SAND2015-3314

SANDIA REPORT

TBD
Unlimited Release
Printed TBD

Development of high-fidelity models for liquid fuel spray atomization and mixing processes in transportation and energy systems

Rainer N. Dahms, Joseph C. Oefelein

Prepared by
Sandia National Laboratories
Albuquerque, New Mexico 87185 and Livermore, California 94550

Sandia National Laboratories is a multi-program laboratory managed and operated by Sandia Corporation, a wholly owned subsidiary of Lockheed Martin Corporation, for the U.S. Department of Energy's National Nuclear Security Administration under contract DE-AC04-94AL85000.

Sandia National Laboratories

Issued by Sandia National Laboratories, operated for the United States Department of Energy by Sandia Corporation.

Available to DOE and DOE contractors from
U.S. Department of Energy
Office of Scientific and Technical Information
P.O. Box 62
Oak Ridge, TN 37831

Telephone: (865) 576-8401
Facsimile: (865) 576-5728
E-Mail: reports@adonis.osti.gov
Online ordering: http://www.osti.gov/bridge

Available to the public from
U.S. Department of Commerce
National Technical Information Service
5285 Port Royal Rd
Springfield, VA 22161

Telephone: (800) 553-6847
Facsimile: (703) 605-6900
E-Mail: orders@ntis.fedworld.gov
Online ordering: http://www.ntis.gov/help/ordermethods.asp?loc=7-4-0#online

TBD
Unlimited Release
Printed TBD
Reprinted TBD

Development of high-fidelity models for liquid fuel spray atomization and mixing processes in transportation and energy systems

Rainer N. Dahms
Reacting Flow Research Department
Sandia National Laboratories
P.O. Box 969
Livermore, CA 94550-0969
rndahms@sandia.gov

Joseph C. Oefelein
Reacting Flow Research Department
Sandia National Laboratories
P.O. Box 969
Livermore, CA 94550-0969
oefelei@sandia.gov

Abstract

Significant inadequacies of current models for multiphase flows present a major barrier to rapid development of advanced high-efficiency low-emissions combustion devices. Liquid spray atomization processes largely determine fuel-air mixture formation, which subsequently govern combustion and controls performance, emissions, and durability of a device. The current study presents a fundamentally-consistent framework to model the effects of breakup processes, liquid drop deformations, and internal flow dynamics on mass, momentum, and energy exchange functions. This framework builds on the Taylor Analogy Breakup (TAB) model which naturally quantifies local drop deformation dynamics. Real-fluid multicomponent thermodynamic property modeling and Gradient Theory simulations facilitate accurate calculations of molecular two-phase interface exchange functions, surface tensions forces, drop oscillations, and breakup processes. The analysis establishes that these drop dynamics, along with finite liquid viscosity effects, significantly alter gas-liquid exchange functions. The study quantifies these effects for the resulting drag coefficients of liquid drops and demonstrates significant deviations from the classic dynamic drag model, which is widely applied in modern simulations performed in academia and industry. This work also quantifies effects, which originate from gas-liquid coupling dynamics, on evaporation and heating rates. The analysis establishes that the consideration of these coupling dynamics modify mass and energy transfer rates even more significantly than the corresponding drag forces from momentum exchange. This physical complexity, however, is largely neglected in modern studies from academia and industry. A new set of equations is presented to improve the modeling of drop breakup processes to address the current shortcomings in the prediction of resulting drops properties over the full range of relevant breakup conditions. The framework is based on a refined energy balance equation which explicitly enforces drop momentum conservation during the breakup process. The introduced modeling framework is entirely derived from conservation equations for mass, momentum, and energy and does not, as a consequence, introduce new modeling constants. The significance of the developed modeling advances to fuel injection processes is demonstrated using Large Eddy Simulation (LES) with a Lagrangian-Eulerian modeling approach.

Contents

List of Figures

List of Tables

This page intentionally left blank.

Chapter 1

Introduction

We develop a model framework to simulate liquid atomization and spray dynamics typically encountered in modern transportation, propulsion, and power systems (e.g., reciprocating and gas-turbine internal combustion engines). The Lagrangian-Eulerian approach is employed, with emphasis on the development of a fully coupled Lagrangian system of models to systematically treat the classical situation where a well-defined molecular interface separates the injected liquid from ambient gases due to the presence of surface tension. Interactions between dynamic shear forces and surface tension promote secondary breakup processes that evolve from a dense to a dilute state, where drop-drop interactions are negligible and dilute spray theory can be used. The system of models is developed in the context of large-eddy-simulation (LES). We utilize the Lagrangian-Eulerian modeling approach which solves the turbulent gaseous phase in the Eulerian frame while individual liquid drops are modeled in the Lagrangian frame.

Lagrangian techniques, unlike Eulerian methods, naturally accommodate non-equilibrium processes that differ substantially from a Maxwellian distribution. Thus, Lagrangian methods can be applied over a wide range of drop Stokes, Weber, and Reynolds numbers and, as such, can conceptually be applied both in the dense and dilute spray regimes. Lagrangian methods are also able to accurately represent multicomponent vaporization processes, drop breakup and collisions, and coupled interactions with the local turbulent flow field. Furthermore, there is a widespread misconception that a point particle approach, along with the corresponding restriction to computational grid regions of small liquid phase volume fractions, is an intrinsic feature of Lagrangian spray modeling. In fact, if formulated consistently from the standpoint of filtering, no such restriction exists. This makes the Lagrangian method potentially suitable to model dense spray breakup, the resultant polydispersed distribution of finite size drops, and the inherent nonlinear, nonequilibrium, multiscale interactions that occur with the gas phase using highly-refined grids.

Here, we systematically develop a Lagrangian based model framework aimed at treating the cascade of processes associated with liquid fuel atomization. The coupled system of models is physics-based, where for example we avoid the use of parcel methods and instead treat physical drops directly. Particular emphasis is placed on the treatment of secondary breakup processes.

Past Literature

Numerous spray combustion models have been proposed over the past three decades. Reviews by Faeth [26, 27] systematically organize relevant works up to 1987. With subtle differences in specific detail, current methodologies have generally been classified as either locally-homogeneous-flow (*LHF*) models, where the condensed-phase is assumed to be in local thermodynamic equilibrium with the gas-phase, or separated-flow (*SF*) models, where finite-rate interphase transport is considered. Of these two classes, *SF* models have received the widest acceptance.

SF models are generally categorized within three groups: 1) continuous-particle-models; 2) discrete-particle-models; and 3) continuum-formulation-models. Continuous particle models employ a multidimensional drop distribution function which gives a statistically accurate field description of the spray. Discrete particle models, in contrast, employ a finite number of computational parcels to achieve the same description. Parcels act as delta function point sources which represent classes of drops in various states. Continuum formulation models treat the gas and dispersed particle-phase as interpenetrating continua. The basic formulation results in similar governing equations for both phases, which can become ambiguous when attempting to represent turbulent stresses and interphase transport processes.

Of the three *SF* models described above, the continuous-particle-model proposed by Williams [109] and the discrete-particle-model proposed by Crowe et al. [8] are fundamentally important. Consider a drop distribution function $f(\mathbf{s};\mathbf{x},t)$ where $\mathbf{s}$ represents an M dimensional vector with components that represent those properties required to adequately describe the state of the spray. This function is defined such that $f(\mathbf{s};\mathbf{x},t)ds_1ds_2\ldots ds_M$ represents the probable number of drops, per unit system volume, per unit time, which exist in a given state $s_1, s_2, \ldots, s_M$. The continuous-particle-model accommodates the distribution function directly using a phenomenological Liouville equation typically referred to as the spray equation [110]. This equation describes the time evolution of the drop distribution function and can be written in the general form

$$\frac{\partial f}{\partial t} + \nabla \cdot \left(\frac{\partial x_p}{\partial t} f \right) + \sum_{i=1}^{M} \left[\nabla_i \cdot \left(\frac{\partial s_i}{\partial t} f \right) \right] = \dot{f}_c + \dot{f}_b \tag{1.1}$$

where ∇_i represents a gradient operator with respect to the coordinate s_i. Quantities $\dot{f}_c$ and $\dot{f}_b$ represent the net rate of increase, per unit volume of drops in state s_i, due to collision and break-up processes, respectively.

Difficulties arise with continuous-particle-models due to the multidimensional character of the distribution function and the level of resolution required to minimize numerical diffusion when steep gradients with respect to f exist. A practical implementation of Eq. (1.1) requires one of two treatments: 1) specifying the functional dependence of the drop distribution function in terms of statistical variances; i.e., $f(\mathbf{s};\mathbf{x},t) = F(\hat{\mu}, \hat{\sigma}, \hat{\kappa}, \ldots)$, where $\hat{\mu}$, $\hat{\sigma}$, $\hat{\kappa}$, ..., etc. represent variances such as the mean, standard deviation, kurtosis, ..., etc. or; 2) implementing discrete-particle-models. There are major limitations associated with the first treatment due to a general lack of knowledge regarding the correct functional form of the drop distribution function. There is little evidence to suggest the existence of a single universally correct form.

Discrete-particle-models minimize problems associated with numerical diffusion by solving a set of Lagrangian equations of motion and transport for the life histories of a statistically significant sample of particles. Because of the large number of drops present in an actual spray, a sampling technique is employed whereby characteristic groups of drops are represented by computational parcels. As outlined by Dukowicz [20], this implies a distribution function of the form

$$f(\mathbf{s};\mathbf{x},t) = \frac{1}{\Delta V}\sum_{k=1}^{P} n_{d_k}\left(\prod_{i=1}^{M}\delta(s_i - s_{i_k})\right) \tag{1.2}$$

where n_{d_k} represents the number of identical drops in the k^{th} parcel, s_{i_k} represents the i^{th} property associated with this parcel and P the total number of parcels. The quantity n_{d_k} is determined at the inlet boundary through joint specification of a number distribution function and the total particle mass M_p. These quantities are related by the expression

$$M_p = \sum_{k=1}^{P} n_{d_k} m_{d_k} \tag{1.3}$$

Assuming an adequate number of drops are represented, discrete-particle-models can simulate the full drop distribution function. The primary difficulty with this approach arises from the introduction of large fluctuating transport sources when an insufficient number of parcels are used in the computations.

Travis et al. [101] have shown that continuous-particle-models can be directly related to discrete-particle-models by taking various moments of the spray equation. Moment equations are derived by multiplying Eq. (1.1) by selected components of $\mathbf{s}$ then integrating over all drop coordinates $s_1, s_2, \ldots, s_M$. This yields a system of partial differential equations that describe the behavior of the selected components. In the absence of collision and break-up processes, this system of equations can be decoupled into a set of ordinary differential equations. The resultant system describes the Lagrangian particle path, energy, and mass transfer characteristics of the spray. Early works, such as the investigations conducted by Crowe et al. [8], did not account for turbulence in the calculation procedure. Subsequently, however, stochastic methods were adopted to simulate the instantaneous velocity field. Dukowicz [20], O'Rourke [66], and Gosman and Ioannides [33] were the first to adopt stochastic methods to study drop dispersion due to turbulence. Shuen [84] (see [27]) has extended the methodology of Gosman and Ioannides to include the effects of turbulence on interphase heat and mass transfer. Here, turbulent eddy lifetimes are specified in the vicinity of each parcel using the scaling arguments associated with the turbulence model. A particle is assumed to interact with an eddy for a time defined as the smaller of the eddy lifetime or the characteristic transit time, as given by the Lagrangian equations of motion. This methodology, which is commonly referred to as the stochastic-separated-flow (*SSF*) model, has been evaluated in a wide variety of flows and appears to be the most efficient way to handle particulate dynamics in steady-state spray combustion algorithms. The current work extends this methodology to model unsteady spray dynamics using the *LES* framework.

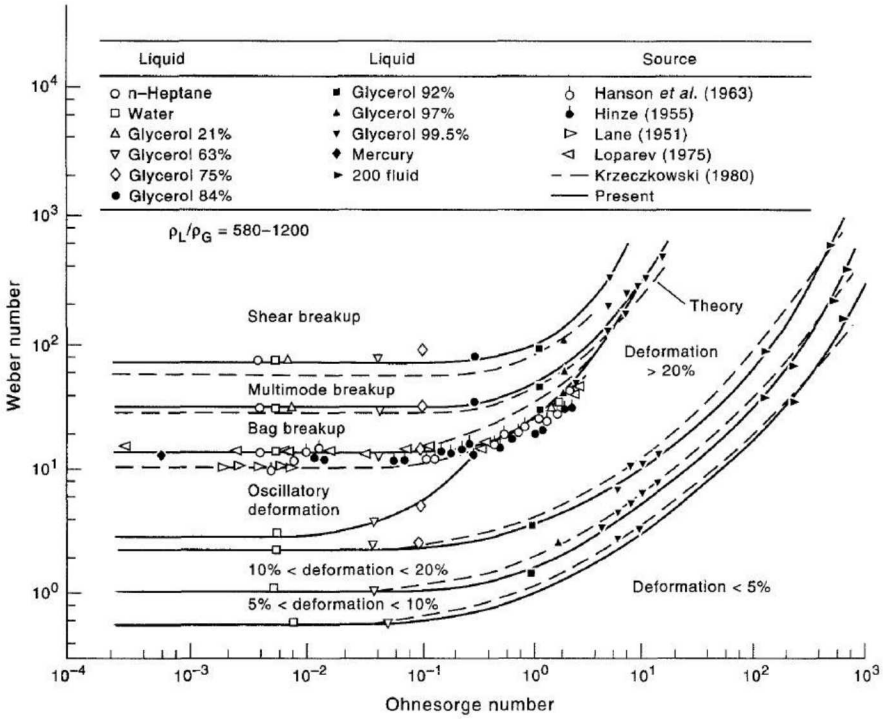

Figure 1.1. The drop deformation and breakup regime map according to Hsiang and Faeth [38].

In accelerating flows, the liquid drops are generally not in equilibrium with the flow and are therefore subject to aerodynamic forces which may cause drop deformations, oscillations, and different types of breakup events. It has long been recognized that such processes can be classified by the Weber number, which relates forces imposed by fluid flow to the restoring surface tension, and the Ohnesorge number, which relates the viscous forces of the drop to its inertia and surface tension. Based on these parameters, widely-accepted regime diagrams for drop deformation and breakup have been compiled such as those presented by Hsiang and Faeth [38], shown in Fig. 1.1, or by Lasheras and Hopfinger [44]. They classify the response of a single drop based on the local fluid dynamics and its thermodynamic state. At low Weber numbers ($0.5<\mathrm{We}<2$), liquid drops deform with a corresponding deformation up to $\approx 20\%$. At higher Weber numbers, drops undergo harmonic oscillations without breakup which is generally suppressed below the critical Weber number $\mathrm{We}_c \approx 12$. Then, drops experience bag breakup and multimode breakup up to Weber numbers of $\mathrm{We} \approx 100$. At higher Weber numbers, shear and stripping breakup processes occur before drops finally undergo a catastrophic breakup at $\mathrm{We} > 350$. These regime separators are valid at low Ohnesorge numbers ($\mathrm{Oh}<0.05$). At higher Ohnesorge numbers, the corresponding classification of deformation and breakup processes remains valid but they are generally initiated at higher Weber numbers which depend on the respective Ohnesorge number.

Over the past three decades, many models have been developed to simulate such drop dynamics, two of which have found wide acceptance and have entered into academic and commercial fluid flow software [2, 3, 39, 53, 83]. The first is the classic WAVE model, originally developed by Reitz [73] and by Reitz and Diwakar [75], and the second is the TAB model, originally developed by O'Rourke and Amsden [67]. The classic WAVE breakup model associates the mechanism of drop breakup with the analogy to Kelvin-Helmholtz instabilities along cylindrical liquid jets of viscous fluids. It assumes that the time of breakup and the produced drop sizes are proportional to the growth rate and wavelength of the most unstable Kelvin-Helmholtz instability at the present flow conditions [73, 74]. Most recently, this model has been improved by advancing the analogy to a jet with a linear shear layer in the surrounding gas phase to lift the previous assumption of a velocity discontinuity at the fluid interface [104]. This development added the thickness of the resulting shear layer to the surface tension force as a leading order mechanism to drive surface wave instabilities.

Previously, the Rayleigh-Taylor mechanism was also included in the prediction of the corresponding surface growth rate which determines drop breakup [41, 76]. In analogy to the Kelvin-Helmholtz instability criterion, drop breakup is assumed to occur after a certain time period of corresponding wave growth. Then, the resulting drop sizes are determined as being proportional to the respective wavelength. This breakup model has been successfully applied to describe shear and catastrophic breakup events which occur at high Weber numbers ($We > 100$). As a surface wave prediction model, however, the approach largely neglects the large-scale drop dynamics before the breakup event such as drop deformations. As a consequence, it also largely neglects interactions of those dynamics with drop mass, momentum, and energy transfer. The model also generally assumes a constant resulting drop size after breakup which is not necessarily consistent with experimental evidence.

The Taylor-Analogy-Breakup (TAB) model is built upon Taylor's analogy between drop dynamics and a forced spring-mass-damper system [100]. It thereby explicitly models the deformation and oscillation of drop dynamics and assumes that drop breakup occurs as soon as such oscillations of the drop poles meet at its center. Then, an energy equation is consulted to predict the properties of newly created drops after breakup. The model is conceptually valid for a wide range of Ohnesorge numbers and Weber numbers up to values which correspond to the shear breakup regime, compare Fig. 1.1. At higher Weber numbers, drop breakup is increasingly determined by surface stripping processes for which the forced spring-mass-damper system is not necessarily a meaningful surrogate model. Since its original introduction, many studies from academia and industry have shown, however, that the predicted drop sizes after breakup are often significantly under-predicted and that deficiencies in the prediction of the spray angle, to which the breakup model contributes, exist [42, 52, 97–99, 103]. These deficiencies, along with the attempt to extend the validity of TAB model to higher Weber number regimes, have mainly motivated further developments since such as the Enhanced Taylor Analogy Breakup (ETAB) model [97, 99].

The "ETAB-law" postulates that the rate of drop creation after breakup is proportional to the number of critically deformed drops. It must be noted, however, that the physical basis of this law is not yet rigorously established and that the respective proportionality constants must be set, dependent on the breakup regime, to match experimental data. A subsequently applied smoothing

function guarantees a continuous distribution of the value of the proportionality constant across the different breakup regimes [97]. A uniform drop size distribution after breakup is applied which is not necessary supported by experimental evidence of drop breakup in relevant regimes [38, 44]. Further, ETAB tunes the initial rate of drop deformation to extend the breakup time in order to match experimentally determined values of jet breakup lengths. After breakup and similar to the original formulation from O'Rourke and Amsden, the newly created drops receive a velocity component normal to the velocity vector of the original drop. The ability of these methods to comply with laws of drop momentum conservation is, however, questionable. More recently, the Cascade Atomization and Drop Breakup (CAB) model was introduced as a further development of ETAB model [98]. This model builds on the "ETAB-law" in an attempt to extend its applicability to the catastrophic breakup regime relevant for near-nozzle regions. Additionally, the CAB model constant has been selected to naturally guarantee its continuous distribution across the different breakup regimes without the utilization of a smoothing function as previously required in ETAB.

In previously developed frameworks for device-scale turbulent combustion simulations, the coupling of drop distortion, oscillation, breakup, and internal flow dynamics to the conservation equations is, despite its relevance, largely neglected. To this end, however, a dynamic drag model is widely applied in academia and industry to account for the effect of drop distortion on its aerodynamic drag [51, 83, 89, 102]. This correction to the drag law is facilitated by a linear interpolation between the drag of a sphere and the drag of a disc as originally proposed by Liu *et al.* [51]. It is worth mentioning, however, that, instead of the postulated sharp-edged disc, the drop deformation limit predicted by TAB model does resemble the shape of an oblate spheroid. Further, this widely-applied drag correction model is only valid and utilized for positive distortions. Hence, it neglects deformations into prolate spheroids which naturally occur during drop oscillations. Additionally, recent studies have raised concerns about the validity of linear interpolations of reference drag coefficients over the range of relevant drop Reynolds numbers [30, 34, 37, 77]. Furthermore, effects which originate from the coupling of drop dynamics and internal flow dynamics on heat and mass transfer are also relevant but are still largely neglected [7, 12–16, 18, 19, 29, 59, 82, 83, 108, 112]. Sirignano and co-workers were one of the first to discover and quantify the effects of internal flow dynamics on drop heating and evaporation [1, 85, 87]. However, such models are not fully utilized in current modeling frameworks.

The current work is based on the TAB model due to its natural ability to resolve complex drop dynamics and its validity over relevant ranges of Weber and Ohnesorge numbers. A framework suitable for device-scale simulations is presented in which drop distortions, oscillations, and internal flow dynamics are fully coupled to the mass, momentum, and energy transfer equations. Real-fluid thermodynamics and mean-field molecular gas-liquid interface methods facilitate accurate simulations of two-phase transfer functions and dynamics of drop oscillations at high Weber numbers. The aerodynamic forces are calculated from the coupling to high-fidelity large eddy simulations. A suitable temporal resolution of the drop dynamics is employed in order to accurately capture the complex interactions between those forces and the drop response. The drop breakup event is modeled by a new set of equations to address the current shortcomings in the prediction of resulting drops properties over the full range of relevant breakup conditions. This model is entirely derived from conservation equations for mass, momentum, and energy and does not, as a consequence, introduce new modeling constants.

Chapter 2

Theoretical-Numerical Formulation

In the current work, we use the formalism developed by Oefelein [62, 65]. The system of interest is assumed to be compressible, multicomponent and to contain a turbulent, chemically-reacting, multiphase fluid mixture composed of N species. Respective phases are assumed to consist of multicomponent fluids. Historically, the application of LES to inert single-phase flow has involved only spatial filtering since, by coincidence, truncation errors associated with small-scale temporal fluctuations are typically small. In the more general case, however, the filtering operation must accommodate both temporal and spatial fluctuations. This is particularly true for multiphase flows that involve significant nonlinear space-time interactions over ranges of scales much smaller than those given by Kolmogorov theory. The application of temporal filtering accounts for the presence of subfilter fluctuations in time. These quantities must ultimately be accounted for in a consistent manner to capture important physical dynamics associated with sprays. Starting with the instantaneous system, the filtered equations have been derived in a general manner that retains commutation properties in space and time. A filtered void fraction is defined as an artifact of this operation. Interphase exchange functions with clear and distinct physical interpretations are derived naturally as part of the mathematical formalism with no *a priori* assumptions made to define the physical or geometric characteristics of the multiphase fluid elements or the spatial and temporal nature of the corresponding subfilter dynamics. The resultant system of integro-differential equations provide a unified framework that facilitates the closure problem in a well-posed, numerically compatible manner. This system is summarized as follows. See [65] for details.

Instantaneous Conservation Equations

The instantaneous conservation equations of mass, momentum, total-energy and chemical species are presented in this section to provide the basis for the formulation and analysis of the corresponding filtered system. The system of interest is assumed to be compressible, multicomponent, and to contain a turbulent, chemically-reacting, multiphase fluid-mixture composed of N species. Respective phases are assumed to consist of multicomponent fluids or solid particulates. Fluid mixtures associated with each phase are assumed to follow the continuum approximation. This system is representative of a general class of problems over a wide range of Reynolds numbers and Mach numbers and includes incompressibility and inert single-phase flow as limiting extremes. The baseline system of equations are cast in dimensionless form using a reference length scale, δ_{ref}, flow speed, U_{ref}, and fluid state characterized by a reference density, ρ_{ref}, sound speed,

Table 2.1. Definition of dimensionless variables.

Spatial Coordinates	Time	Velocity
$\mathbf{x} = \dfrac{\mathbf{x}^*}{\delta_{\text{ref}}}$	$t = \dfrac{t^* U_{\text{ref}}}{\delta_{\text{ref}}}$	$\mathbf{u} = \dfrac{\mathbf{u}^*}{U_{\text{ref}}}$
Density	Pressure	Temperature
$\rho = \dfrac{\rho^*}{\rho_{\text{ref}}}$	$p = \dfrac{p^*}{\rho_{\text{ref}} c_{\text{ref}}^2}$	$T = \dfrac{T^* C_{p_{\text{ref}}}}{c_{\text{ref}}^2}$
Internal Energy	Enthalpy	Specific Heat
$e = \dfrac{e^*}{c_{\text{ref}}^2}$	$h = \dfrac{h^*}{c_{\text{ref}}^2} = e + \dfrac{p}{\rho}$	$C_p = \dfrac{C_p^*}{C_{p_{\text{ref}}}}$
Dynamic Viscosity	Prandtl Number	Schmidt Number(s)
$\mu = \dfrac{\mu^*}{\mu_{\text{ref}}}$	$Pr = \dfrac{\mu^* {C_p}^*}{\lambda^*}$	$Sc_i = \dfrac{\mu^*}{\rho^* \mathscr{D}_{im}^*}$
Chemical Source Term(s)		
$\dot{\omega}_i = \dfrac{\dot{\omega}_i^* \delta_{\text{ref}}}{\rho_{\text{ref}} U_{\text{ref}}}$		

c_{ref}, constant pressure specific heat, $C_{p_{\text{ref}}}$, and dynamic viscosity, μ_{ref}. Using these quantities, a reference Mach and Reynolds number are defined as

$$M = \frac{U_{\text{ref}}}{c_{\text{ref}}} \text{ and } Re = \frac{\rho_{\text{ref}} U_{\text{ref}} \delta_{\text{ref}}}{\mu_{\text{ref}}}.$$

A set of dimensionless variables are defined in terms of the dimensional counterparts (denoted here using the superscript $()^*$) by the relations given in Table 2.1. With these definitions, the instantaneous conservation equations of mass, momentum, total-energy and chemical species can be written in conservative form as follows.

- Mass:

$$\frac{\partial \rho}{\partial t} + \nabla \cdot (\rho \mathbf{u}) = 0. \tag{2.1}$$

- Momentum:

$$\frac{\partial}{\partial t}(\rho \mathbf{u}) + \nabla \cdot \left[\rho \mathbf{u} \otimes \mathbf{u} + \frac{p}{M^2}\mathbf{I}\right] = \nabla \cdot \tau, \tag{2.2}$$

  where

$$\tau = \frac{\mu}{Re}\left[-\frac{2}{3}(\nabla \cdot \mathbf{u})\mathbf{I} + \left(\nabla \mathbf{u} + \nabla \mathbf{u}^T\right)\right]$$

  represents the viscous-stress tensor.

- Total-energy:

$$\frac{\partial}{\partial t}(\rho e_t) + \nabla \cdot [(\rho e_t + p)\mathbf{u}] = \nabla \cdot \left[\mathbf{q}_e + M^2(\tau \cdot \mathbf{u})\right], \tag{2.3}$$

  where

$$\begin{aligned} e_t &= e + \frac{M^2}{2}\mathbf{u} \cdot \mathbf{u}, \\ e &= \sum_{i=1}^{N} h_i Y_i - \frac{p}{\rho}, \text{ and} \\ h_i &= h_{f_i}^{\circ} + \int_{p^{\circ}}^{p} \int_{T^{\circ}}^{T} C_{p_i}(T,p)\, dT dp \end{aligned}$$

  represent the total internal energy, internal energy and enthalpy of the i^{th} species, respectively, and

$$\mathbf{q}_e = \frac{\mu C_p}{PrRe}\nabla T + \sum_{i=1}^{N} h_i \mathbf{q}_i$$

  represents the energy flux due to heat conduction and mass diffusion.

- Species:

$$\frac{\partial}{\partial t}(\rho Y_i) + \nabla \cdot (\rho Y_i \mathbf{u}) = \nabla \cdot \mathbf{q}_i + \dot{\omega}_i \qquad i = 1, \ldots, N-1 \tag{2.4}$$

where

$$\mathbf{q}_i = \frac{\mu}{Sc_i Re} \nabla Y_i$$

and $\dot{\omega}_i$ represent, respectively, the mass diffusion flux and the instantaneous rate of production of the i^{th} chemical species due to reactions.

In the system above the heat release due to chemical reactions in the total-energy equation is accounted for in the description of the specific enthalpies, h_i, as given by the enthalpy of formation, $h^\circ_{f_i}$. This term can be represented equivalently with a source term on the right hand side of Equation (2.3) as the product of the enthalpy of formation and the local rate of production of all the species considered in the system. Using this representation, the source term for chemical energy and specific enthalpies are defined by the expressions

$$\dot{Q}_e = -\sum_{i=1}^{N} \dot{\omega}_i h^\circ_{f_i}, \text{ and} \tag{2.5}$$

$$h_i = \int_{p^\circ}^{p} \int_{T^\circ}^{T} C_{p_i}(T,p)\, dT\, dp. \tag{2.6}$$

For illustration purposes, radiation fluxes and body forces have been neglected and a common set of assumptions have been made with respect to the viscous-stresses, diffusive energy flux, and diffusive mass flux terms. In particular, the viscous-stress tensor is assumed to follow Stokes' hypothesis, Dufour and Soret effects are neglected, and Fick's and Fourier's laws have been used to represent thermal and mass diffusion processes. These assumptions are not required to derive the filtered system and can easily be relaxed or altered. Alternative constitutive relationships can also be easily substituted.

Filtered Conservation Equations for Multiphase Flow

Equations (2.1) – (2.4) coupled with an appropriate equation of state, appropriate treatments of thermodynamic and transport properties, and validated mixing and combining rules for treatment of mixtures accommodate the most general system of interest including cases when preferential diffusion processes and strong compressibility effects are present. No assumptions have been made regarding the thermodynamic ideality of the system. Oefelein [65] has shown that the filtering operation can be performed using modified convolution integrals [48, 49] with an arbitrary filter kernel that accounts for both temporal and spatial fluctuations. This approach leads to the

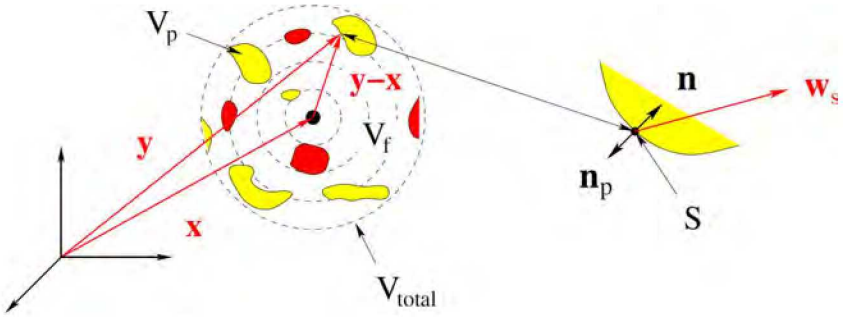

Figure 2.1. Schematic diagram of the hypothetical volume of influence, V_{total}, associated with the filter kernel, $\mathscr{G}(\mathbf{y}-\mathbf{x},\tau-t;\delta\mathbf{y},\delta\tau)$, in a multiphase flow field. The term V_f represents the volume occupied by the fluid to which the governing conservation equations are being applied. The term V_p represents the volume occupied by all other multiphase fluid elements. Evolution in time within V_{total} is inferred.

formal derivation of the interphase exchange functions that couples the Eulerian gas phase to the Lagrangian particulate (e.g., liquid) phase. The filter kernel is denoted $\mathscr{G}(\mathbf{y}-\mathbf{x},\tau-t;\delta\mathbf{y},\delta\tau)$ and characterizes the weighted contribution of small-scale processes at remote points $(\mathbf{y},\tau)$ on filtered values at the collocation points $(\mathbf{x},t)$. This definition provides a high level of generality. The resultant system of filtered equations are formally indifferent to the precise nature of the filter, except for certain broad conditions specified below.

Figure 2.1 shows a schematic diagram of the hypothetical volume of influence, V_{total}, associated with the filter kernel, $\mathscr{G}$, in a multiphase flow field. The terms $\mathbf{y}$ and $\mathbf{x}$ represent three-dimensional position vectors in space with a common origin such that the vector $\mathbf{y}-\mathbf{x}$ originates at the collocation point $\mathbf{x}$. The terms τ and t are the temporal analogy of $\mathbf{y}$ and $\mathbf{x}$, respectively, such that $\tau-t$ has an origin defined with respect to a fixed point in real-time t. The quantities $\delta\mathbf{y}$ and $\delta\tau$ represent the spatial and temporal filter widths. Phase boundaries in multiphase systems introduce discontinuities that violate the continuum approximation. The governing equations cannot be applied across these boundaries, and likewise, it is not formally correct to apply the filtering procedure across these boundaries. To accommodate this problem mathematically, integration of the convolution integrals can only be performed within the volume occupied by the fluid to which the governing conservation equations are being applied. This region is represented by V_f in Figure 2.1. The term V_p represents the volume occupied by all other multiphase fluid elements within V_{total}. The definitions of V_f and V_p are purely formal. These regions of integration are only known in principle and must ultimately be modeled.

In general, respective fluid elements described by the volume V_p can differ in composition. At any instant in time the total volume of influence associated with the filter can be occupied by

multiple phases according to the relationship

$$V_{total}(\mathbf{x},t) = V_f(\mathbf{x},t) + \sum_p V_p(\mathbf{x},t), \tag{2.7}$$

where the summation over "p" represents each discrete fluid element within the total volume of influence other than V_f. Equation (2.7) can be written alternatively as

$$\theta(\mathbf{x},t) + \sum_p \theta_p(\mathbf{x},t) = 1, \tag{2.8}$$

where $\theta = V_f/V_{total}$ and $\theta_p = V_p/V_{total}$ represent the corresponding instantaneous volume (or "void") fractions associated with each distinct phase.

The functional characteristics of the filter kernel must obey a broad set of mathematical properties. By definition, $\mathscr{G}$ must be nonnegative and approach zero sufficiently rapidly with distance from the collocation point $(\mathbf{x},t)$ to insure the existence of its integral in space and time. In particular, it must exhibit compact support such that $\mathscr{G}(\mathbf{y}-\mathbf{x},\tau-t;\delta\mathbf{y},\delta\tau) = 0$ for $|\mathbf{y}| > M$ and $|\tau| > N$, where M and N represent finite positive real numbers. The filter kernel must also be normalized, both in time and space within the volume V_{total} (as defined in Figure 2.1), such that

$$\int_{-\infty}^{t} \left\{ \iiint_{V_{total}} \mathscr{G}(\mathbf{y}-\mathbf{x},\tau-t;\delta\mathbf{y},\delta\tau)\, dV \right\} d\tau = 1. \tag{2.9}$$

This insures that the correct space-time scaling is applied remotely and, equivalently, that the filtered component of a constant retains the same value. The time domain characteristics of $\mathscr{G}$ must also be causal, which applies to real-time processes and produces output that depends only on inputs at the current time or earlier. Causal filters reduce to a Dirac delta function in time in the limit as $\delta\tau \to 0$.

When integration is performed within the volume V_f, the normalization condition described by Equation (2.9) gives rise to the filtered analog of the void fraction $\theta(\mathbf{x},t)$ defined in Equation (2.8). This term can be obtained in two ways. The first involves direct integration of the filter function within the volume V_f. The second involves application of the identity given by Equation (2.8). Performing these operations yields

$$\begin{aligned} \overline{\theta}(\mathbf{x},t) &= \int_{-\infty}^{t} \left\{ \iiint_{V_f(\tau)} \mathscr{G}(\mathbf{y}-\mathbf{x},\tau-t;\delta\mathbf{y},\delta\tau)\, dV \right\} d\tau \\ &= 1 - \int_{-\infty}^{t} \left\{ \sum_p \iiint_{V_p(\tau)} \mathscr{G}(\mathbf{y}-\mathbf{x},\tau-t;\delta\mathbf{y},\delta\tau)\, dV \right\} d\tau, \end{aligned} \tag{2.10}$$

where $\overline{\theta}(\mathbf{x},t)$ is defined as the "filtered" void fraction. Similarly, the mathematical definition of an arbitrary filtered variable, $\overline{\phi}_i(\mathbf{x},t)$, is defined by the convolution integral

$$\overline{\theta}(\mathbf{x},t)\overline{\phi}_i(\mathbf{x},t) = \underbrace{\int_{-\infty}^{t} \underbrace{\left\{ \iiint_{V_f(\tau)} \mathscr{G}(\mathbf{y}-\mathbf{x},\tau-t;\delta\mathbf{y},\delta\tau)\phi_i(\mathbf{y},\tau)\,dV \right\}}_{(i)} d\tau}_{(ii)}, \tag{2.11}$$

where $\phi_i(\mathbf{x},t)$ is assumed to be any arbitrary intensive quantity. Term (i) in Equation (2.11) characterizes the net influence of subfilter processes at remote points $\mathbf{y}$ on filtered values at $\mathbf{x}$, at remote times τ. Term (ii) represents the time-filtered effects of small-scale temporal fluctuations associated with (i), within V_{total}, over the interval $-\infty < \tau \leq t$. The quantity $\overline{\phi}_i(\mathbf{x},t)$ is an intrinsic average within the volume V_f. The filtered void fraction, $\overline{\theta}$, accounts for the fact that integration was carried out within V_f and provides the correction that relates respective intrinsic averages back to V_{total}.

Using the definitions above and the standard Favre and Reynolds averaged field decompositions, the filtered conservation equations of mass, momentum, total-energy, and species for a multiphase (particulate) flow can be expressed as can be derived in a completely general manner with no *a priori* assumptions made regarding the geometric character of the multiphase fluid elements or the spatial and temporal nature of the small-scale dynamics. Development of the these equations depends on two basic assumptions. The multiphase media is assumed to reside in disjoint and complementary regions in space, and respective phases are assumed to behave as a continuum. The system can be written in conservative form as follows.

- Filtered Mass:

$$\frac{\partial}{\partial t}(\overline{\theta}\overline{\rho}) + \nabla\cdot(\overline{\theta}\overline{\rho}\tilde{\mathbf{u}}) = \overline{\dot{\rho}}_s. \tag{2.12}$$

- Filtered Momentum:

$$\begin{aligned} \frac{\partial}{\partial t}(\overline{\theta}\overline{\rho}\tilde{\mathbf{u}}) + \nabla\cdot\left[\overline{\theta}\left(\overline{\rho}\tilde{\mathbf{u}}\otimes\tilde{\mathbf{u}} + \frac{\overline{p}}{M^2}\mathbf{I}\right)\right] &= \nabla\cdot(\overline{\theta}\,\overline{\tau}) \\ &- \nabla\cdot(\overline{\theta}\,\mathbf{T}) + \overline{\dot{\mathbf{F}}}_s, \end{aligned} \tag{2.13}$$

where

$$\overline{\tau} = \overline{\frac{\mu}{Re}\left[-\frac{2}{3}(\nabla\cdot\mathbf{u})\mathbf{I} + (\nabla\mathbf{u} + \nabla\mathbf{u}^T)\right]}.$$

- Filtered Total Energy:

$$\begin{aligned}\frac{\partial}{\partial t}(\overline{\theta}\overline{\rho}\tilde{e}_t)+\nabla\cdot\left[\overline{\theta}(\overline{\rho}\tilde{e}_t+\overline{p})\tilde{\mathbf{u}}\right] &= \nabla\cdot\left[\overline{\theta}\left(\overline{\mathbf{q}}_e+M^2(\overline{\tau}\cdot\tilde{\mathbf{u}})\right)\right]\\ &- \nabla\cdot\left[\overline{\theta}\left(\mathbf{Q}+M^2(\mathbf{T}\cdot\tilde{\mathbf{u}})\right)\right]\\ &- \nabla\cdot\left[\overline{\theta}\,\frac{M^2}{2}tr(\overline{\mathbf{T}\mathbf{u}''})\right]\\ &+ \nabla\cdot(\overline{\theta}\,\overline{\tau\cdot\mathbf{u}''})+\overline{\theta}\dot{\overline{Q}}_e+\dot{\overline{Q}}_s, \end{aligned} \tag{2.14}$$

where

$$\begin{aligned}\tilde{e}_t &= \tilde{e}+\frac{M^2}{2}\tilde{\mathbf{u}}\cdot\tilde{\mathbf{u}}+\frac{M^2}{2}\frac{tr(\mathbf{T})}{\overline{\rho}},\\ \tilde{e} &= \underbrace{\sum_{i=1}^{N}\tilde{h}_i\tilde{Y}_i}_{\tilde{h}}-\frac{\overline{p}}{\overline{\rho}}+\frac{1}{\overline{\rho}}\sum_{i=1}^{N}\overline{\rho h_i''Y_i''}, \text{ and}\\ \tilde{h}_i &= \int_{\overline{p}^\circ}^{\overline{p}}\int_{\tilde{T}^\circ}^{\tilde{T}}C_{p_i}(T,p)\,dTdp,\\ \dot{\overline{Q}}_e &= -\sum_{i=1}^{N}\overline{\dot{\omega}}_i h_{f_i}^\circ,\end{aligned}$$

as defined by Equations (2.5) and (2.6), and

$$\overline{\mathbf{q}}_e=\overline{\frac{\mu C_p}{PrRe}\nabla T}+\sum_{i=1}^{N}\overline{h_i\mathbf{q}_i}.$$

- Filtered Species:

$$\begin{aligned}\frac{\partial}{\partial t}(\overline{\theta}\overline{\rho}\tilde{Y}_i)+\nabla\cdot(\overline{\theta}\overline{\rho}\tilde{Y}_i\tilde{\mathbf{u}}) &= \nabla\cdot(\overline{\theta}\overline{\mathbf{q}}_i)\\ &- \nabla\cdot(\overline{\theta}\mathbf{S}_i)+\overline{\theta\dot{\omega}_i}+\overline{\dot{\omega}}_{s_i},\end{aligned} \tag{2.15}$$

where

$$\overline{\mathbf{q}}_i=\overline{\frac{\mu}{Sc_iRe}\nabla Y_i}.$$

Equations (2.12) – (2.15) are analogous in form to the Favre averaged system of equations for inert single-phase systems, with the exception of the filtered void fraction and the interphase exchange functions $\dot{\overline{\rho}}_s$, $\overline{\mathbf{F}}_s$, $\dot{\overline{Q}}_s$, and $\overline{\dot{\omega}}_{s_i}$. These functions account for the net exchange of mass, momentum, total-energy and chemical species between phases based on the definition of the filter kernel. It is important to note that the overbar in these equations now represents the definition given by

Table 2.2. General form of interphase exchange functions represented by Equation (2.16).

$\overline{\dot{\mathscr{H}}}_s(\mathbf{x},t)$	$\vec{\vec{\psi}}(\mathbf{y},\tau)\cdot\mathbf{n}_p$
$\overline{\dot{\rho}}_s(\mathbf{x},t)$	$\rho(\mathbf{u}-\mathbf{w}_s)\cdot\mathbf{n}_p$
$\overline{\dot{\mathbf{F}}}_s(\mathbf{x},t)$	$\left\{\rho\mathbf{u}\otimes(\mathbf{u}-\mathbf{w}_s)-\left(-\frac{p}{M^2}\mathbf{I}+\tau\right)\right\}\cdot\mathbf{n}_p$
$\overline{\dot{Q}}_s(\mathbf{x},t)$	$\left\{\rho e_t(\mathbf{u}-\mathbf{w}_s)-\left(-p\mathbf{I}+M^2\tau\right)\cdot\mathbf{u}-\mathbf{q}_e\right\}\cdot\mathbf{n}_p$
$\overline{\dot{\omega}}_{s_i}(\mathbf{x},t)$	$\{\rho Y_i(\mathbf{u}-\mathbf{w}_s)-\mathbf{q}_i\}\cdot\mathbf{n}_p$

Respective terms represented by $\vec{\vec{\psi}}(\mathbf{y},\tau)\cdot\mathbf{n}_p$ can be interchanged using the jump conditions given by Equations (2.17) – (2.20).

Equation (2.11) for the joint space-time filter. This definition has unique relevance, even in the limit of a single phase system where the void fraction is unity and interphase exchange functions are zero.

Each of the interphase exchange functions has the general form

$$\overline{\dot{\mathscr{H}}}_s = \underbrace{\int_{-\infty}^{t} \underbrace{\sum_p \oint\!\!\oint_{S(\tau)} \mathscr{G}(\mathbf{y}-\mathbf{x},\tau-t;\delta\mathbf{y},\delta\tau)\underbrace{\{\vec{\vec{\psi}}(\mathbf{y},\tau)\cdot\mathbf{n}_p\}}_{(i)} dS}_{(ii)}\, d\tau}_{(iii)}, \tag{2.16}$$

where $\overline{\dot{\mathscr{H}}}_s$ denotes a particular source term and $\vec{\vec{\psi}}(\mathbf{y},\tau)\cdot\mathbf{n}_p$ the corresponding surface flux. Table 2.2 lists the specific form of these terms. Term (i) in Equation (2.16) represents the local instantaneous rate of exchange of mass, momentum, total-energy and chemical species, respectively, across multiphase interfaces at remote points $\mathbf{y}$ and τ. Term (ii) represents the spatially-filtered effect of these remote interfacial processes at the collocation point $\mathbf{x}$, at remote times τ. Term (iii) represents the time-filtered effect of small-scale temporal fluctuations associated with (ii) that occur over the interval $-\infty < \tau \leq t$.

Interphase Exchange Functions

Up to this point the regions of integration associated with the filtering operation are only known in principle. Further assumptions are required to characterize the instantaneous shape of the interfaces within the filter volume V_{total}. Accurate characterization of small-scale temporal and spa-

tial interface dynamics hinges on the application of methods and models that accurately describe the position of respective interfaces, the corresponding dynamic evolution, and the interphase exchange of mass, momentum, total-energy and chemical species. For modeling purposes, the interphase exchange processes must be related to the properties of respective phase boundaries. A common approach is to apply the thin film approximation and assume that there is no net accumulation of mass, momentum, energy, or chemical species within the interfacial boundaries. Local properties on either side of an interface can be related by the jump relations

$$\rho(\mathbf{u}-\mathbf{w}_s)\cdot\mathbf{n}_p = \rho(\mathbf{u}_p-\mathbf{w}_s)\cdot\mathbf{n}_p, \tag{2.17}$$

$$\left\{\rho\mathbf{u}\otimes(\mathbf{u}-\mathbf{w}_s)-\left(-\frac{p}{M^2}\mathbf{I}+\tau\right)\right\}\cdot\mathbf{n}_p = \left\{\rho\mathbf{u}_p\otimes(\mathbf{u}_p-\mathbf{w}_s)-\left(-\frac{p_p}{M^2}\mathbf{I}+\tau_p\right)\right\}\cdot\mathbf{n}_p, \tag{2.18}$$

$$\left\{\rho e_t(\mathbf{u}-\mathbf{w}_s)-\left(-p\mathbf{I}+M^2\tau\right)\cdot\mathbf{u}-\mathbf{q}_e\right\}\cdot\mathbf{n}_p = \left\{\rho e_{t_p}(\mathbf{u}_p-\mathbf{w}_s)-\left(-p_p\mathbf{I}+M^2\tau_p\right)\cdot\mathbf{u}_p-\mathbf{q}_{e_p}\right\}\cdot\mathbf{n}_p, \tag{2.19}$$

$$\left\{\rho Y_i(\mathbf{u}-\mathbf{w}_s)-\mathbf{q}_i\right\}\cdot\mathbf{n}_p = \left\{\rho Y_{i_p}(\mathbf{u}_p-\mathbf{w}_s)-\mathbf{q}_{i_p}\right\}\cdot\mathbf{n}_p. \tag{2.20}$$

The right-hand side of these equations can be substituted for the corresponding left-hand side terms given in Table 2.2. The assumptions that Equations (2.17) – (2.20) are based on can easily be relaxed to accommodate alternative representations of the space-time interface dynamics. Here they are used to simplify the interphase exchange functions for use in the discrete particle limit.

The general form of the interphase exchange functions can be simplified when fluid elements within the filter volume V_{total} are small relative to the filter width $\delta\mathbf{y}$. In this limit variations in the coordinate $\mathbf{y}$ become small over the spatial intervals occupied by respective particles. Similarly, corresponding variations in the filter kernel also become negligible. In this limit the filter kernel $\mathscr{G}(\mathbf{y}-\mathbf{x},\tau-t;\delta\mathbf{y},\delta\tau)$ may be placed outside of the surface integral given in Equation (2.16). This yields a modified set of source terms of the form

$$\overline{\dot{\mathscr{H}}}_s(\mathbf{x},t) = \underbrace{\int_{-\infty}^{t}\underbrace{\sum_p \mathscr{G}(\mathbf{y}-\mathbf{x},\tau-t;\delta\mathbf{y},\delta\tau)\underbrace{\oint\!\!\oint_{S(\tau)}\vec{\vec{\psi}}(\mathbf{y},\tau)\cdot\mathbf{n}_p\,dS}_{(i)}}_{(ii)}\,d\tau}_{(iii)}. \tag{2.21}$$

Note that this assumption does not imply or require that the multiphase particulates be infinitesimally small or so called "point-particles." The latter is simply a limiting extreme.

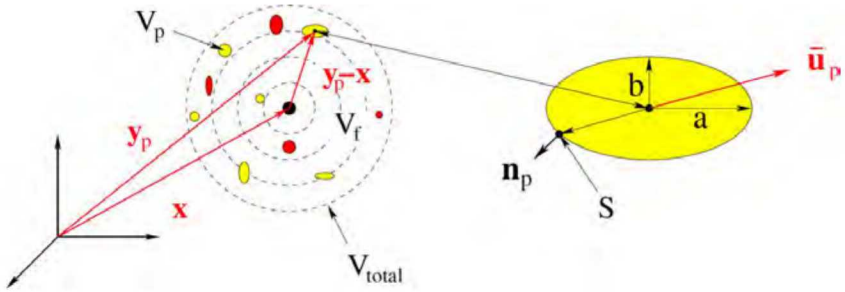

Figure 2.2. Schematic diagram of the hypothetical volume of influence, V_{total}, associated with the filter kernel, $\mathscr{G}(\mathbf{y}-\mathbf{x},\tau-t;\delta\mathbf{y},\delta\tau)$, with discrete time-evolving elliptic particles. Evolution in time within V_{total} is inferred.

With $\mathscr{G}$ moved outside of the surface integral, term (i) in Equation (2.21) now represents the bulk instantaneous exchange rate of mass, momentum, total-energy and chemical species across the surface of each discrete particle "p" at remote points $\mathbf{y}$ and times τ. In a manner analogous to Equation (2.16), term (ii) represents the spatially-filtered effect of the bulk exchange processes associated with all of the particles within V_{total}. Term (iii) represents the time-filtered effect of the small-scale temporal fluctuations associated with (ii) that occur over the interval $-\infty < \tau \leq t$.

In general, discrete multiphase fluid particles can convect and deform in an arbitrary thermophysical state. For modeling purposes, it is necessary to make certain assumptions regarding the precise nature of these dynamic processes. A common assumption is that the particle kinematics and dynamics can be represented by a set of Lagrangian state vectors that are uniquely related to each particle by a single time-evolving point in space. This point is typically the particle centroid, which is denoted $\mathbf{y}_p(\tau)$. Here it is assumed that a particle can be completely characterized as a function of $\mathbf{y}_p$, at remote times τ, by its mass, velocity, total internal energy, and composition. These quantities can be represented by the state vector

$$\bar{\mathbf{s}}(\mathbf{y_p},\tau) = \left[\mathbf{y}_p(\tau), \bar{m}_p(\mathbf{y}_p,\tau), \bar{\mathbf{u}}_p(\mathbf{y}_p,\tau), \bar{e}_{t_p}(\mathbf{y}_p,\tau), \bar{Y}_{i_p}(\mathbf{y}_p,\tau)\right]^T. \tag{2.22}$$

The centroid, $\mathbf{y}_p$, represents the location of respective particles at remote times τ. The bulk surface and volumetric properties must then be related to the time evolving centroid through the specification of a particular geometric configuration.

Particles with any quantifiable geometric form may be considered to within the approximation of Equation (2.21). The most common assumption is that the particles are spherical. An alternative approximation one step more general is to assume that the particles are elliptic and oscillate between the major and minor axes. Figure 2.2 shows a schematic diagram of this precise case. This diagram shows the hypothetical volume of influence, V_{total}, associated with the filter kernel, $\mathscr{G}$, with discrete time-evolving elliptic particles present. As was the case in Figure 2.1, evolution in time within V_{total} is inferred.

Table 2.3. Interphase exchange functions for discrete subfilter particles represented by Equation (2.21).

$\overline{\mathscr{H}}_s(\mathbf{x},t)$	$\oint\!\!\oint_{S(\tau)} \vec{\bar{\psi}}(\mathbf{y}_p,\tau)\cdot\mathbf{n}_p\,dS$
$\overline{\dot{\rho}}_s(\mathbf{x},t)$	$-\left\{\dfrac{d\bar{m}_p}{d\tau}\right\}$
$\overline{\dot{\mathbf{F}}}_s(\mathbf{x},t)$	$-\left\{\dfrac{d\bar{m}_p}{d\tau}\bar{\mathbf{u}}_p+\bar{m}_p\dfrac{d\bar{\mathbf{u}}_p}{d\tau}\right\}$
$\overline{\dot{Q}}_s(\mathbf{x},t)$	$-\left\{\dfrac{d\bar{m}_p}{d\tau}\bar{e}_{t_p}+\bar{m}_p\dfrac{d\bar{e}_{t_p}}{d\tau}\right\}$
$\overline{\dot{\omega}}_{s_i}(\mathbf{x},t)$	$-\left\{\dfrac{d\bar{m}_p}{d\tau}\bar{Y}_{i_p}+\bar{m}_p\dfrac{d\bar{Y}_{i_p}}{d\tau}\right\}$

Evaluation of term (i) in Equation (2.21) requires integration along particle surfaces. From a modeling perspective, it is desirable to formulate the problem in terms of the bulk-average surface properties. These properties can be obtained by applying Leibniz's and Gauss' theorems simultaneously. Consider conservation of mass for a vaporizing particle that is both moving and deforming in an arbitrary state defined by Equation (2.22). Integrating Equation (2.1) over an arbitrary discrete volume V_p gives

$$\underbrace{\iiint_{V_p(\tau)}\frac{\partial\rho_p}{\partial\tau}\,dV}_{(i)}+\underbrace{\iiint_{V_p(\tau)}\nabla_{\mathbf{y}}\cdot(\rho_p\mathbf{u}_p)\,dV}_{(ii)}=0. \tag{2.23}$$

Applying Leibniz's theorem to term (i) gives the relation

$$(i)=\frac{d}{d\tau}\underbrace{\iiint_{V_p(\tau)}\rho_p\,dV}_{\bar{m}_p}-\oint\!\!\oint_{S(\tau)}\rho_p\mathbf{w}_s\cdot\mathbf{n}_p\,dS. \tag{2.24}$$

Similarly, application of Gauss' theorem to term (ii) gives

$$(ii)=\oint\!\!\oint_{S(\tau)}\rho_p\mathbf{u}_p\cdot\mathbf{n}_p\,dS. \tag{2.25}$$

The first term on the right-hand side of Equation (2.24) is the time rate of change of the particle mass, $\bar{m}_p$, as defined in the state vector $\bar{\mathbf{s}}(\mathbf{y_p}, \tau)$ given by Equation (2.22). Substituting Equations (2.24) and (2.25) into (2.23) gives the relation

$$\oint\oint_{S(\tau)} \rho(\mathbf{u}_p - \mathbf{w}_s) \cdot \mathbf{n}_p \, dS = -\frac{d\bar{m}_p}{d\tau}. \tag{2.26}$$

If the thin film approximation is assumed to be valid, the left-hand side of Equation (2.17) can be substituted into the integrand of Equation (2.26). This modified expression corresponds directly to term (i) in Equation (2.21) and relates the exchange of mass between the medium characterized by V_f and the bulk particle vaporization rate $d\bar{m}_p/d\tau$. Similar relations can be derived to relate the surface properties associated with momentum, total-energy and chemical species to the bulk properties represented by $\bar{\mathbf{s}}(\mathbf{y_p}, \tau)$. These relations are summarized in Table 2.3 and provide a modified representation of the interphase exchange functions based on the approximation of Equation (2.21).

Lagrangian Equations of Motion and Transport

In this chapter, we develop the system of Lagrangian particle models following the formulation and framework developed by Oefelein [61, 62, 65]. The primitive system is represented by the Lagrangian state vector

$$\frac{d\mathbf{s}}{dt} = \left[\frac{d\mathbf{y}_p}{dt}, \frac{dm_p}{dt}, \frac{d\mathbf{u}_p}{dt}, \frac{de_{t_p}}{dt}, \frac{dY_{i_p}}{dt}\right]^T. \tag{2.27}$$

In addition, a sub-system of ordinary differential equations are coupled to this primitive system to represent phenomena such as secondary breakup. For convenience, we have dropped the overbear and use t in place of τ to represent time. The governing system is derived based on the assumptions that:

1. The spray is dispersed and that collisions between particles are negligible.
2. Particles associated with the spray can be characterized by equivalent spherical diameters.
3. Particles are small enough to become entrained within the turbulent eddies.
4. Particle motions due to shear flow is negligible.

Under these circumstances, the Lagrangian equations which govern instantaneous particle motion can be written as

$$\frac{d\mathbf{x}_p}{dt} = \mathbf{u}_p \tag{2.28}$$

$$\begin{aligned}\frac{d\mathbf{u}_p}{dt} &= \frac{3}{4}C_D Re_p \frac{\mu}{\rho_p d_p^2}(\mathbf{u}-\mathbf{u}_p) - \frac{1}{\rho_p}\frac{\partial p}{\partial \mathbf{r}} \\ &+ \frac{C_V}{2}\frac{\rho}{\rho_p}\frac{d}{dt}(\mathbf{u}-\mathbf{u}_p) + \frac{9C_B}{\rho_p d_p}\sqrt{\frac{\rho\mu}{\pi}}\int_t^{t+\Delta t}\frac{(d/d\xi)(\mathbf{u}-\mathbf{u}_p)}{\sqrt{t-\xi}}d\xi\end{aligned} \tag{2.29}$$

The Lagrangian equations which govern instantaneous particle mass and heat transfer processes can be written as

$$\frac{dm_p}{dt} = -\dot{m}_p \tag{2.30}$$

$$m_p C_{p_p}\frac{dT_p}{dt} = h_p \pi d_p^2 (T - T_p) - \dot{m}_p \Delta h_v \tag{2.31}$$

The subscript p in these equations denotes values associated with individual fluid particles or drops. The quantity d_p represents the equivalent spherical diameter of a fluid particle with mass m_p; i.e., $d_p = \sqrt[3]{6m_p/\pi\rho_p}$. The terms C_D and Re_p represent the drag coefficient and particle Reynolds number, respectively. The particle Reynolds number is defined as

$$Re_p = \frac{\rho d_p}{\mu}|\mathbf{u}-\mathbf{u}_p| \tag{2.32}$$

The constants C_V and C_B are empirical correction factors that account for inertial effects induced by high Reynolds numbers and rapid particle accelerations. At the conditions of interest, these terms can be approximated as $C_V = C_B = 1$. The terms $\dot{m}_p$, h_p, and Δh_v in Eq. (2.30) and (2.31) represent the vaporization rate, heat transfer coefficient, and enthalpy of vaporization, respectively.

Equation (2.29) was derived by Bassett, Boussinesq, and Oseen [93] and is commonly referred to as the *BBO* equation. The term on the left-hand side represents the particle acceleration or inertial force per unit mass. The terms on the right-hand side represent the force per unit mass due to: 1) skin friction and form drag; 2) static pressure gradients; 3) the inertia of the fluid displaced by the particle; and 4) the forces induced by unsteady flow patterns in the vicinity of the particle. The latter two terms are commonly referred to as the virtual mass and the Bassett forces, respectively. The magnitudes of these forces are proportional to the ratio ρ/ρ_p. At atmospheric pressure, this ratio is typically on the order of 10^{-3} and the virtual mass and Bassett forces are negligible. As pressure is increased, however, the ratio ρ/ρ_p approaches unity and there is a greater need to include these forces in the calculation procedure.

The instantaneous velocity field is simulated using Favre decompositions of the form $\mathbf{u} = \tilde{\mathbf{u}} + \mathbf{u}''$ coupled with SSF methodologies similar to those outlined by [27]. Correlated velocity and scalar fluctuations are generated stochastically as a function of the subfilter variance and covariances using a Cholesky decomposition. The fluctuations are generated at intervals coincident with the eddy-particle interaction time τ_i. The motions of particles are tracked as they traverse a succession of subfilter eddies and particles are assumed to interact with these eddies for a time taken as the smaller of either the eddy lifetime or the characteristic transit time. The eddy lifetime is obtained using the scaling arguments provided by [88].

$$\tau_e = \sqrt{\frac{3}{2}\frac{C_R}{C_I}}\frac{1}{\Pi_{\tilde{\mathbf{S}}}^{\frac{1}{2}}} \tag{2.33}$$

The characteristic transit time is obtained using the linearized form of Eq. (2.29) by considering only the effect of skin friction and form drag since these are the dominating phenomena. This scale is given by

$$\tau_t = -\tau_r \ln\left(1 - \frac{\sqrt{C_R\Delta^2}}{\tau_r|\mathbf{u}-\mathbf{u}_p|}\right), \tag{2.34}$$

where τ_r represents the linearized particle relaxation time given by

$$\tau_r = \frac{4}{3}\frac{\rho_p d_p^2}{\mu}(C_D Re_p)^{-1} \tag{2.35}$$

and $\sqrt{C_R\Delta^2}$ represents the turbulence mixing length scale defined by *LES* framework.

The eddy-particle interaction time is obtained as a function of Eqs. (2.33) and (2.34) using the criteria

$$\tau_i = \begin{cases} \tau_e & \sqrt{C_R\Delta^2} \geq \tau_r|\mathbf{u}-\mathbf{u}_p| \\ \\ \min(\tau_e, \tau_t) & \sqrt{C_R\Delta^2} < \tau_r|\mathbf{u}-\mathbf{u}_p| \end{cases}. \tag{2.36}$$

When $\sqrt{C_R\Delta^2} \geq \tau_r|\mathbf{u}-\mathbf{u}_p|$, Eq. (2.34) has no solution and it is assumed that the particle is entrained within the eddy. For the opposite situation it is assumed that the particle interacts with the eddy for a time taken as the smaller of the eddy lifetime or the characteristic transit time.

Equations (2.28) through (2.31) are evaluated using a fourth-order Runge-Kutta scheme with semi-empirical models employed to quantify the drag coefficient, vaporization rate, and heat transfer coefficient. The models employed to predict these quantities are presented below. Initial conditions for the Lagrangian system involve the specification of initial particle positions, velocities,

masses, and temperatures. This latter quantity is determined at the inlet boundary through the joint specification of a particle size distribution and the mass flow rate $M_p/\Delta t$, where Δt represents the physical time step used for the dual-time Eulerian solver. These quantities are related by Eq. (1.3). Injected particle sizes are assumed to follow an upper limit distribution function. The time step used for Runge-Kutta integration is coupled to the physical time step Δt using the criteria

$$\Delta t_{\text{R-K}} = 10^{-1} \min\{\tau_r, \tau_i, \tau_l, \tau_h, \Delta t\} \tag{2.37}$$

The terms τ_r and τ_i are defined by Eqs. (2.35) and (2.36). The terms τ_l and τ_h represent characteristic time associated with the drop lifetime

$$\tau_l = \frac{m_p}{\dot{m}_p} \tag{2.38}$$

and the characteristic time associated with drop heating

$$\tau_h = -\tau_c \ln\left(1 - \frac{\Delta T_p}{\Delta T_\infty - \dfrac{\tau_c}{\tau_l}\dfrac{\Delta h_v}{C_{p_p}}}\right) \tag{2.39}$$

Here, τ_c represents the characteristic time associated with interfacial heat transfer processes

$$\tau_c = \frac{m_p C_{p_p}}{h_p \pi d_p^2} \tag{2.40}$$

The terms ΔT_p and ΔT_∞ represent the characteristic change in the particle temperature over the interval $t \rightarrow t + \Delta t$ and the initial difference between the ambient fluid temperature and particle temperature, respectively. These terms are derived by linearizing Eqs. (2.30) and (2.31). Using the solution from the previous step as initial conditions, the Lagrangian system is advanced over the interval Δt after each pseudo time iteration performed with the dual-time system. Performing the integration in this manner ensures that both systems converge simultaneously to an accurate solution in a fully coupled manner.

The drag coefficient employed in Eq. (2.29) is evaluated using the correlation proposed by [69]. This correlation describes the influence of pressure and viscous forces acting on the surface of spherical particles. This correlation is given as a function of the drop Reynolds number as

$$C_D^o = \begin{cases} \dfrac{24}{Re_p}\left(1 + \dfrac{1}{6}Re_p^{\frac{2}{3}}\right) & Re_p \leq 10^3 \\ 0.424 & Re_p > 10^3 \end{cases}. \tag{2.41}$$

At subcritical pressures, the assumption of spherical fluid particles is typically valid due to the dominating effects of surface tension. Under such conditions Eq. (2.41) has proven to be quite accurate. Similarly, the solutions of Eqs. (2.30) and (2.31) are dependent upon the specification of drop models which characterize the vaporization rate and heat transfer coefficient. The major assumptions and detailed formulations that describe drop transport models are given by [45], [86], and Faeth [25–27]. These works provide an in-depth analysis of drop vaporization beginning with the classical models derived by [71] and Spalding [94, 95].

To provide a point of reference with respect to established theories at low-pressure, the following correlations are used to model subcritical drop dynamics

$$\dot{m}_{d_{Re_p=0}} = 2\pi\rho_s\mathscr{D}_{sm}d_p\ln(1+B_M) \tag{2.42}$$

$$Nu_{d_{Re_p=0}} = \frac{2\ln(1+B_M)^{Le^{-1}}}{(1+B_M)^{Le^{-1}}-1} \tag{2.43}$$

The term $\dot{m}_{d_{Re_p=0}}$ represents the vaporization rate in a quiescent environment and $Nu_{d_{Re_p=0}}$ represents the corresponding Nusselt number. The quantity $Le = \lambda_s/\rho_s C_p \mathscr{D}_{sm}$ represents the Lewis number where here the subscript s refers to the vapor mixture at the drop surface. The quantity

$$B_M = \frac{Y_{d_s} - Y_{d_\infty}}{1 - Y_{d_s}} \tag{2.44}$$

represents the Spalding transfer number, and Y_{d_s} and Y_{d_∞} represent the mass fraction associated with the particulate phase at the drop surface and within the ambient fluid, respectively. The Spalding transfer number is evaluated by means of the relation

$$\ln(1+B_M) = Le\ln(1+B_T) \tag{2.45}$$

where for the low-pressure case

$$B_T = \frac{C_p(T_\infty - T_s)}{\Delta h_v} \tag{2.46}$$

Equations (2.44) through (2.46) provide the functional relationship between the surface temperature T_s and mass fraction Y_{d_s}. This system is closed using the property evaluation scheme and phase equilibrium theory outlined in Section 3.1.

To account for convective effects the multiplicative correction factors proposed by [28] are employed. These factors take the form

$$\frac{\dot{m}_p}{\dot{m}_{d_{Re_p=0}}} = 1+\frac{0.278Re_p^{1/2}Sc^{1/3}}{[1+1.232/Re_pSc^{4/3}]^{1/2}} \tag{2.47}$$

$$\frac{h_p}{h_{d_{Re_p=0}}} = 1+\frac{0.278Re_p^{1/2}Pr^{1/3}}{[1+1.232/Re_pPr^{4/3}]^{1/2}} \tag{2.48}$$

where $Sc = \mu_s/\rho_s\mathscr{D}_{sm}$ and $Pr = \mu_s C_p/\lambda_s$ represent the Schmidt and Prandtl numbers, respectively.

The system of models described above is summarized below in dimensionless form as follows. The instantanesous particle momentum in the Lagrangian-Particle limit is given by

$$\frac{d\mathbf{u}_p}{dt} = \frac{\tau_f}{\tau_r}(\mathbf{u}-\mathbf{u}_p)+\cdots, \tag{2.49}$$

where

$$\frac{\tau_r}{\tau_f} = \frac{St}{(1+aRe_p^b)}, \qquad St = \frac{\tau_p}{\tau_f} = \frac{1}{18}\rho_p d_p^2 Re, \text{ and} \qquad Re_p = d_p Re\left|\mathbf{u}-\mathbf{u}_p\right|.$$

Key assumptions associated with these equations are: 1) that the particle density is much greater than carrier fluid, 2) particle motion due to shear is negligible, and that the particles are dispersed and wake interactions are negligible. The instantaneous particle mass and energy in respective order are

$$\frac{dm_p}{dt} = -\frac{\tau_f}{\tau_l}m_p \tag{2.50}$$

and

$$\frac{dT_p}{dt} = \frac{\tau_f}{\tau_c}(T-T_{p_s}) - \frac{\tau_f}{\tau_l}\frac{\Delta h_{v_p}}{C_{p_p}}. \tag{2.51}$$

Here it is assumed that the composition of bulk liquid remains at the injection condition, surface composition varies as dictated by local phase equilibrium conditions, the vaporization rate and heat transfer coefficient are derived in closed form for spherically symmetric, $Re_p = 0$, quasi-steady flow. Multiplicative correction factors are then applied to account for convective effects and particle asymmetries. The characteristic time scales are for the drop lifetime and heating are

$$\frac{\tau_f}{\tau_l} = \frac{12}{\rho_p d_p^2} \frac{\mu_s}{Sc_s Re} \ln(1+B_M) f(Re_p, Sc_s), \text{ and} \tag{2.52}$$

$$\frac{\tau_f}{\tau_c} = \frac{12}{\rho_p d_p^2} \frac{\mu_s}{Pr_s Re} \frac{\ln(1+B_M)^{Le_s{}^{-1}}}{(1+B_M)^{Le_s{}^{-1}} - 1} f(Re_p, Pr_s). \tag{2.53}$$

The related convective correction factors and transfer numbers are

$$f(Re_p, [Sc_s \text{ or } Pr_s]) = 1 + \frac{0.278 Re_p{}^{1/2} [Sc_s \text{ or } Pr_s]^{1/3}}{\sqrt{1 + 1.232/Re_p [Sc_s \text{ or } Pr_s]^{1/3}}}, \text{ and} \tag{2.54}$$

$$B_M = \frac{Y_{p_s} - Y_p}{1 - Y_{p_s}} \qquad B_T = \frac{C_{p_p}}{\Delta h_{v_p}} (T - T_{p_s}). \tag{2.55}$$

The transfer numbers are related as follows

$$B_M = (1+B_T)^{Le_s} - 1 \tag{2.56}$$

Real-Fluid Thermodynamic Property Modeling

Our model provides a generalized treatment of the equation of state, thermodynamics, and transport processes at all pressure conditions for any mixture of relevance here. To account for thermodynamic non-idealities and transport anomalies over a wide range of pressures and temperatures, we apply an extended corresponding-states principle similar to that developed by Rowlinson and Watson [79]. A 32-term Benedict-Webb-Rubin (*BWR*) equation of state is used to predict the pressure-volume-temperature (*PVT*) behavior of the liquid-phase, saturated vapor mixtures, and gas phase properties. Use of modified *BWR* equations of state has been shown to provide consistently accurate results over the widest range of pressures, temperatures, and mixture states, especially at saturated conditions.

The law of corresponding-states expresses the generalization that equilibrium properties which depend on intermolecular forces are related to the critical properties in a universal way. In 1873, van der Waals showed that this law is theoretically valid for all pure substances whose *PVT* properties can be expressed in terms of a two-constant equation of state [107]. In 1939, Pitzer showed that this law is similarly valid for substances which can be described by a two parameter intermolecular potential function [68]. The corresponding-states principle holds well for fluids containing simple molecules and, upon semi-empirical extension, also holds for more complex mixtures.

The corresponding-states model used in this study is based on three assumptions: 1) the configurational properties of a single phase mixture η_m can be equated to those of a hypothetical pure fluid; i.e.,

$$\eta_m(\rho, T, X_1, \ldots, X_N) = \eta_x(\rho, T) \tag{2.57}$$

2) the properties of the hypothetical pure fluid obey classical two parameter corresponding-states formalism

$$\eta_x(\rho, T) = \eta_o F_\eta(W_o, W_x, \hbar_x, f_x) \tag{2.58}$$

where η_o corresponds to a reference fluid; and 3) the reference fluid density and temperature, ρ_o and T_o, obey an extended equilibrium corresponding-states principle given by

$$\rho_o = \rho\, \hbar_x \qquad T_o = T/f_x \tag{2.59}$$

The terms $\hbar_x$, f_x and W_x in (2.57)–(2.59) are, respectively, the equivalent substance volume reducing ratio, the equivalent substance temperature reducing ratio, and molecular weight for the multi-component mixture. The equivalent substance volume reducing ratio accounts for the distribution of energy with respect to the reference fluid. The temperature reducing ratio accounts for molecular size differences. F_η in (2.58) is a dimensional scaling factor. The functional forms of these parameters are described below.

Implementation of the corresponding-states methodology requires the selection of a reference fluid. In this study methane is employed for two reasons. First, a reliable database exists with sufficient data correlated for the equation of state and relevant thermodynamic and transport properties. Second, it is similar in structure to the chemical systems of interest.

To apply the model to mixtures, analytical expressions for F_η must be specified along with a set of mixing and combining rules for $\hbar_x$, f_x and W_x, a reference fluid equation of state, and relevant property data for the reference fluid. Following [47], the mixing rules employed are as follows

$$\hbar_x = \sum_{i=1}^{N} \sum_{j=1}^{N} X_i X_j\, \hbar_{ij} \tag{2.60}$$

$$f_x = \hbar_x^{-1} \sum_{i=1}^{N} \sum_{j=1}^{N} X_i X_j f_{ij}\, \hbar_{ij} \tag{2.61}$$

$$W_x^{n/2} f_x^{1/2}\, \hbar_x^{-4/3} = \sum_{i=1}^{N} \sum_{j=1}^{N} X_i X_j W_{ij}^{n/2} f_{ij}^{1/2}\, \hbar_{ij}^{-4/3} \tag{2.62}$$

where subscript ij corresponds to binary pair parameters. Combining rules for these terms are given by

$$\hbar_{ij} = \frac{1}{8}\left(\hbar_i^{1/3} + \hbar_j^{1/3}\right)^3 (1-\ell_{ij}) \tag{2.63}$$

$$f_{ij} = \left(f_i f_j\right)^{\frac{1}{2}} (1-k_{ij}) \tag{2.64}$$

$$W_{ij} = \frac{2W_iW_j}{W_i+W_j} \tag{2.65}$$

In (2.63) and (2.64), the quantities l_{ij} and k_{ij} represent binary interaction parameters which account for molecular energy and volumetric effects in the binary system. The quantities $\hbar_i$ and f_i are the equivalent substance reducing ratios for compound i in the mixture. These quantities are obtained by a two-parameter methodology as follows

$$\hbar_i = \left(\frac{V_{c,i}}{V_{c,o}}\right)\phi_i(V_{r,i}, T_{r,i}, \omega_i) \tag{2.66}$$

$$f_i = \left(\frac{T_{c,i}}{T_{c,o}}\right)\theta_i(V_{r,i}, T_{r,i}, \omega_i) \tag{2.67}$$

Functions ϕ_i and θ_i are shape factors [31, 46] which account for non-sphericity with respect to molecular structure. Subscript c denotes a critical value, r a reduced value.

The functional form of the *BWR* equation of state is

$$p(\rho,T) = \sum_{n=1}^{9} a_n(T)\rho^n + \sum_{n=10}^{15} a_n(T)\rho^{2n-17}\exp -\gamma\rho^2 \tag{2.68}$$

where γ is an empirically fitted parameter termed the strain rate. Coefficients a_n are functions of

temperature and R_u is the universal gas constant. These quantities are given as

$$
\begin{aligned}
a_1(T) &= R_u T \\
a_2(T) &= N_1 T + N_2 T^{1/2} + N_3 + N_4/T + N_5/T^2 \\
a_3(T) &= N_6 T + N_7 + N_8/T + N_9/T^2 \\
a_4(T) &= N_{10} T + N_{11} + N_{12}/T \\
a_5(T) &= N_{13} \\
a_6(T) &= N_{14}/T + N_{15}/T^2 \\
a_7(T) &= N_{16}/T \\
a_8(T) &= N_{17}/T + N_{18}/T^2 \\
a_9(T) &= N_{19}/T^2 \\
a_{10}(T) &= N_{20}/T^2 + N_{21}/T^3 \\
a_{11}(T) &= N_{22}/T^2 + N_{23}/T^4 \\
a_{12}(T) &= N_{24}/T^2 + N_{25}/T^3 \\
a_{13}(T) &= N_{26}/T^2 + N_{27}/T^4 \\
a_{14}(T) &= N_{28}/T^2 + N_{29}/T^3 \\
a_{15}(T) &= N_{30}/T^2 + N_{31}/T^3 + N_{32}/T^4
\end{aligned}
$$

Equation (2.59) coupled with (2.68) and the mixing rules given by (2.60)–(2.62) are used to obtain the *PVT* behavior for the multi-component system considered in this study.

Explicit expressions for the enthalpy, Gibbs energy, and constant pressure specific heat are required as a function of temperature and pressure. Having established an analytical representation for real mixture *PVT* behavior, these properties are obtained using a two step process. First, respective reference properties are transformed to those for the mixture at a given pressure using the corresponding-states methodology outlined above. The equation of state is then employed to obtain a pressure correction using departure functions of the form given by (2.70)–(2.71) [72]. These functions describe the deviation of known reference values with respect to pressure at a given temperature and composition. They are derived by means of the Maxwell relations [106, Chapter 10].

$$\Delta H = -\int_{\infty}^{V} \left(p - \frac{RT}{V} \right) dV + T \int_{\infty}^{V} \left[\left(\frac{\partial p}{\partial V} \right)_V - \frac{R}{V} \right] dV + RT(Z-1) \tag{2.69}$$

$$\Delta G = -\int_{\infty}^{V} \left(p - \frac{RT}{V} \right) dV - RT \ln \left(\frac{V}{V_o} \right) + RT(Z-1) \tag{2.70}$$

$$\Delta C_p = T \int_{\infty}^{V} \left(\frac{\partial^2 p}{\partial T^2} \right) dV - \frac{T(\partial p/\partial V)_V^2}{(\partial p/\partial V)_T} - R \tag{2.71}$$

The viscosity μ and thermal conductivity λ are obtained using the methodologies developed by Ely and Hanley [23, 24]. Equations (2.57)–(2.65) are employed with scaling factors of the form

$$F_\mu = \left(\frac{W_x}{W_o} \right)^{\frac{1}{2}} f_x^{\frac{1}{2}} \, \hbar_x^{-\frac{2}{3}} \tag{2.72}$$

$$F_\lambda = \left(\frac{W_o}{W_x}\right)^{\frac{1}{2}} f_x^{\frac{1}{2}} \hbar_x^{-\frac{2}{3}} \tag{2.73}$$

using values of $n = 1$ and $n = -1$, respectively, in Eq. (2.62).

For mixtures of molecules of substantially different size; i.e., when the difference between two binary species approaches volumetric ratios on the order $V_{c,1}/V_{c,2} \sim 6$, the mean density approximation given by Eq. (2.57) fails. Since most thermo-physical properties are determined from relatively short range forces, the properties of the larger component dominate. To correct for this effect in the prediction of mixture viscosity, Eq. (2.72) is used together with an Enskog correction of the form given by Ely and Hanley [23]

$$\mu = \mu_o(\rho_o, T_o) F_\mu + \Delta\mu^{ENSKOG} \tag{2.74}$$

This correction has been shown to improve predictions for mixtures which exhibit large size and mass differences for both dense and dilute gas states.

In a similar manner, Ely and Hanley [24] propose an expression of the form

$$\lambda = \lambda_o(\rho_o, T_o) F_\lambda + \lambda''(T) + \Delta\lambda_{crit}(\rho, T) \tag{2.75}$$

for thermal conductivity. The first term on the right-hand side accounts for purely collisional and transitional effects. The second term accounts for transfer of energy due to internal degrees of freedom. This term is modeled by means of a modified Eucken correlation with an empirical mixing rule for polyatomic gases [72]. The last term in Eq. (2.75) accounts for near critical effects.

The effective diffusion coefficient $\mathscr{D}_{im}$ for each species i is related to the binary diffusion coefficients $\mathscr{D}_{ij}$ of the mixture using the formula given by Bird [4, Chapter 16]

$$\mathscr{D}_{im,g} = \frac{(1 - X_i)}{\sum_{\substack{j=1 \\ j \neq i}}^{N} \left(\frac{X_j}{\mathscr{D}_{ij}}\right)} \tag{2.76}$$

Theory describing diffusion in binary gas mixtures at low to moderate pressures has been well developed [72]. At low pressures, these coefficients vary inversely with pressure or density and are essentially independent of composition. At high pressure, however, the product $\mathscr{D}_{ij} p$ (or $\mathscr{D}_{ij}\rho$) is no longer constant. For this situation, these products decrease with increasing pressure (or density) and are dependent on composition. Thus, binary mass diffusivities are obtained by means of a two step approach. First, low-pressure theory is employed using Chapman-Enskog theory coupled with the Lennard-Jones intermolecular potential functions. A high pressure correction is then applied using the corresponding-states methodology proposed by Takahashi [96].

Vapor Liquid Equilibrium Theory

The real-fluid model for multicomponent mixtures is applied to obtain vapor-liquid equilibrium conditions. Assuming that the liquid (L) is in thermodynamic equilibrium with its vapor (V), the equilibrium conditions are

$$\begin{aligned} T^V &= T^L \\ p^V &= p^L \\ \mu_i^V &= \mu_i^L \end{aligned} \tag{2.77}$$

with T as the temperature, p as the pressure, and μ_i as the chemical potential of species i. In contrast to cubic equations of state, the applied BWR equation of state has shown to accurately predict saturated liquid properties (e.g., density) over the widest range of pressures and temperatures. Therefore, accurate vapor-liquid equilibrium conditions can be computed which serve to calculate latent heat values and Spalding transfer numbers as utilized in Eqs. (2.51), (2.52), and (2.53).

Modeling Surface Tension Forces in Multi-Component Mixtures

Gradient Theory provides a widely accepted methodology to calculate detailed interface structures and surface tension forces between gases and liquids [6, 50, 57, 78, 105]. The foundation of this theory was established by van der Waals in 1893 [78, 105] and reformulated later by Cahn and Hilliard in 1958 [6]. At thermodynamic equilibrium, the model has been shown in detail to be equivalent to mean-field molecular theories of capillarity and it has been successfully applied to a wide variety of fluids: e.g., hydrocarbons and their mixtures, polar compounds and their mixtures, polymer and polymer melts, vapor-liquid and liquid-liquid interfaces. Most recently, Gradient Theory has been successfully compared to Monte Carlo simulations of vapor-liquid and liquid-liquid interfaces [56, 58, 60]. The theory proved successful in capturing both surface tension forces and details of vapor-liquid molecular interfacial structures. The spatial dimensions of vapor-liquid interfaces can carry important implications for high-pressure liquid injection processes[10, 11, 17, 54, 63, 64]

To simplify the calculations without loss of validity, we employ Linear Gradient Theory (LGT). LGT is derived from Gradient Theory by assuming a linearized minimization function of the Helmholtz free energy density distribution across the vapor-liquid interface for the calculation of the interfacial density profiles. It has proven successful for calculating binary and multicomponent interface states of the kind considered here [81, 114]. The Helmholtz free energy density for a mixture is expanded as a Taylor series and truncated at lower spatial derivatives of density

$$F = \int \left[f_0(\rho_M) + \sum_{i,j} \frac{1}{2} \kappa_{ij} \nabla \rho_{M,i} \nabla \rho_{M,j} \right] ds \tag{2.78}$$

with F defined as the Helmholtz free energy, $f_0(\rho)$ the Helmholtz free energy density of a homogeneous fluid, ρ_M the molar density, and s the volume unit. The influence parameter of the inhomogeneous fluid is denoted κ and carries the molecular structure information of the interface. This in turn determines the density gradients response to local deviations of the chemical potentials from their bulk value. The interfacial profile of a planar multicomponent gas-liquid interface in equilibrium is then obtained by assuming the influence parameter to be density-independent [55] and by minimizing the Helmholtz free energy according to the equation [50, 57]

$$\sum_i \sum_j \frac{1}{2} \kappa_{ij} \frac{d\rho_{M,i}}{dz} \frac{d\rho_{M,j}}{dz} = \bar{\omega}(\rho_M) - \bar{\omega}_s \tag{2.79}$$

with z as the normal interface direction and $\bar{\omega}_s = -p_s$ as the equilibrium pressure. The grand thermodynamic potential energy density is defined as

$$\bar{\omega}(\rho_M) = f_0(\rho_M) - \sum_i \rho_{M,i} \mu_{i,B} \tag{2.80}$$

with $\mu_{i,B}$ as the chemical potential of species i in the bulk phase. According to Gradient Theory, the surface tension and spatial interface dimension z can be calculated once the species density profiles within the interface are known

$$\sigma = \int_{\rho_{I,V}}^{\rho_{I,L}} \sqrt{2\left(\bar{\omega}(\rho_M) - \bar{\omega}_s\right) \sum_i \sum_j \kappa_{ij} \frac{d\rho_i}{d\rho_I} \frac{d\rho_j}{d\rho_I}} d\rho_I \tag{2.81}$$

and

$$z = z_0 + \int_{\rho_{I,0}}^{\rho_I} \sqrt{\frac{\sum_i \sum_j \kappa_{ij} \frac{d\rho_i}{d\rho_I} \frac{d\rho_j}{d\rho_I}}{2\left(\bar{\omega}(\rho_M) - \bar{\omega}_s\right)}} d\rho_I \tag{2.82}$$

with subscripts I as the reference component. The cross influence parameter κ_{ij} is calculated following Lin *et al.* [50]. For temperatures higher than the critical temperature of the vapor component, the corresponding parameter is set to a single value, consistent with suggestions from Zuo and Stenby [114]. This method has found wide acceptance and has also been adopted here. However, more suitable and generalized methods have also been most recently proposed [9]. The boundary conditions of the bulk vapor and liquid phases, referred to by indices V and L in Eq. (2.81), are obtained from real-fluid multicomponent vapor-liquid equilibrium calculations. The species density profiles across the molecular interface are obtained in relation to the chosen reference species and the respective composition of the bulk vapor and liquid phases as follows

$$\frac{d\rho_i}{d\rho_I} = \frac{\rho_{i,L} - \rho_{i,V}}{\rho_{I,L} - \rho_{I,V}} \tag{2.83}$$

Breakup Modeling of Evaporating Drops

In the following, the modeling framework for the simulation of drop distortion and breakup is presented. Dynamics of drop oscillations and deformations are captured with the Taylor Analogy Breakup (TAB) model, originally proposed by O'Rourke and Amsden [67]. It is built upon Taylor's analogy between drop dynamics and a forced spring-mass-damper system [100]. This model is applied in combination with frameworks of large eddy simulations and real-fluid thermodynamics and Gradient Theory in order to predict the local and unsteady forces on the drops and to accurately capture their dynamic responses. A new framework has been developed in which the distortion model is fully coupled to the mass, momentum, and energy transfer functions. The breakup event is modeled by a new set of equations to accurately predict the properties of newly created drops over the full range of conditions under which the TAB model is applicable. This refined model is entirely derived from conservation equations for mass, momentum, and energy and does not, as a consequence, introduce new modeling constants.

The Taylor Analogy Breakup Model

The model assumes, consistent with the Taylor analogy, that simulations of drop deformations and oscillations can be facilitated by an one-dimensional forced mass-spring-damper surrogate model. It is further assumed that drop oscillations can be sufficiently described by considering only the first (fundamental) deformation mode of an oscillating sphere and that higher modes can be neglected. Over-damped conditions result in drop deformations while under-damped drop dynamics result in harmonic oscillations with an amplitude and frequency dependent on the fluid dynamic forcing and the systems natural resonant frequency and damping. Drop breakup is assumed to occur when oscillations of the drop poles meet at its center.

The fundamental equation of the utilized forced mass-spring-damper system reads [67]

$$\frac{d^2y}{dt^2} = \frac{C_F}{C_b}\frac{\rho_g}{\rho_l}\frac{V_{slip}^2}{r^2} - \frac{C_K\sigma}{\rho_l r^3}y - \frac{C_d\mu_l}{\rho_l r^2}\frac{dy}{dt} \tag{2.84}$$

with ρ_g and ρ_l as the ambient gas and liquid drop density, V_{slip} as the slip velocity between the gaseous flow and the drop translational motion, r as the drop radius, σ as the surface tension, and with μ_l as the liquid drop viscosity. The non-dimensional distortion of the drop poles is defined as

$$y = \frac{x}{C_b r} \tag{2.85}$$

with x as the distance between the dynamic position of the drop pole and its original position in its spherical shape. These quantities are dynamically determined during the simulation from high-fidelity large-eddy simulations and from real-fluid thermodynamics. The first term on the right-hand-side of Eq. (2.84) represents the fluid dynamic force. The second and third term on

C_F	C_K	C_d	C_b
1/3	8	5	0.5

Table 2.4. Modeling constants of the TAB model, rigorously determined by Lamb.

the right-hand-side model the liquid drop analogies to a spring and damper, respectively. The coefficients C_F, C_K, C_d, and C_b are given in Table 2.4 and have been rigorously determined by Lamb [43]. These coefficients are chosen to match the known oscillation dynamics of inviscid ($C_K = 8$) and damped viscous drops ($C_d = 5$) and to match the experimentally verified critical Weber number of $We_{crit} = 12$ of low viscosity Newtonian liquids below which breakup does not occur ($C_F = 1/3$ assuming $C_b = 0.5$ and $C_K = 8$ as demonstrated below) in the drop deformation and breakup regime map of Hsiang and Faeth [38]. Using these definitions, breakup occurs if the non-dimensional drop distortion y exceeds unity. After integration and discretization of Eq. (2.84), the final form of the modeling framework is obtained [67]

$$y(t) = We_c + \exp(-\frac{\Delta t}{t_D}) \left[(y_0 - We_c)\cos(\omega \Delta t) + \frac{1}{\omega}(\frac{dy_0}{dt} + \frac{y_0 - We_c}{t_D})\sin(\omega \Delta t) \right] \tag{2.86}$$

with y_0 and dy_0/dt as the drop distortion and distortion velocity at the beginning of the time step. The remaining terms in Eq. (2.86) are assumed constant over each time step and are defined as follows. The reduced Weber number is denoted as

$$We_c = \frac{C_F}{C_K C_b} We^\star \tag{2.87}$$

The effective Weber number $We^\star$ is scaled by the Ohnesorge number to account for its generally accepted effect on the critical Weber number below which breakup does not occur [5, 38]

$$We^\star = \frac{We}{1 + 1.077 \cdot Oh^{1.6}} \tag{2.88}$$

The Ohnesorge number is defined as

$$Oh = \frac{\mu_l}{\sqrt{\rho_l D \sigma}} \tag{2.89}$$

with D as the drop diameter. The Weber number is defined based on the radius of the drop as

$$We = \frac{\rho_g V_{slip}^2 r}{\sigma} \tag{2.90}$$

In Eq. (2.86), t_D denotes the oscillation damping time which reads, based on Eq. (2.84),

$$t_D = \frac{2\rho_l r^2}{C_d \mu_l} \tag{2.91}$$

The drop oscillation frequency is then defined as

$$\omega = \sqrt{C_K \frac{\sigma}{\rho_l r^3} - \frac{1}{t_D^2}} \tag{2.92}$$

Based on Eqs. (2.86) and (2.84), the equation for the discretized drop distortion velocity can be obtained [67]

$$\frac{dy}{dt} = \frac{We_c - y}{t_D} + \omega \exp(\frac{-\Delta t}{t_D}) \left[\frac{1}{\omega} \left(\frac{dy_0}{dt} + \frac{y_0 - We_c}{t_D} \right) \cos(\omega \Delta t) - (y_0 - We_c) \sin(\omega \Delta t) \right] \tag{2.93}$$

With these introduced definitions, the corresponding breakup times of this framework can be determined. The breakup time is defined as the period between the initiation of aerodynamic forces on an initially undistorted and non-oscillating drop and the time when drop breakup occurs ($y > 1$). In the low Weber number breakup regime, when the Weber number is of the order of the critical Weber number, the breakup time t_B can be determined from Eq. (2.86) by assuming

$$\omega \cdot t_B = \pi \quad \rightarrow We \sim o(We_c) \tag{2.94}$$

which, with the already defined oscillation frequency of an unviscid liquid and with $C_K = 8$, compare Eq. (2.92) and Table 2.4, results in

$$t_B(We \sim We_c) = \frac{\pi}{2} \sqrt{\frac{\rho_l r^3}{2\sigma}} \tag{2.95}$$

This breakup time agrees with the experimentally observed breakup time in the bag breakup regime ($We_c < We < 100$) [38]. For high Weber numbers, drop breakup occurs almost immediately after the initiation of aerodynamic forcing. This corresponds to the following assumption for the breakup time

$$\omega \cdot t_B \ll 1 \quad \rightarrow We \gg 1 \tag{2.96}$$

Inserting this assumption into Eq. (2.86) results in

$$t_B(We \gg 1) = \sqrt{3} \frac{r}{V_{slip}} \sqrt{\frac{\rho_l}{\rho_g}} \tag{2.97}$$

This breakup time agrees with the experimentally observed breakup time in the stripping breakup regime ($100 < We < 350$) [38]. As a consequence, the TAB model is valid to model corresponding drop dynamics for a wide range of Ohnesorge numbers. At higher Weber numbers, however, breakup is increasingly determined by surface stripping and drop shattering processes for which TAB's forced spring-mass-damper system is not necessarily a meaningful surrogate model.

Interaction of Mass, Momentum, and Energy in Oscillating Drops

In what follows, a framework is presented which accurately and efficiently couples the TAB equations for drop distortion and oscillations, along with effects of internal flow dynamics, to the equations for drop momentum, evaporation, and heat transfer. The starting point of the momentum coupling model is the "standard drag curve" which assumes solid particles (referred to by index "s") of perfect spherical shape (referred to by index "sph"). This drag law is defined as

$$C_{d,s,sph} = \frac{24}{Re}(1 + 0.15 \cdot Re^{0.287}) \tag{2.98}$$

Based on drag measurements of free-falling, evaporating and burning drops of various liquids in hot air from Eisenklam *et al.* [21, 22], Yuen and Chen have established that Eq. (2.98) remains valid for evaporating drops if the Reynolds number is properly scaled by the average gas film dynamic viscosity [113]. The corresponding underlying drop boundary film theory was developed by Abramzon and Sirignano [1]. The calculation is facilitated by the "1/3" rule, established by Hubbard *et al.* [40]. According to the "1/3"-rule, the average gas film temperature T_{av} and mixture composition $x_{i,av}$ is calculated as follows

$$T_{av} = T_d + \frac{1}{3}(T_\infty - T_d) \tag{2.99}$$

and

$$x_{i,av} = x_{i,d} + \frac{1}{3}(x_{i,\infty} - x_{i,d}) \tag{2.100}$$

Then, the average gas film viscosity μ_{av} is calculated accordingly using the real-fluid thermodynamics framework, presented in Sec. 2, which results in the calculation of the effective Reynolds number.

$$Re = \frac{\rho_g D\,|u - u_d|}{\mu_{av}} = \frac{\rho_g D V_{slip}}{\mu_{av}} \tag{2.101}$$

Next, the drag coefficient calculated from Eq. (2.98) is corrected to account for internal flow patterns which form, in contrast to solid spheres, in viscous spheres. This correction is built upon the

analytical solution of hydrodynamic forces on viscous ("vis") spheres ("sph") for creeping flows by Hadamard and Rybczynski as presented by Sirignano [87].

$$C^{\star}_{d,vis,sph} = \frac{8}{Re}\left(\frac{3\lambda+2}{\lambda+1}\right) \qquad \rightarrow Re \ll 1 \tag{2.102}$$

with the parameter λ defined as the viscosity ratio

$$\lambda = \frac{\mu_d}{\mu_g} \tag{2.103}$$

and with μ_d and μ_g as the viscosities of the drop and of the ambient gas, respectively. While numerous expressions for the drag coefficient of solid spheres ($\lambda \rightarrow \infty$) and bubbles ($\lambda = 0$) exist, a recent study from Feng and Michaelides developed one of the few fundamentally consistent correlation formula which applies to finite viscosity ratios [30]. Their correlation formula is utilized here to lift the underlying assumption of Eq. (2.98) of a rigid sphere to include the effect of internal drop flow fields at finite drop viscosity ("vis") on the drag coefficient as follows

$$C_{d,vis,sph} = \frac{2-\lambda}{2}C_{d,b} + \frac{4\lambda}{6+\lambda}C_{d,2} \qquad (0 \leq \lambda \leq 2;\ 5 < Re < 1000) \tag{2.104}$$

which applies at low viscosity ratios. For higher viscosity ratios, the following equation is valid

$$C_{d,vis,sph} = \frac{4}{\lambda+2}C_{d,2} + \frac{\lambda-2}{\lambda+2}C_{d,s,sph} \qquad (2 \leq \lambda < \infty;\ 5 < Re < 1000) \tag{2.105}$$

which applies for the same Reynolds number range. Note that the Reynolds number is calculated from the "1/3"-rule as defined in Eq. (2.101) to properly include the effect of evaporation on the solid sphere reference state, utilized in Eq. (2.105). In the equations above, the drag coefficient of a bubble ($\lambda = 0$) is related to the drag coefficient of a solid sphere, based on Eq. (2.102), as follows

$$C_{d,b} = \frac{16}{24}C_{d,s,sph} \tag{2.106}$$

The drag coefficient of a sphere with an intermediate viscosity ratio $\lambda = 2$ is defined as [30]

$$C_{d,2} = 17 \cdot Re^{-2/3} \tag{2.107}$$

while the drag coefficient of a solid sphere ($\lambda \rightarrow \infty$) has already been defined in Eq. (2.98). Feng and Michaelides also offer an equation for the low Reynolds number range ($Re \leq 5$) [30] which is utilized in analogy to the equations above. Note that the correlations presented by Eqs. (2.104) and (2.105) demonstrated a maximal fractional difference and a standard deviation of all fractional

differences from the reference solution of 4.6 percent and 2.1 percent, respectively [30]. The reference solution has been obtained by 3-D direct numerical simulations of the Navier-Stokes equations around a sphere at various Reynolds numbers. Building on these correlations, the momentum coupling model is finalized by lifting the still present underlying assumption of a spherical drop shape in those equations. Most recently, detailed 3-D direct numerical simulations of flows around non-spherical objects were performed by Richter and Nikrityuk [77]. Their work built on related previous studies from Haider and Levenspiel [34] and later from Hölzer and Sommerfeld [37], whose regression formula were shown, however, to suffer from substantial uncertainties [32]. The regression model, presented by Richter and Nikrityuk, which is utilized here, however, has demonstrated the capability to predict 99.8 percent of the variance of the drag coefficient. It reads [77]

$$\frac{C_{d,s}}{C_{d,s,sph}} = \frac{0.21 + \frac{20}{Re}\left(\frac{\ell}{d}\right)^{0.58} + \frac{6.9}{\sqrt{Re}}\left(\frac{\ell}{d}\right)^{-1.4}}{0.21 + \frac{20}{Re} + \frac{6.9}{\sqrt{Re}}} \tag{2.108}$$

which leads to the final correction to the drag law

$$C_d = C_{d,vis,sph} \cdot \frac{0.21 + \frac{20}{Re}\left(\frac{\ell}{d}\right)^{0.58} + \frac{6.9}{\sqrt{Re}}\left(\frac{\ell}{d}\right)^{-1.4}}{0.21 + \frac{20}{Re} + \frac{6.9}{\sqrt{Re}}} \tag{2.109}$$

in which the reference drag coefficient of the viscous sphere $C_{d,vis,sph}$ is modified according to the spanwise length ℓ of the deformed drop defined below, normalized by the diameter d of the volume-equivalent sphere. It is worth mentioning that the study from Richter and Nikrityuk specifically included a sphere which was deformed into volume-equivalent spheroids. This deformation accurately resembles the corresponding distortion modeled by TAB. As a consequence, the spanwise length ℓ can be calculated from the normalized distortion y, compare Eq. (2.86), as follows

$$\ell = 2(r - x) = 2r(1 - C_b y) \tag{2.110}$$

These modifications to the drag law alter the characteristic time scale of the instantaneous particle momentum, given by Eq. (2.49) which has assumed solid and spherical drops, as follows

$$\frac{\tau_f}{\tau_r} = \left.\frac{\tau_f}{\tau_r}\right|_{s,sph} \cdot \frac{C_d}{C_{d,s,sph}} \tag{2.111}$$

with C_d defined in Eq. (2.109) and with $C_{d,s,sph}$ defined in Eq. (2.98), respectively. This modified characteristic time scale also enters into the scheme for the determination of the time step used for Runge-Kutta integration as defined in Eq. (2.37). It is important to note that these modifications to

the drag law do not enter into TAB model since its constants have already been, as discussed above, rigorously established in order to match well-known drop deformation and oscillation dynamics. As a consequence, these constants already consider much of the discussed physical complexity.

Fully consistent with the momentum coupling approach, the corresponding model for the mass and energy equations is derived. Starting point of this model are the equations for drop evaporation and heating, already defined in Eqs. (2.52), (2.53), and (2.43). The corresponding Reynolds, Schmidt, and Prandtl numbers are calculated as average gas film quantities as defined above to properly consider effects of drop evaporation. Next, the drop heat and mass transfer coefficients are modified to include the effect of the internal drop flow which forms due to the finite viscosity of liquid drops. Consistent with the respective momentum correction, the correction for the effective Nusselt number for viscous ("vis") spheres ("sph") read, based on the work of Feng and Michaelides [30, 80],

$$Nu_{vis,sph} = \frac{2-\lambda}{2} Nu_b + \frac{4\lambda}{6+\lambda} Nu_2 \qquad (0 \leq \lambda \leq 2;\ Pe \leq 1000) \tag{2.112}$$

with λ already defined in Eq. (2.103). At high viscosity ratios, the following equation applies

$$Nu_{vis,sph} = \frac{4}{\lambda+2} Nu_2 + \frac{\lambda-2}{\lambda+2} Nu_{s,sph} \qquad (2 \leq \lambda < \infty;\ Pe \leq 1000) \tag{2.113}$$

In the equations above, the Nusselt number of a bubble ($\lambda = 0$) is defined as [30]

$$Nu_b = 0.651\sqrt{Pe}\left(1.032 + \frac{0.61Re}{Re+21}\right) + \left(1.6 - \frac{0.61Re}{Re+21}\right) \tag{2.114}$$

The Nusselt number for a solid sphere ($\lambda \to \infty$) reads [30]

$$Nu_{s,sph} = 0.852Pe^{1/3}(1+0.233Re^{0.287}) + 1.24 - 0.182Re^{0.355} \tag{2.115}$$

Finally, the Nusselt number for a sphere with an intermediate viscosity ratio ($\lambda = 2$) reads [30]

$$Nu_2 = 0.64Pe^{0.43}(1+0.233Re^{0.287}) + 1.41 - 0.15Re^{0.287} \tag{2.116}$$

Note that the Peclet number is defined in this formulation based on gaseous fluid quantities and the thermal conductivity as

$$Pe_{Nu} = Pr \cdot Re \tag{2.117}$$

The respective correction for the Sherwood number is also obtained by Eqs. (2.112) and (2.113) if the Peclet number is defined based on the mass diffusion coefficient as

$$Pe_{Sh} = Sc \cdot Re \tag{2.118}$$

Next, the underlying assumption of a spherical drop in the equations above is lifted. Fully consistent with the momentum coupling approach, the correction of the Nusselt number is based on the most recent work from Richter and Nikrityuk [77]. They identified the sphericity ϕ and the cross-wise sphericity $\phi_\perp$ as the main geometric parameters which account for variations of Nusselt numbers when a sphere is distorted along its spanwise direction. Note that this spanwise direction is directly calculated by TAB model, compare Eq. (2.110). Similarly to Eq. (2.109), the correction equation reads

$$Nu = Nu_{vis,sph} \cdot \frac{1.76 + 0.55\phi Pr^{1/3}\sqrt{Re}\phi_\perp^{0.075} + 0.014 Pr^{1/3} Re^{2/3} \left(\frac{\phi}{\phi_\perp}\right)^{7.2}}{1.76 + 0.55 Pr^{1/3}\sqrt{Re} + 0.014 Pr^{1/3} Re^{2/3}} \tag{2.119}$$

The sphericity ϕ is defined as

$$\phi = \frac{4\pi r^2}{\mathrm{Srfc}_d} \tag{2.120}$$

and the cross-wise sphericity $\phi_\perp$is defined as

$$\phi_\perp = \left(\frac{r}{H}\right)^2 \tag{2.121}$$

with Srfc_d as the surface area of the deformed drop and with H as the length of half of the axis of the cross-wise area of the deformed drop. These quantities are defined as follows. Dependent on the drop distortion y, compare Eq. (2.86), the drop deforms into an oblate spheroid ($y \geq 0$) or into a prolate spheroid ($y < 0$), respectively. It is important to realize that the shape of these spheroids is well-defined from TAB model and can be obtained from volume conservation to

$$V = \mathrm{const} = \frac{4}{3}\pi r^3 = \frac{4}{3}\pi L H^2 \tag{2.122}$$

Then, the height of the spheroid (in normal flow direction) can be calculated

$$H = \sqrt{\frac{r^3}{L}} = \frac{r}{\sqrt{1 - C_b y}} \tag{2.123}$$

where the relation $L = r(1 - C_b y)$ was utilized. Then, the surface area can be computed if the drop is deformed into an oblate spheroid as follows

$$\mathrm{Srfc}_d = 2\pi H^2 \left(1 + \frac{1 - e^2}{e} \tanh^{-1} e\right) \qquad y \geq 0 \tag{2.124}$$

or, if the drop is deformed into a prolate spheroid

$$\mathrm{Srfc}_d = 2\pi H^2 \left(1 + \frac{L}{He}\sin^{-1} e\right) \qquad y < 0 \tag{2.125}$$

with the eccentricity e defined as

$$e = \sqrt{1 - \left(\frac{\min(H,L)}{\max(H,L)}\right)^2} \tag{2.126}$$

The shape correction for the Sherwood number is also performed based on Eq. (2.119) when the Prandtl number is replaced by the respective Schmidt number. These modifications of the transfer numbers alter the characteristic time scales of drop heating and evaporation, utilized in Eqs. (2.52) and (2.53) for the limit of a solid spherical drop, in the following manner. The time scale for the drop lifetime then reads

$$\frac{\tau_f}{\tau_l} = \left.\frac{\tau_f}{\tau_l}\right|_{s,sph} \cdot \frac{Sh}{Sh_{s,sph}} \tag{2.127}$$

The time scale of drop heating reads, consulting Eq. (2.43),

$$\frac{\tau_f}{\tau_c} = \left.\frac{\tau_f}{\tau_c}\right|_{s,sph} \cdot \frac{Nu}{Nu_{s,sph}} \tag{2.128}$$

Note that, contrary to the drag coefficient which implicitly includes the surface area alteration of the deforming drop, the Nusselt and Sherwood numbers represent surface-averaged values only. As a consequence, the coupling model for mass and energy, which explicitly includes the square of the mass-equivalent drop diameter as defined in Eqs. (2.52) and (2.53), is finalized by the calculation of the surface area change with respect to the mass-equivalent drop sphere. The final correction is introduced as a correction factor to the original drop diameter of the spherical drop d_p as follows

$$d^2 = d_p^2 \cdot \frac{\mathrm{Srfc}_d}{\pi d_p^2} \tag{2.129}$$

Finally, the characteristic time scales for the drop lifetime

$$\frac{\tau_f}{\tau_l} = \left.\frac{\tau_f}{\tau_l}\right|_{s,sph} \cdot \frac{Sh}{Sh_{s,sph}} \frac{\mathrm{Srfc}_d}{\pi d_p^2} \tag{2.130}$$

and heating are

$$\frac{\tau_f}{\tau_c} = \left.\frac{\tau_f}{\tau_c}\right|_{s,sph} \cdot \frac{Nu}{Nu_{s,sph}} \frac{\mathrm{Srfc}_d}{\pi d_p^2} \tag{2.131}$$

These modified characteristic time scale also enter into the scheme for the determination of the time step used for Runge-Kutta integration as defined in Eq. (2.37).

It is worth mentioning that, in the limit of rigid spherical drops, the predicted corrections from this framework on drop mass, momentum, and energy transfer due to drop distortions and internal flow dynamics exactly recover the widely-accepted and highly-accurate correlations of drag, mass, and heat transfer coefficients.

The coupled equations of mass, momentum, and energy also feed back into the TAB model. The TAB equations explicitly depend on the dynamic drop radius which depends on the drop temperature and the evaporation rate. With changing temperature, the liquid drop properties and the surface tension also change accordingly. This is being calculated dynamically from real-fluid thermodynamics and molecular mean-field two-phase interface methods. The aerodynamic forces are calculated from the coupling to high-fidelity large eddy simulations. A suitable temporal resolution of the drop dynamics is required in order to accurately capture these complex interactions between the unsteady aerodynamic forces and the drop response. This temporal resolution is determined by adding the characteristic oscillation time scale in relation to the fluid flow time to the determination of the simulation time step used for Runge-Kutta integration as defined in Eq. (2.37). This oscillations time scale reads

$$\tau_{osc} = \Delta y \frac{d\tau}{dy} = \Delta y \frac{dt}{dy} \frac{U_{ref}}{L_{ref}} \tag{2.132}$$

with $\Delta y \sim 0.05$ as a well-defined proportionality constant in order to accurately resolve the non-dimensional TAB distortion parameter y.

A Refined Model for Drop Breakup

In the original work of O'Rourke and Amsden, a theory for the determination of the drop properties after a breakup event (y $>$ 1) is presented. It is based on an energy balance of surface and kinetic energy between drops before and after breakup [67]. The energy balance before breakup E_b reads for the original drop [67]

$$E_b = 4\pi r^2 \sigma + K \frac{\pi}{5} \rho_l r^5 \left[\left(\frac{dy}{dt} \right)^2 + \omega^2 \right] \tag{2.133}$$

with $K = 10/3$ as the experimentally obtained ratio of the oscillation and distortion energy and the energy of the fundamental mode. The first term on the right-hand side represents the surface energy

and the second term denotes the kinetic energy. The energy balance E_a of drops after breakup can be obtained similarly [67]

$$E_a = 4\pi r^2 \sigma \frac{r}{r_{32}} + \frac{\pi}{6} r^5 \rho_l \left(\frac{dy}{dt}\right)^2 \tag{2.134}$$

The Sauter mean radius has entered the above equation using its fundamental definition

$$r_{32} = \frac{r_V^3}{r_d^2} \tag{2.135}$$

with r_V and r_d as the volume-equivalent and surface-equivalent drop radius, respectively. Equating both formulas leads to the following final expression for the Sauter mean radius r_{32} as proposed by O'Rourke and Amsden [67]

$$r_{32} = \frac{r}{1 + \frac{8K}{20} + \left(\frac{6K-5}{120}\right) \frac{\rho_l r^3}{\sigma} \left(\frac{dy}{dt}\right)^2} \tag{2.136}$$

The velocities of newly created drops receive a velocity v_n normal to the original drop velocity vector

$$v_n = AC_b r \frac{dy}{dt} \tag{2.137}$$

with A being a proportionality constant postulated to be $A = 1$ in the original formulation [67]. The constant C_b is listed in Table 2.4. The exact direction of the normal drop velocity vector is obtained by random sampling.

Since the pioneering work from O'Rourke and Amsden, many studies from academia and industry have shown that the drop sizes after breakup are often significantly under-predicted and that deficiencies in the prediction of the spray angle, to which the breakup model contributes, exist [42, 52, 97–99, 103]. This deficiency, along with the attempt to extend the validity of TAB model to higher Weber number regimes, has motivated further developments since, most notably the Enhanced Taylor Analogy Breakup (ETAB) model [97, 99], the Cascade Atomization Breakup (CAB) model [98], and the hybrid T-BLOB/T-TAB model [102]. These frameworks have utilized introduced proportionality constants, which depend on the drop breakup regime, to successfully match the experimental drop size distribution.

The model for drop breakup presented in this study, however, is entirely derived from a set of conservation equations for mass, momentum, and energy and does not rely, as a consequence, on introduced proportionality constants. The starting point of this model is a refined energy conservation equation of the type originally proposed by O'Rourke and Amsden, compare Eqs. (2.133)

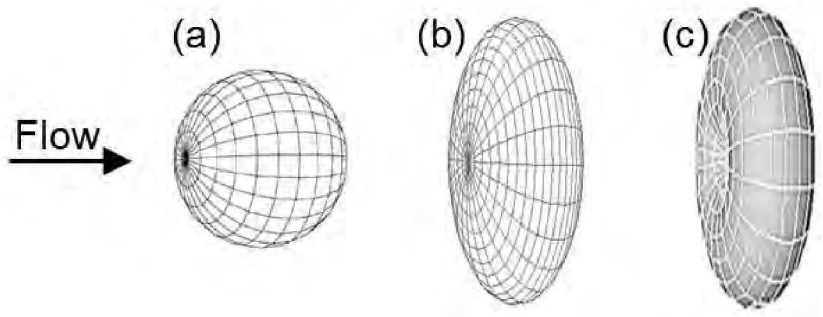

Figure 2.3. (a) The spherical shape of the drop is the underlying assumption of the original breakup energy equation, compare the first term of the right-hand-side of Eq. (2.133). (b) The well-defined oblate shape of the drop at $y = 1$. (c) The well-defined flattened torus shape of the drop at breakup $y = 1$. In TAB, breakup is assumed to occur when the oscillation of the north and south pole meet at the center [67].

and (2.134). It is important to realize that this equation is conditioned on the specific time of drop breakup and has no meaning at any other point in time.

Figure 2.3 illustrates a sketch of different levels of drop distortions which are fully consistent with the underlying TAB equations and assumptions. Figure 2.3 (a) shows the spherical shape of the drop without distortion or oscillations. It serves as the underlying assumption of the drop state at breakup in the original breakup energy equation, compare the first term on the right-hand side of Eq. (2.133). Figure 2.3 (b) illustrates the distortion of the drop into an oblate shape as predicted by TAB at the time of breakup ($y \geq 1$). This shape can be obtained by a mass conservation equation as follows

$$m = \text{const.} = \frac{4}{3}\pi\rho_l r^3 = \frac{4}{3}\pi\rho_l L \cdot H^2 \tag{2.138}$$

with L as half of the length of the minor axis (in flow direction) and with H as half of the length of the major axis of the oblate spheroid. The breakup model directly provides L as a solution to Eq. (2.86) as

$$L = r - x = r(1 - C_b y) \tag{2.139}$$

Then, the major axis of the oblate spheroid can be calculated as

$$H = \sqrt{\frac{r^3}{L}} \tag{2.140}$$

According to TAB's original criterion, the oscillation of the north and south pole of the drop meet at its center at the time of breakup [67]. As a consequence, the shape of the drop has then further deformed into a flattened torus with a cross area of an ellipse as conceptually shown in Fig. 2.3 (c). The surface area of this shape reads

$$\mathrm{Srfc}_b = \pi \cdot H \cdot \left[\pi(\frac{H}{2} + b_m) \cdot \left(1 + 3\frac{\lambda_b^2}{10 + \sqrt{4 - 3\lambda_b^2}} \right) \right] \tag{2.141}$$

with $\lambda_b = (H/2 - b_m)/(H/2 + b_m)$ according to the approximation formula of the circumference of an ellipse proposed by Ramanujan [70] and with H as the major axis of the underlying oblate spheroid at $y \geq 1$, calculated according to Eq. (2.140). The minor axis of the ellipse has again been obtained by mass conservation to

$$b_m = \frac{8}{3}\frac{r^3}{\pi H^2} \tag{2.142}$$

This surface area can be related to a corresponding radius $r^\star$ of a sphere with the same area and to the physical radius r of the mass-equivalent drop

$$r^\star = r\sqrt{\frac{\mathrm{Srfc}_b}{4\pi r^2}} = r\chi_s \tag{2.143}$$

with χ_s as the square root of the ratio of the respective surface areas. This well-defined shape also allows the calculation of the velocity magnitude of newly created drops from breakup normal to the flow vector of the original drop. The velocity of the poles of the original drop, dy/dt, conditioned on the time of breakup, is directly obtained from Eq. (2.93). Mass conservation then allows the calculation of the respective normal velocity magnitude.

$$\frac{dm}{dt} = 0 = \frac{d(\rho_l V)}{dt} = \frac{4}{3}\pi\rho_l \frac{d(H^2 r(1 - C_b y))}{dt} \tag{2.144}$$

where Eq. (2.139) is utilized and the time derivative of the liquid density is assumed to be negligible in comparison to the other terms ($\rho_l \approx$ const). This leads to

$$r(1 - C_b y)\frac{d(H^2)}{dt} + H^2 r\frac{d(1 - C_b y)}{dt} = 0 \tag{2.145}$$

It is important to note that r is constant in this equation since it reflects the radius of the mass-equivalent sphere, compare Eq. (2.139). This results further in

$$2Hr(1 - C_b y)\frac{dH}{dt} - C_b r H^2 \frac{dy}{dt} = 0 \tag{2.146}$$

which is finally solved for the velocity magnitude normal to the flow velocity

$$\frac{dH}{dt} = \frac{C_b H}{2(1-C_b y)} \frac{dy}{dt} = \frac{r}{2} \frac{C_b}{\sqrt{(1-C_b y)}} \frac{dy}{dt} \tag{2.147}$$

From these equations, the proportionality constant in the original model, compare Eq. (2.137), is then being calculated to

$$A = \frac{1}{2(1-C_b y)^{1.5}} \tag{2.148}$$

It is noteworthy that for the special case of $C_b = 0.5$ and $y = 1$, the constant equates to $A = \sqrt{2}$, similar to the originally postulated value of unity.

Now, the energy balance for the drop mass before breakup, conditioned on the time of breakup, is formulated as

$$E_b^\star = 4\pi r^2 \chi_s^2 \sigma + K \frac{\pi}{5} \rho_l r^5 \left[\left(\frac{dy}{dt} \right)^2 + \left(\frac{C_K \sigma}{\rho_l r^3} - \frac{C_d^2 \mu_l^2}{4\rho_l^2 r^4} \right) y^2 \right] \tag{2.149}$$

Note that χ_s is defined in Eq. (2.143) and that Eq. (2.149) includes the drop damping in the calculation of the drop oscillation frequency, neglected in the original formulation. It is also worth mentioning that the distortion parameter is not set to $y = 1$ since this value is directly linked to the critical Weber number below which breakup does not occur. However, under certain conditions, such as elevated system pressures or non-Newtonian liquids, deviations from the classical value $We_c = 12$ may occur. To obtain the energy balance for the drop mass after breakup, conditioned on the time of breakup, the kinetic energy of the drop mass in normal flow direction must be calculated.

$$E_{kin} = \frac{1}{2} m v^2 = \frac{1}{2} \frac{4}{3} \pi \rho_l r^3 \left(\frac{dH}{dt} \right)^2 \tag{2.150}$$

Note that the kinetic energy is independent of the drop shape. Consulting Eqs. (2.147) and (2.148) leads to

$$E_{kin} = \frac{2}{3} \pi \rho_l r^5 C_b^2 A^2 \left(\frac{dy}{dt} \right)^2 \tag{2.151}$$

Then, the energy balance of drops after breakup is defined as

$$E_a^\star = 4\pi r^2 \chi_s^2 \frac{r}{r_{32}} \sigma + \frac{2}{3} \pi \rho_l r^5 C_b^2 A^2 \left(\frac{dy}{dt} \right)^2 \tag{2.152}$$

Equating the energy distribution before (Eq. (2.149)) and after breakup (Eq. (2.152)) and solving for the Sauter mean radius r_{32} finally leads to

$$r_{32} = \frac{r}{1 + \frac{K}{20\chi_s^2}\left(C_K - \frac{C_d^2 \mu_l^2}{4\sigma\rho_l r}\right) y^2 + \left(\frac{K}{20} - \frac{A^2 C_b^2}{6}\right) \frac{\rho_l r^3}{\chi_s^2 \sigma} \left(\frac{dy}{dt}\right)^2} \tag{2.153}$$

with χ_s defined in Eq. (2.143), with σ defined in Eq. (2.81), and with A defined in Eq. (2.148). This equation includes, fully consistent with the underlying assumptions of TAB, a more realistic approximation of the surface energy, a more precisely calculated kinetic energy of the newly created drops, and it considers the true oscillation energy of the drop as calculated by Eq. (2.86) at the time of breakup. Note that, besides these advancements, the TAB modeling constants remain present in all equations above. As a consequence, alterations of these constants are carried through the framework to avoid inconsistencies and violations of conservations laws.

At the time of breakup, new drops are created with an initial location randomly chosen within the volume of the original distorted drop. The velocity $\vec{v}_d$ of each drop i is calculated as follows

$$\vec{v}_{d,i} = \vec{v}_o + \text{rand}(\vec{e}_\perp) \frac{dH}{dt} \tag{2.154}$$

with $\vec{v}_o$ as the velocity vector of the original drop, with $\text{rand}(\vec{e}_\perp)$ as a random unit vector normal to $\vec{v}_o$, and with dH/dt defined in Eq. (2.147). It is important to realize that Eq. (2.154), also applied in previous frameworks in a similar form, generally violates the conservation of momentum. As demonstrated above, the second term on the right-hand-side of Eq. (2.154) originates from the kinetic energy stored in the drop oscillation of the original drop before breakup. This oscillation has not contributed to the original drop momentum which solely resulted from its translational motion. After breakup, however, this oscillation is transformed into a translational motion of the new drops which carry momentum as a consequence. In order to conserve momentum after breakup, the following equations are solved

$$m_o \vec{v}_o = \sum_{i=1}^{N} m_i \vec{v}_{d,i} = \sum_{i=1}^{N} m_i \left[\vec{v}_o + \text{rand}(\vec{e}_\perp) \frac{dH}{dt}\right] = m_o \vec{v}_o + \sum_{i=1}^{N} m_i \cdot \text{rand}(\vec{e}_\perp) \frac{dH}{dt} \tag{2.155}$$

with N as the number of newly created drops and with $m_o = \sum m_i$ as the mass of the original drop. This analysis immediately leads to the condition for momentum conservation

$$\sum_{i=1}^{N} m_i \cdot \text{rand}(\vec{e}_\perp) \frac{dH}{dt} = 0 \tag{2.156}$$

This restriction is enforced in the following manner. The radii of newly created drops are determined by sampling based on the Sauter mean radius as defined in Eq. (2.153). This sampling of

drop sizes proceeds until the total mass of all new drops has exceeded the mass of the original drop m_o. This determines the number of newly created drops N. Mass conservation between the new drops and the original drop is enforced by a subsequent scaling of all drop radii r_i as follows

$$r_i = r_{i,s} \left(\frac{m_o}{\sum m_{i,s}} \right)^{1/3} \tag{2.157}$$

with $r_{i,s}$ as the drop radius from sampling and with $m_{i,s}$ as the corresponding drop mass. The velocities of all randomly chosen drops is prescribed by Eq. (2.154). The normal velocity vector of the drop with the largest mass $\vec{v}_m$, however, is calculated afterwards for momentum conservation to

$$\vec{v}_{m,\perp} = -\frac{1}{m_m} \sum_{i=1;i\neq j}^{N} m_i (\vec{v}_{d,i} - \vec{v}_o) \tag{2.158}$$

with m_m as the mass of the drop with the largest mass of all newly created drops. Note that the mass-based selection criterion for this drop guarantees its meaningful velocity determined by Eq. (2.158). It is important to realize that, without the framework described above, momentum conservation is violated in a non-negligible manner. The number of newly created drops, while depending on the computed ratio r/r_{32}, is generally far insufficient to guarantee an approximate solution of Eq. (2.156) using statistical sampling. Furthermore, respective drop masses and drop velocities are both chosen randomly and independently of each other. As a consequence, a large number of samples would be required for statistical convergence which is, conceptually, not realizable by the physical process of drop breakup within breakup regimes modeled by TAB. Equation (2.158), while enforcing momentum conservation, violates energy conservation since it computes a velocity magnitude which differs from the magnitude of the other drops, inconsistent with the underlying assumptions of Eq. (2.153). However, we note from Eq. (2.158) that momentum remains conserved if all drop normal velocity magnitudes would be subject to the same scaling operation. This is utilized to obtain the proper velocity scaling for all drops

$$\vec{v}_{i,\perp} = c_v \cdot (\vec{v}_{d,i} - \vec{v}_o) \tag{2.159}$$

with c_v defined as follows to enforce energy conservation consistent with the assumptions of Eqs. (2.150) and (2.153)

$$\frac{m}{2} \left(\frac{dH}{dt} \right)^2 = c_v^2 \left[\frac{m_m}{2} \vec{v}_{m,\perp}^2 + \frac{m - m_m}{2} \left(\frac{dH}{dt} \right)^2 \right] \tag{2.160}$$

which results in

$$c_v = \left(1 + \frac{m_m}{m} \left[\left(\frac{v_{m,\perp}}{\vec{v}_d - \vec{v}_o} \right)^2 - 1 \right] \right)^{-1/2} \tag{2.161}$$

This page intentionally left blank.

Chapter 3

Results - Sommerfeld

Following previous research by Oefelein [62, 65], the models described in the preceding chapters are tested in a model gas turbine configuration to analyze the framework at realistic conditions. Sommerfeld et al. [90–92] provides detailed measurements of swirling particle-laden flow in a model combustion chamber that consists of a sudden pipe expansion with a centered (primary) and annular (secondary) jet discharging into a cylindrical test section. Experimental measurements were acquired using a one-component phase-Doppler-anemometer *(PDA)* to obtain mean and rms gas-phase and particle-phase statistics of velocity and particle size. This experiment provides a good benchmark for validation of LES with well-defined boundary conditions.

A schematic of the experimental apparatus and matching computational domain is shown in Fig. 3.1. The rig is cylindrical and consists of an injector section, main chamber, and plenum chamber. The coaxial injector houses a centered particle-laden primary jet surrounded by a swirling annular secondary jet. Flow is injected into the main chamber from the top. Upon entering the chamber the flow undergoes a sudden expansion followed by a series of complex fluid dynamic interactions. The flow then undergoes a second expansion at the exit of the main chamber into a plenum chamber. The region of interest showing the eight axial stations where cross-sectional *PDA* measurements were made is shown in Fig. 3.2. Gas-phase and particle-phase mean and rms velocity components are given with simultaneous measurements of the particle size and mass flux distributions. Data were obtained with two different particle mass loadings in the primary jet, for three different particle size classes.

The relevant flow conditions and particle properties are summarized in Table 3.1. Particles are injected into the primary jet in equilibrium with the gas phase velocity according to the distribution given by Fig. 3.3. This distribution produces a mean number diameter of 45 μm and particle sizes over the range $20 \leq d_p \leq 80$ μm. The walls inside the injector ducts are assumed to be adiabatic. Walls in the main chamber are assumed to be 300 K. The geometry is characterized in dimensionless units using the radius R of the outer wall of the secondary jet as the reference length scale (i.e., $\delta_{\text{ref}} = R = 32$ mm). The main chamber is approximately 30 dimensionless units long and extends a radial distance of approximately 3 dimensionless units. The injector section (not shown) extends 8 units upstream from the main chamber face plate. The plenum chamber begins approximately 30 units downstream of the main chamber, ends at 50 units, and extends a radial distance of 9 units. The primary jet has a radius of $r/R = 0.5$. Flow from the primary jet evolves to a fully-developed turbulent state prior to injection and enters the main chamber axially. The secondary jet extends over a radial interval of $0.59 \leq r/R \leq 1$, is fully-developed, and is injected

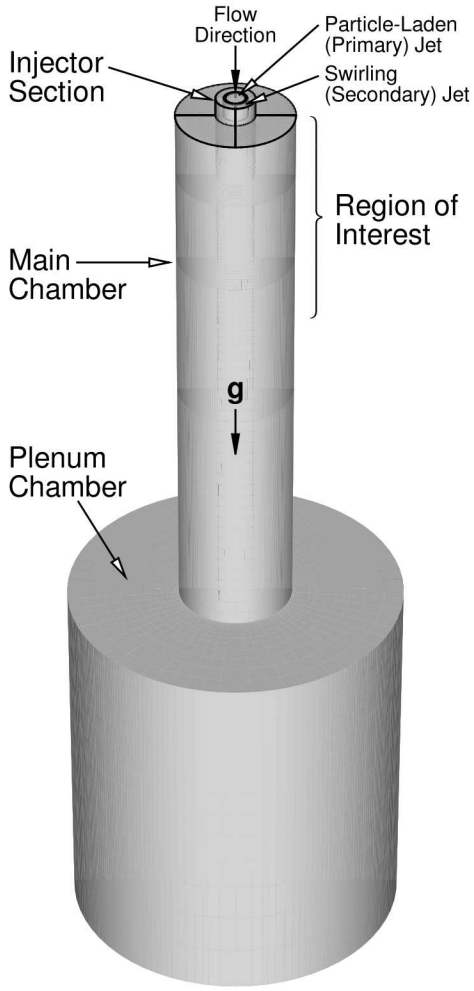

Figure 3.1. Schematic of the experimental apparatus employed by Sommerfeld *et al*. [90–92].

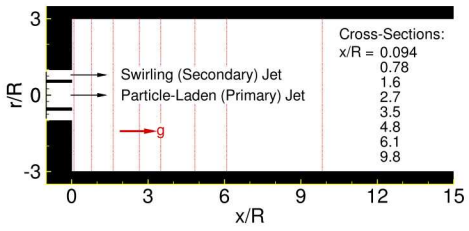

Figure 3.2. Region of interest showing the location where cross-sectional *PDA* measurements were made.

Table 3.1. Flow conditions and particle properties used in the Sommerfeld experiments.

	Case 1	**Case 2**
Gas Phase (Air):		
Flow rate in primary jet, g/s	9.9	6.0
Flow rate in secondary jet, g/s	38.3	44.6
Inlet Reynolds number[a]	26200	27250
Swirl number	0.47	0.49
Temperature, K	300	
Particle Phase:		
Loading ratio in primary jet	0.034	0.17[b]
Flow rate, g/s	0.34	1.0
Mean diameter, μm	45.5	
Density ratio, ρ_p/ρ_f	2152	

[a]Based on total volume flow rate. [b]5 $\times$ Case 1.

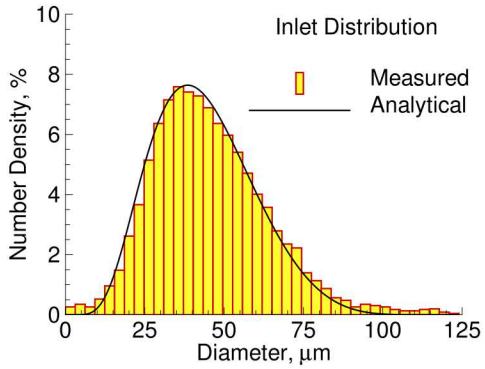

Figure 3.3. Particle size distribution in the axial (primary) jet.

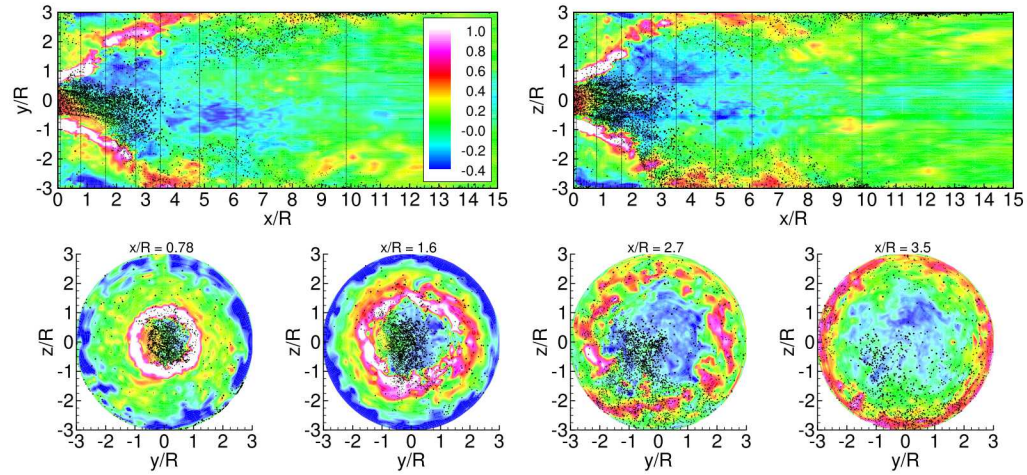

Figure 3.4. Instantaneous particle distribution superimposed on the corresponding turbulent velocity field. Case 2, cross-sections correlate with the axial locations shown in Fig. 3.2.

into the main chamber with a swirling azimuthal velocity component. A reference velocity of $U_{\text{ref}} = 12.9\ m/s$ (based on the bulk flow rate in the primary jet) was used in all cases. The flow rate in the secondary annular jet was adjusted to give a maximum velocity of approximately 18 m/s. The maximum tangential velocity for both cases was approximately 13 m/s.

A representative LES solution corresponding to Case 2 in Table 3.1 is shown in Figure 3.4. This figure shows the instantaneous particle distribution in the region of interest superimposed on the corresponding turbulent velocity field in the y-x, z-x, and z-y planes at axial locations of $x/R = 0.78,\ 1.6,\ 2.7$ and 3.5, respectively. The four radial cross-sections correspond to the axial stations where *PDA* measurements were made. This figure clearly highlights the asymmetric precessing nature of the flow. At any instant in time there are approximately 2.5-million particles being tracked in the region of interest. Tracking this number of particles is significant since it verifies the feasibility of employing large numbers of physical particles and eliminates the need to implement classical parcel approximations for cases such as this.

To test the current model framework, we analyze the injection of liquid n-decane drops at a temperature of $T_d = 363$ K into compressed air at p=10 bar and $T_{air} = 475$ K. These boundary conditions define the envelope of possible vapor-liquid interface conditions and, as a consequence, the envelope of resulting interface transfer processes as highlighted in what follows. Figure 3.5 (left) presents the real-fluid vapor and liquid equilibrium phase conditions of a n-decane–air mixture which are physically realizable at p=10 bar. These calculations are performed as defined in Eq. (2.77). Figure 3.5 (left) shows the mole fraction of fuel as a function of the interface temperature. At low temperatures, the saturated fuel mole fraction in the vapor phase remains low, which indicates a low evaporation rate, to be quantified later, at these conditions. With increasing temperature, however, the mole fraction and the corresponding evaporation rate is expected to increase significantly. Figure 3.5 (right) shows corresponding mixture densities of vapor and liquid

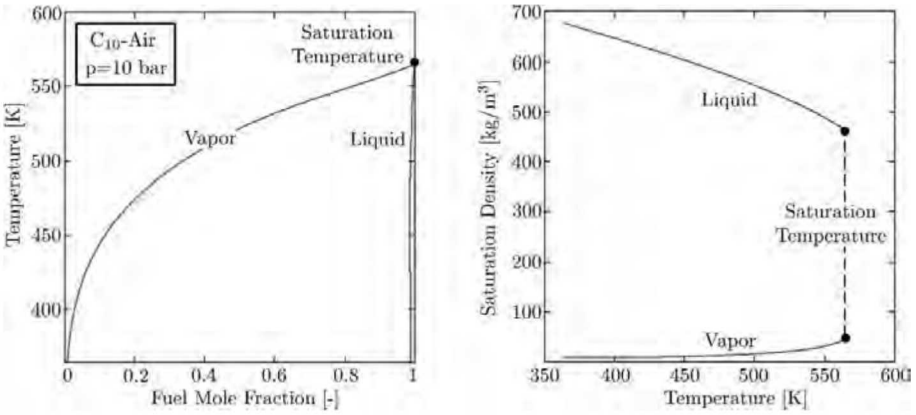

Figure 3.5. (Left) Envelope of vapor and liquid equilibrium phase compositions of a C_{10}-Air mixture at p=10 bar and various temperatures. (Right) Corresponding vapor and liquid saturation densities.

phases up to temperatures of T ≈ 565 K, which represents the saturation temperature of the multi-component mixture at p=10 bar. A distinct two-phase interface cannot exist at higher temperatures. Such calculations quantify the vapor and liquid phase compositions and facilitate corresponding computations of the Spalding transfer number B_M, which is defined in Eq. (2.44).

Calculations of the transfer number are presented in Fig. 3.6 as a function of the interface temperature for a n-decane–air mixture. It shows an exponential increase with temperature. The presented distribution has its highest curvature at T≈525 K which highlights the significance of elevated temperatures to evaporation rates. Figure 3.7 shows mean-field simulations of molecular two-phase interface structures at an interface temperature of T=450 K and T=500 K, respectively. Such simulations, obtained from Eq. (2.82), quantify the molar density distributions of decane, nitrogen, oxygen, and argon in the direction normal to the vapor-liquid interface. For illustration, the molar densities of nitrogen and oxygen are multiplied by a factor of 10. The molar density of argon is multiplied by a factor of 100. Note that the interfacial region has a thickness of only about 1–2 nm. As a consequence, each species spatial density gradient significantly contributes to the distribution of the Free Helmholtz energy within the interfacial region, fully accounted for in Gradient Theory. It is also important to realize that the respective mixture composition at either side of the interface simulation exactly matches the vapor and liquid phase compositions of prior real-fluid two-phase equilibrium calculations, shown in Fig. 3.5 (left).

Gradient Theory simulations facilitate fundamentally-consistent surface tension calculations in multicomponent mixtures over a wide range of conditions as defined in Eq. (2.81). As demonstrated later, the fidelity of surface tension calculations significantly contributes to the accurate predictions of drop dynamics and drop breakup processes in particular. Figure 3.8 presents real-fluid calculations of liquid viscosities at p=10 bar and various temperatures, computed from Eq. (2.72) and utilized for TAB drop oscillation simulations as defined in Eq. (2.86). Such calculations are based on the composition of the liquid phase only and not the state of the two-phase interface.

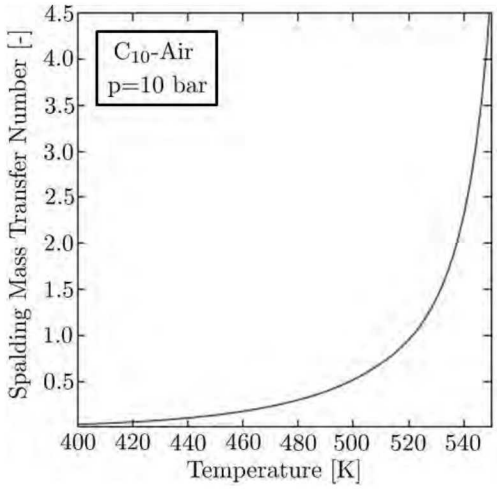

Figure 3.6. Real-fluid calculations of the Spalding transfer number B_M, defined in Eq. (2.44), for a C_{10}-Air mixture at p=10 bar and various temperatures.

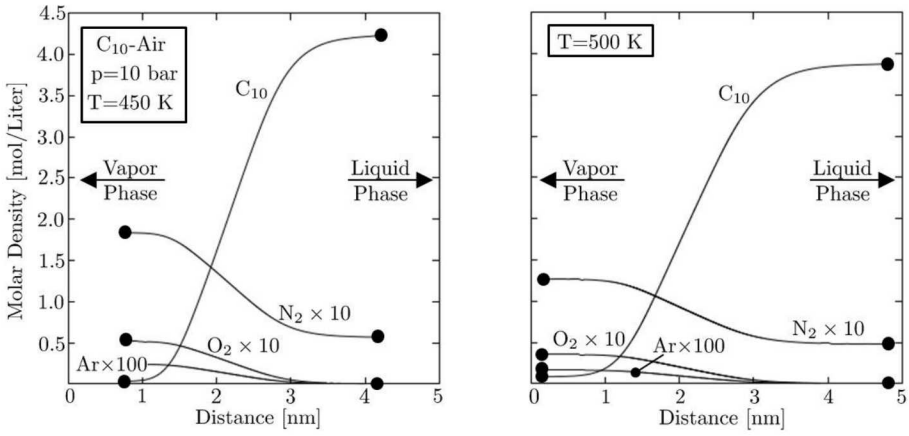

Figure 3.7. Mean-field simulations of molecular two-phase interface structures for a C_{10}-Air mixture at p=10 bar and at T=450 K (left) and at T=500 K (right), respectively. These simulations facilitate surface tension calculations in multicomponent mixtures over a wide range of conditions as defined in Eq. (2.81).

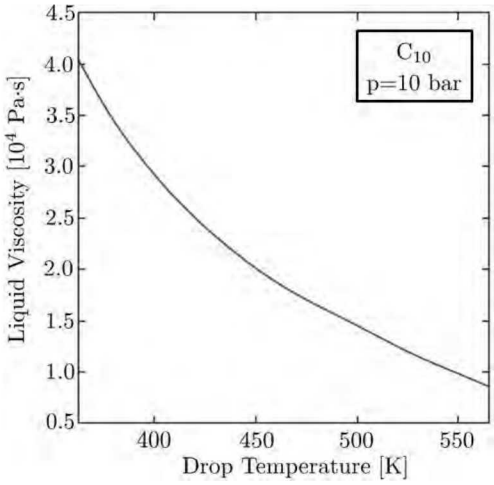

Figure 3.8. Real-fluid simulations of liquid viscosities for decane at p=10 bar and various drop temperatures.

Having established the capability of predicting both the flow and thermodynamic states of the injected drops, their location inside the widely-accepted drop distortion and breakup regime map according to Hsiang and Faeth [38] is presented in Fig. 3.9. It demonstrates that drops experience virtually all Weber numbers below We ≈ 70. As a consequence, drop dynamics are dictated by sole shape deformations (We$<$2), harmonic oscillations (We$<$12), and multimode and bag breakup processes (We$<$100). Drops experience Ohnesorge numbers in the narrow range of 0.01$<$Oh$<$0.05. Besides affecting drop oscillations (highlighted region), Ohnesorge numbers do not significantly influence the identified drop dynamics. Hence, in what follow, the analysis focuses on corresponding effects of Weber numbers while the Ohnesorge number is largely neglected.

It is important to realize that the utilized TAB breakup model is valid under all conditions of the resulting envelope of drop states. The upper range of Weber numbers under which the TAB model remains applicable is also highlighted in Fig. 3.9. Building on this analysis, simulations of drop dynamics are performed using Eqs. (2.86) and (2.93), respectively. Figure 3.10 presents drop distortions, defined in Eq. (2.85), as a function of the local drop Weber number. A drop distortion of $y = 0$ resembles the reference shape of a perfectly spherical drop. Positive and negative drop distortions characterize drops which have been deformed into an oblate spheroid or into a prolate spheroid, respectively. Hence, negative drop distortions only occur during harmonic drop oscillations. The performed analysis demonstrates that, consistent with Fig. 3.9, no drop oscillations are predicted by TAB model above the critical Weber number We_c. At higher than critical Weber numbers, Fig. 3.10 does show some drops which closely resemble the reference spherical shape (y$<$0.2). As being shown in Fig. 3.11, however, drops in this deformation state generally exhibit the largest drop distortion velocities and are, therefore, on the pathway to deform further and to eventually break up. Figure 3.11 also illustrates that drop distortion velocities diminish toward the minimal drop distortion y ≈ -0.4 observed under the conditions here. This negative distortion represents the maximal amplitude of a prolate shape deformation process. At this point in time, the

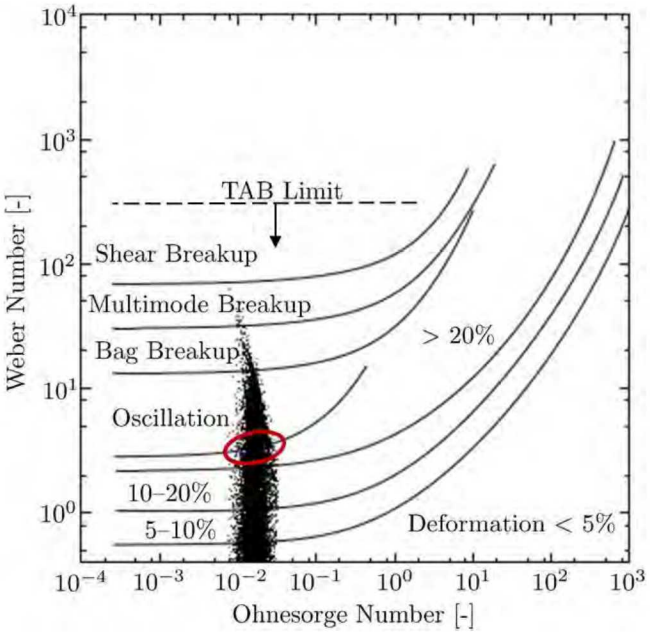

Figure 3.9. Classification of the flow and thermodynamic states of injected drops in the drop distortion and breakup regime map according to Hsiang and Faeth [38]. Besides affecting drop oscillations (highlighted region), Ohnesorge numbers do not significantly influence the identified drop dynamics. The upper range of Weber numbers under which TAB model is applicable is also highlighted.

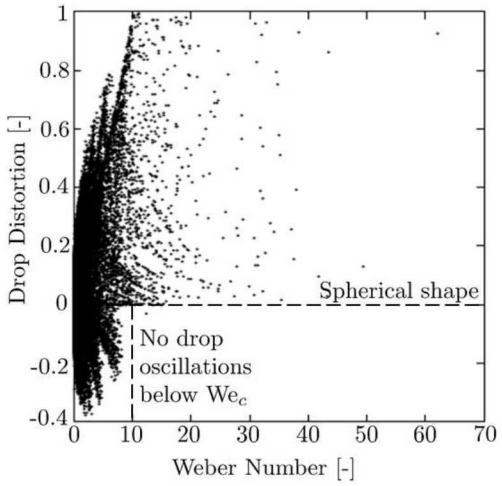

Figure 3.10. Drop distortions as a function of their local Weber numbers. Consistent with Fig. 3.9, no drop oscillations are predicted by TAB model above the critical Weber number We$_c$.

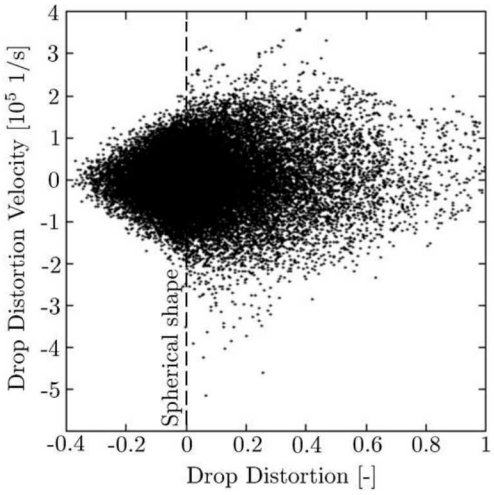

Figure 3.11. Drop distortion velocities as a function of their deformation.

energy of drop oscillations has been transferred to the energy of deformation. Note that the same trend is observed for positive deformations. The difference is, however, that the deformation can exceed the critical value for breakup before the system's natural amplitude can be reached.

Figure 3.12 presents drop Weber numbers as a function of the respective drop diameter. For large Weber numbers, a quasi-linear relation to the drop diameter is observed. It is also recognized that at drop diameters below $D \approx 13\,\mu$m, no Weber numbers higher than the critical value of We_c=12 exist. Hence, this drop diameter is unconditionally stable for drop breakup processes. This drop size along with the iso-line of the critical Weber number separate conditions of combined breakup and evaporation phenomena from conditions of drop evaporation under deformations and oscillations. The effect of the slip velocity on drop Weber numbers and drop Reynolds numbers is shown in Fig. 3.13. The local slip velocity is defined in Eq. (2.101). Both parameters show a very similar dependence on the slip velocity which is noteworthy since the Weber number depends, in contrast to the Reynolds number, on the square of this velocity magnitude. Based on this analysis, Fig. 3.14 shows the direct relation between the drop Weber number and drop Reynolds number and it reveals a strong positive correlation between both parameters. In addition to the result already obtained from Fig. 3.13, this demonstrates that both parameters mainly (and similarly) depend on the slip velocity. As a consequence, the analysis of what follows focuses on dependencies on drop Reynolds numbers which, in addition to their direct effect on gas-liquid interface processes, also implicitly includes the main physical complexity associated with Weber number effects. This analysis establishes that the drop Reynolds number is the leading order parameter of all quantities of interest here.

Figure 3.15 presents drop drag coefficient corrections relative to the solid sphere reference due to internal flow dynamics. These form in viscous spheres and are absent in solid spheres. This drag correction is calculated from Eq. (2.105) as a function of the drop Reynolds number. This correction factor depends, besides on the drop Reynolds number, also on the viscosity ratio

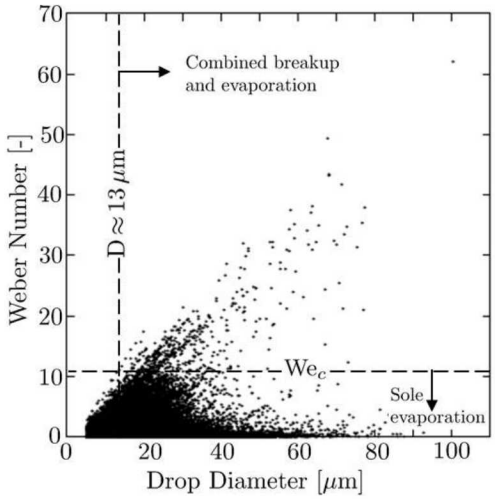

Figure 3.12. Drop Weber numbers as a function of drop diameters. The unconditionally stable drop size of $D \approx 13\mu$m and the critical Weber number We_c establish the range of conditions of combined breakup and evaporation and drop evaporation under deformations and oscillations, respectively.

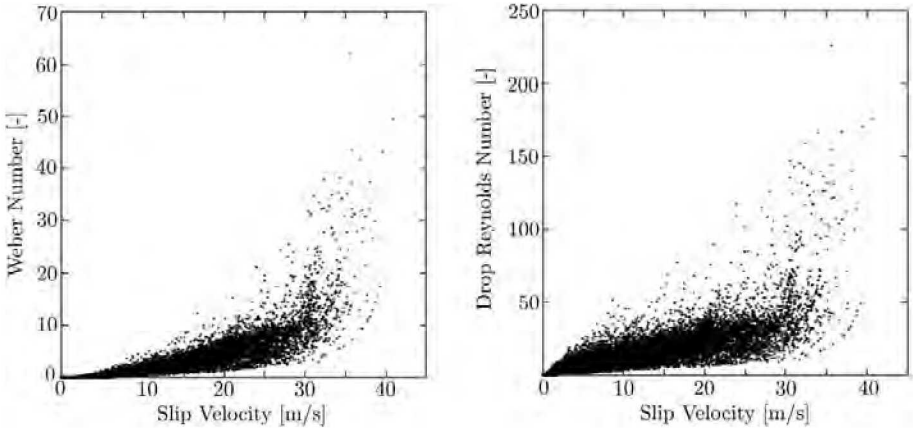

Figure 3.13. Weber number (left) and drop Reynolds number (right) as a function of the local slip velocity, defined in Eq. (2.101).

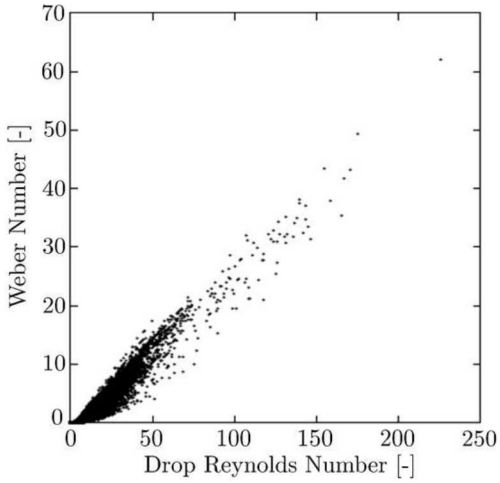

Figure 3.14. Weber number as a function of the drop Reynolds number. As suggested by Fig. 3.13, a strong correlation exists between both parameters.

λ, defined in Eq. (2.103), between liquid n-decane and air. This viscosity ratio varies, under the conditions here, between values of $7<\lambda<16$. However, as shown in Fig. 3.15, at small drop Reynolds numbers, the effect of varying viscosity ratios on the drag correction diminishes. It is important to note, however, that a noticeable difference in drag coefficient correction persists ($\sim$ 0.955) even in the limit of small drop Reynolds numbers. This is consistent with observations that solid spheres ($\lambda \to \infty$) exhibit generally higher drag coefficients than bubbles ($\lambda = 0$) regardless of the Reynolds number. Hence, the correction due to finite drop viscosity consistently lowers the drag coefficient in relation to the solid sphere reference.

Figure 3.16 shows corresponding finite drop viscosity corrections of Sherwood numbers and Nusselt numbers in relation to the solid sphere reference as a function of drop Reynolds number. These corrections have been calculated from Eq. (2.113) in which the Peclet number is defined with the Schmidt number of n-decane or with the Prandtl number, compare Eqs. (2.118) and (2.117), respectively. Similarly to the respective drag coefficient correction, shown in Fig. 3.15, differences in Sherwood and Nusselt numbers diminish at low drop Reynolds numbers. In contrast to the physical complexity observed in Fig. 3.15, both Sherwood and Nusselt numbers approach the solid sphere reference values at low drop Reynolds numbers regardless of the viscosity ratio. The corrections for both parameters exhibit a similar shape.

Figure 3.17 shows the direct relation between the finite drop viscosity corrections in Nusselt and Sherwood numbers. As suggested from Fig. 3.16, a strong correlation exists in which the Sherwood number correction is generally larger than the respective correction in Nusselt number. This is consistent with the fact that the Schmidt number of the higher hydrocarbon fuel n-decane is generally larger than the Prandtl number of the corresponding mixture. Corresponding Sherwood-Peclet numbers, compare Eq. (2.118), are also consistently larger than Nusselt-Peclet numbers as a consequence, compare Eq. (2.117), which explains the trends observed in Fig. 3.17. In the fol-

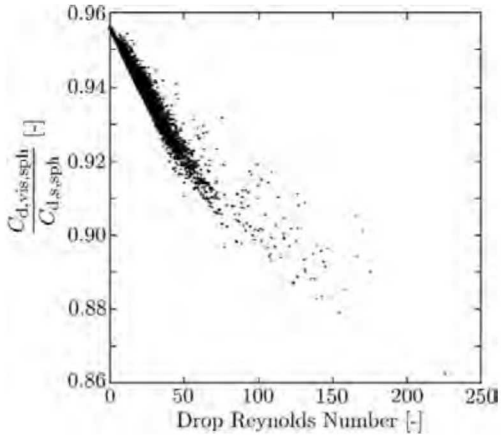

Figure 3.15. Finite drop viscosity drag correction to the solid sphere reference, calculated from Eq. (2.105), as a function of the drop Reynolds number.

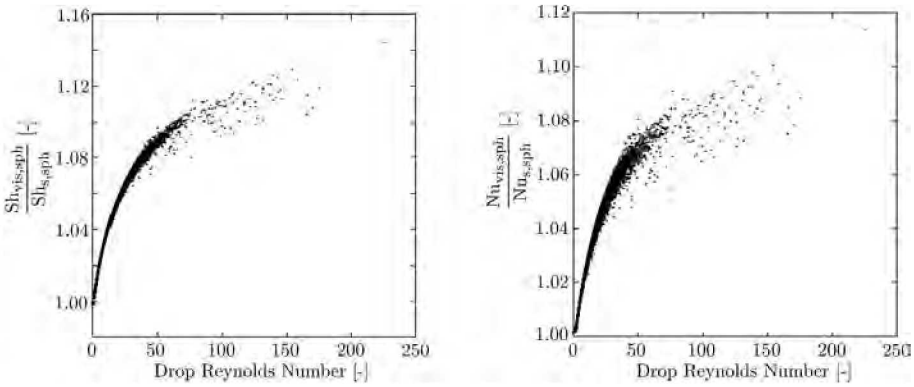

Figure 3.16. Finite drop viscosity corrections of Sherwood number (left) and Nusselt number (right) to the solid sphere reference, calculated from Eqs. (2.113), (2.117), and (2.118), as a function of the drop Reynolds number.

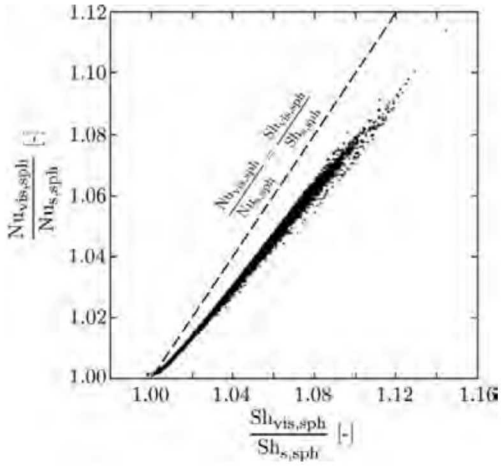

Figure 3.17. Relation between the finite drop viscosity corrections in Nusselt and Sherwood number as shown in Fig. 3.16.

lowing, effects of drop distortions are analyzed without, at first, consideration of the previously investigated finite drop viscosity effects. Figure 3.18 presents the ratio of drag coefficients, calculated by Eq. (2.108) to include the physical complexity of shape distortions, to the solid sphere reference as a function of the drop Reynolds number. It is observed that higher Reynolds numbers generally lead to larger drag coefficient corrections. It is again stressed that a strong positive correlation exists between the Reynolds number and the Weber number which was established from Figs. 3.13 and 3.14. Hence, higher Reynolds numbers also correlate with higher Weber numbers and, as a consequence, generally larger degrees of drop deformations as shown in Fig. 3.10. Drag coefficient corrections below unity resemble the conceptual view of a drop which has deformed into a prolate spheroid in flow direction. As discussed above, this physical complexity only occurs during drop oscillations which are generally present only at low Weber numbers (below the critical Weber number) which, correspondingly, result in only moderate drop deformations, compare Fig. 3.10. Such deformations can then also only be present at low Reynolds numbers ($Re < 50$), established in Fig. 3.13.

It is important to realize that drag coefficient corrections generally increase, at constant drop distortion, with increasing Reynolds numbers. Since it was established that the range of physical realizable Reynolds numbers during drop oscillations is limited, their effect on the corresponding drag coefficient is also limited as a consequence. This explains, in combination with the moderate distortion amplitude in this regime ($y > -0.4$), the trends observed in Fig. 3.18 which show much more pronounced corrections for positive drop distortions at high drop Reynolds numbers. The net effect on the drag coefficient due to finite drop viscosity and deformation is calculated from Eq. (2.109) and shown in Fig. 3.19 as a function of drop distortion. Note that the observed scatter in the plot is related to variations in drop Reynolds number, Weber number, and viscosity ratio at constant drop distortion. For illustration, the classic dynamic drag model proposed by Liu *et al.* [51], often applied in industry and academia [51, 83, 89, 102], is also shown for comparison. It must be noted that the classic model does not apply at negative drop distortions and it therefore

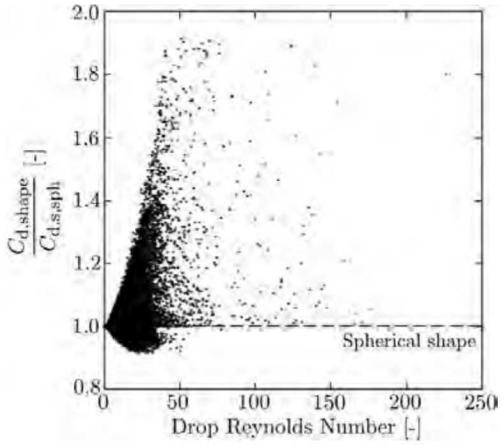

Figure 3.18. Drop drag coefficient correction to the solid sphere reference due to shape distortion, calculated from Eq. (2.108), as a function of drop Reynolds number.

neglects the presence of prolate spheroid deformations. The dynamic drag model also postulates the validity of linear interpolations between drag coefficients of reference shapes. This assumption is not necessarily supported by the results of this framework as presented in Fig. 3.19. Finally, the dynamic drag model assumes that the drag coefficient at the critical drop distortion $y = 1$ can be approximated by the drag coefficient of a sharp-edged disc. However, this assumption appears to significantly over-predict the corresponding drag coefficient in comparison to the results of this framework which may be more fundamentally-consistent with the underlying assumptions of drop deformations as quantified by TAB model.

Figure 3.20 shows drop distortion corrections, without consideration of finite drop viscosity effects, of drop evaporation and heating rates to the solid sphere reference as a function of the drop Reynolds number. The calculations are facilitated by Eqs. (2.130) and (2.131), respectively. The analysis shows similar trends as already observed for drag coefficient corrections, shown in Fig. 3.18. It is recognized, however, that corresponding mass and energy transfer rates are also enhanced, in contrast to the corresponding drag law, at negative drop distortions for prolate spheroids. In general, both transfer rates shown in Fig. 3.20 exhibit distinctive similarities. Figure 3.21 investigates the relation between drop distortion corrections in evaporation rates and heating rates. The analysis reveals, similar to effects of finite drop viscosity, a strong correlation between both transfer rates. This is partly explained due to the significant effect of the surface area increase over the spherical reference shape. This increase affects both transfer rates in equal measure. The remaining effect results from differences in Sherwood and Nusselt numbers due to shape distortions as calculated by Eq. (2.119) with adequate definitions of the Peclet number as discussed above. Due to the larger Sherwood number correction, as discussed in the context of Fig. 3.17, the corresponding correction to the evaporation rate is slightly higher than the respective correction to drop heating. Then, and in analogy to Fig. 3.19, the effective correction to the evaporation rate in relation to the solid sphere reference solution is calculated from Eq. (2.130) and is shown in Fig. 3.22. Note that the respective correction to drop heating rates closely resembles this solution and is therefore

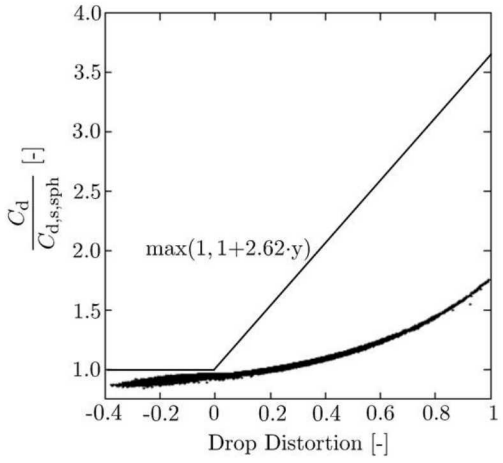

Figure 3.19. Comparison of drag corrections, calculated from Eq. (2.109), and the classic dynamic drag model proposed by Liu *et al.* [51] as a function of drop distortion.

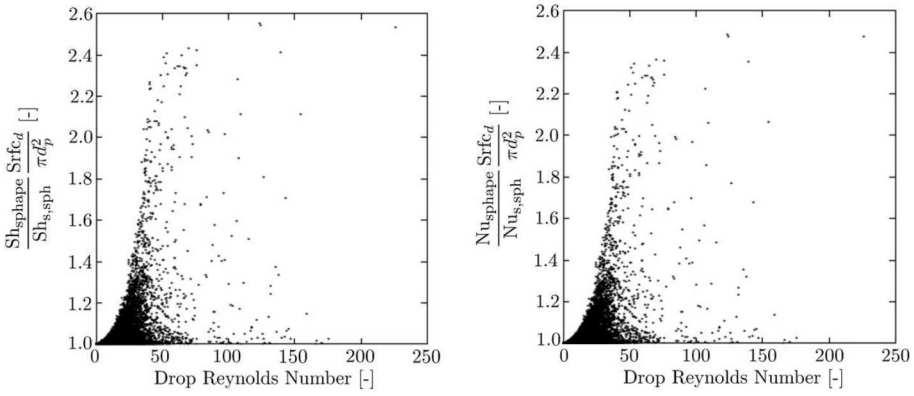

Figure 3.20. Drop distortion corrections of evaporation rates (left) and heating rates (right), calculated from Eqs. (2.130) and (2.130), to the solid sphere reference as a function of drop Reynolds number.

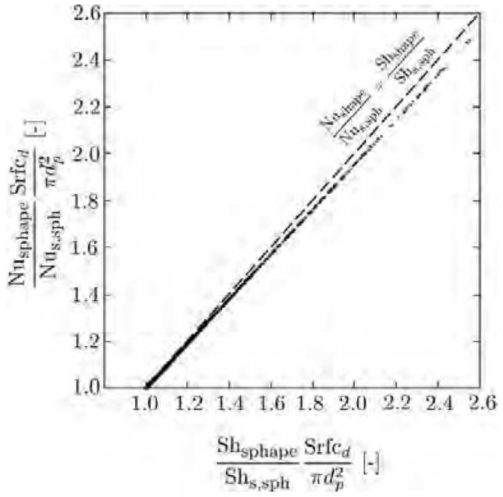

Figure 3.21. Relation between the drop distortion corrections in evaporation rates and heating rates shown in Fig. 3.20.

not explicitly shown here, compare Fig. 3.21. The presented differences result from effects due to both internal flow dynamics and drop deformations. The observed scatter in the plot is related to variations in drop Reynolds number, Weber number, and viscosity ratio at constant drop distortion. It is important to note that the correction, presented in Fig. 3.22, is largely neglected in today's device-scale simulations performed in academia and industry. However, this analysis illustrates that the consideration of drop coupling dynamics affect mass and energy transfer rates even more significantly than the drag forces from the momentum exchange, compare Fig. 3.19 for reference.

Building on this analysis, the significance of this coupling to turbulent flow simulations is, in what follows, analyzed from a large-eddy simulation of the fuel injection process. Figure 3.23 (top) illustrates this injection process. The liquid drops are color-coded by their local drop Reynolds number which was established as the most meaningful drop parameter in this study, compare discussions of Figs. 3.13 and 3.14, respectively. Figure 3.23 (below, left) presents the effective drop drag coefficient correction, calculated from local drop conditions in the large-eddy simulation using Eq. (2.109) and mapped onto the spatial distance from the injector exit. Note that this correction includes the physical complexities of finite drop viscosity and deformations as discussed in the previous analysis. The mapping process reveals that significant drag coefficient corrections from drop deformations to the solid sphere reference exist close to the injector exit. The analysis discussed above has established that finite drop viscosity effects generally decrease drag forces in relation to rigid spheres. Then, the spatial extend of the region of distinctive drop distortion can be defined, as highlighted in Fig. 3.23 (below, left) (x$<$30 mm). At larger distances, drop Reynolds numbers and Weber numbers diminish. The effect of internal flow dynamics on the drag coefficient, however, persists even under such conditions, consistent with the analysis of Fig. 3.15. This defines the region of drop internal flows, highlighted in Fig. 3.23 (below, left). Figure 3.23 (bottom, right) presents effective drop evaporation rates due to internal flow dynamics, shape distortion corrections to the Sherwood number, and surface area corrections in comparison to the solid sphere

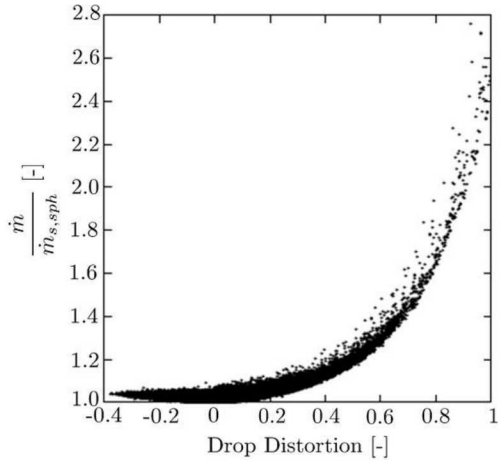

Figure 3.22. Effective evaporation rate corrections in relation to the solid sphere reference, calculated from Eq. (2.130) , as a function of drop distortion.

reference. Corresponding values of drop heating corrections are omitted here since prior analysis has explained and quantified its analogy to drop evaporation, compare Figs. 3.17 and 3.21. The mapping process reveals that significant corrections (5–10%) to the reference evaporation rate exist up to liquid penetration lengths of x<55 mm. The analysis also shows that those corrections, in contrast to corresponding drag coefficient corrections do diminish in the limit of vanishing drop Reynolds numbers and Weber numbers, consistent with Figs. 3.16 and 3.20, respectively.

The past analysis established the significance of the coupling of drop dynamics to its conservation equations for large-eddy simulations. In order to properly capture these coupling dynamics, an adequate time step for Runge-Kutta integration, consistent with Eq. (2.37), must be selected based on the characteristic time scales associated with the relevant physical processes. Figure 3.24 summarizes these relevant time scales. It shows the time-scale ratios of flow-drop momentum (top, left), flow-drop heating (top, right), flow-drop evaporation (bottom, left), and flow-drop oscillation (bottom, right) as a function of the spatial distance from the injector exit. The direct comparison of these time scale ratios reveals that an intense flow-drop oscillation coupling exists, consistent with the spatial extension of the drop distortion regime, defined in Fig. 3.23, at spatial distances of x<30 mm to the injector exit. Hence, the flow-drop oscillation time scale ratio is the most restrictive in this region and determines the Runge-Kutta time-step as a consequence. At larger distances, the flow-drop heating time scale ratio overtakes as the most restrictive time scale ratio. It must be noted, however, that this time scale analysis is performed for each individual drop and can result, due to the large scatter apparent in Fig. 3.24, in different outcomes for individual drops.

The previous statements are useful if viewed as general trends of the development of flow-drop interactions during the simulation. As an exemplarily example, the performance of the effective time-scale selection method is demonstrated on simulations of drop distortions. Corresponding time scales represent the most restrictive characteristic times close to the injector exit. Figure 3.25

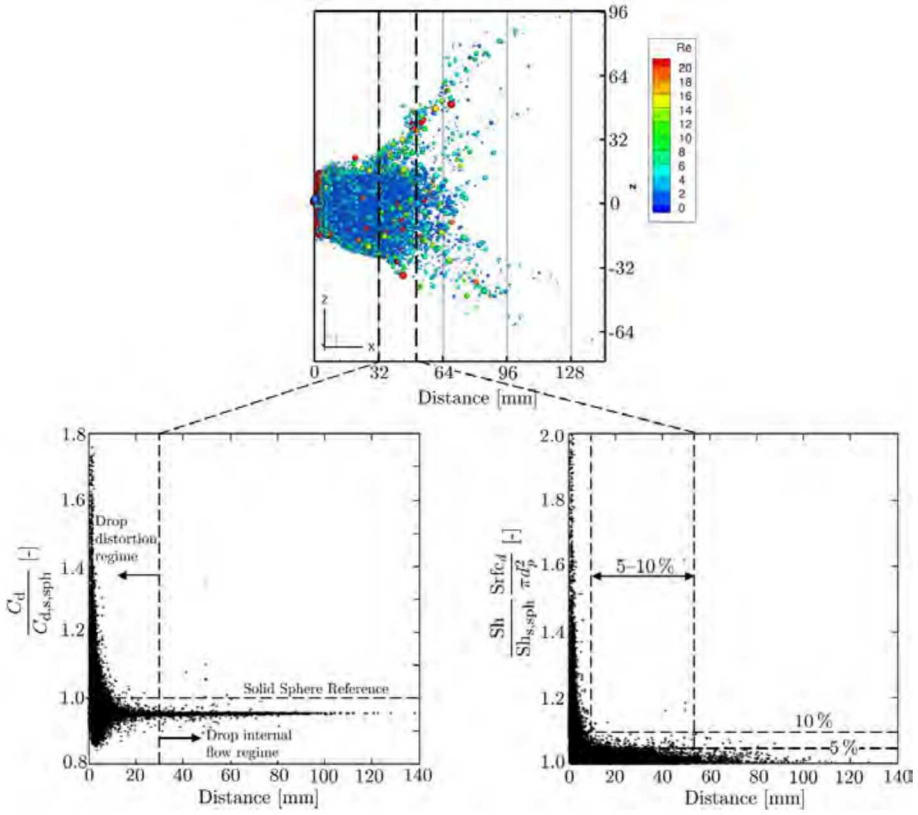

Figure 3.23. (Top) Visualization of the injection process. Liquid drops are color-coded by their drop Reynolds number. (Below) Effective drop drag coefficient correction (left), calculated from Eq. (2.109), and drop evaporation rate (right), calculated from Eq. (2.119), as a function of the spatial distance from the injector exit.

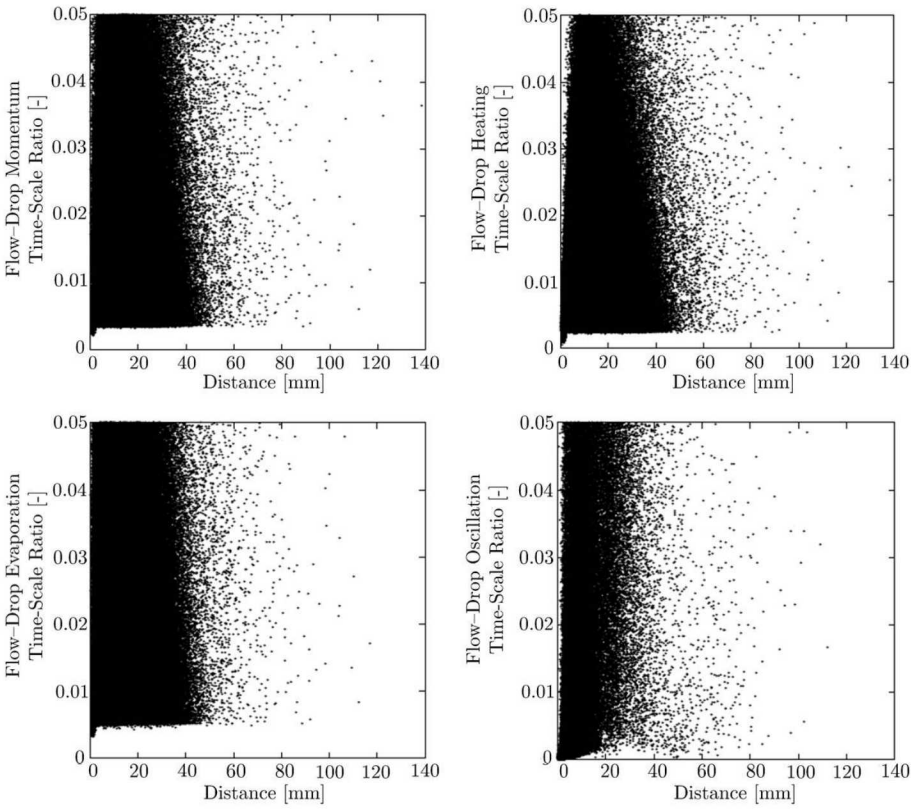

Figure 3.24. Time-scale ratios of flow-drop momentum (top,left), flow-drop heating (top,right), flow-drop evaporation (bottom,left), and flow-drop oscillation (bottom,right). An intense flow-drop oscillation coupling exists, consistent with the spatial extension of the drop distortion regime, defined in Fig. 3.23, at distances less than $\sim$30 mm to the injector exit.

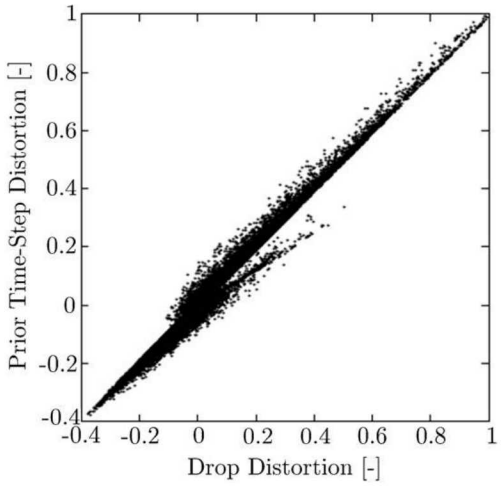

Figure 3.25. Correlation between the simulated drop distortion and its value at the previous time-step demonstrates the temporal resolution of the complex drop dynamics in this simulation.

shows the relation between simulated drop distortions and their value at the previous time-step. The apparent linear relation between the two quantities gives testament to the accurate temporal resolution of the underlying drop dynamics. Note that these dynamics are obtained from the integration of the analytical expression in Eq. (2.86). As a consequence of the analytical character, meaningful drop distortion values may also be obtained at large time steps. In that case, however, the strong positive correlation between drop distortion values between time steps would be lost. That is why Fig. 3.25 represents a meaningful metric to judge upon the time-step selection method for Runge-Kutta integration.

Building on this analysis, representative time-resolved drop states are investigated for an individual drop which exhibits Weber numbers below the critical value. Figure 3.26 (left) presents the drop Weber number and drop Reynolds number distribution. Both parameters decrease over time and the Weber number remains below its critical value during the entire period. Figure 3.26 (right) shows the corresponding drop temperature and diameter. This illustrates that, at the beginning of the drops life time, it undergoes significant heating while drop evaporation remains slow due to low absolute temperatures, consistent with the analysis presented in Fig. 3.6. As a consequence, the drop initially expands in size due to the corresponding decrease of the liquid drop density. Once the drop temperature exceeds $T \approx 460$ K, significant drop evaporation rates develop and further drop heating is prohibited due to balancing rates of latent heat. Then, the drop diameter decreases due to evaporation. Figure 3.27 presents the temporal evolution of drop distortions (left) and distortion velocities (right). The amplitude of drop distortions decreases over time due to diminishing Weber numbers, compare Fig. 3.26. Drop distortions never exceed the breakup criterion of y=1. The drop Weber numbers locate the drops state inside the oscillatory deformation regime within the drop distortion and breakup regime map, shown in Fig. 3.9. Consistent with the observed decrease of drop oscillations, the corresponding distortion velocities also diminish due to reduced forcing and

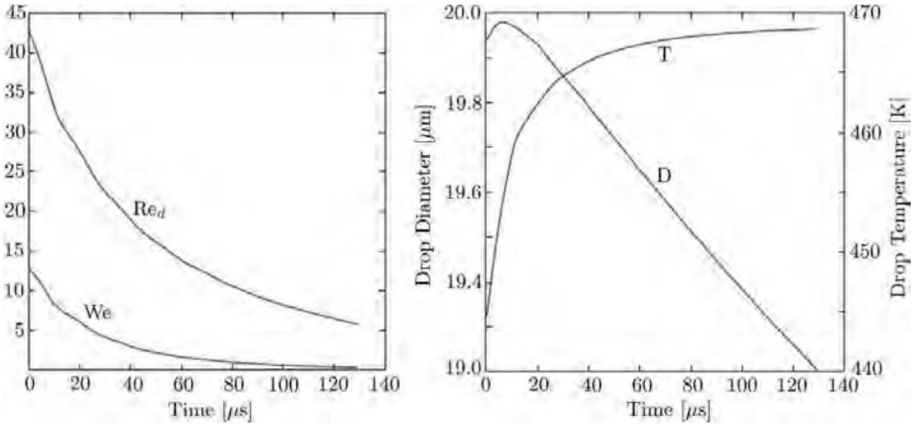

Figure 3.26. (Left) Individual drop Weber number and Reynolds numbers as a function of time. (Right) Drop temperature T and diameter D.

the drops natural damping. The drops oscillation also translates into resulting corrections to the drag law and to the drops evaporation and heating rates in comparison to solid sphere reference values, as shown in Fig. 3.28.

Consistent with prior analysis, the effective drag coefficient correction comprises both increases and decreases in comparison to the reference value. This reflects the oscillatory deformations into oblate and prolate spheroids, respectively. It is also noted that the drag coefficient correction saturates at a corresponding value of $\sim$0.95 due to the persistent effect of finite drop viscosity even at low drop Reynolds numbers. Figure 3.28 (right) shows that respective mass and energy transfer rate corrections diminish, while significant at first, with decreasing oscillation amplitudes. In contrast to this analysis on drop oscillation dynamics, Fig. 3.29 (left) presents the temporal evolution of a drop Weber number and drop Reynolds number where the corresponding Weber number exceeds its critical value. Then, the drop state is located inside the bag breakup regime. Hence, the drop distortion exceeds the breakup criterion y=1 without the formation of drop oscillations, as shown in Fig. 3.29 (right). The time period up to the point when the breakup criterion is fulfilled defines the breakup time, which results in $\Delta t \approx 18.5\mu$s under the conditions here. The corresponding ratios between the effective drag coefficient, calculated from Eq. (2.109), to the solid sphere reference is shown in Fig. 3.30 (left). Its temporal evolution qualitatively resembles the drop distortion parameter. The effective drag coefficient correction increases monotonically until drop breakup occurs. The respective corrections for drop evaporation and heating, calculated from Eqs. (2.119), (2.124), or (2.124), are presented in Fig. 3.30 (right) as a function of the drops lifetime. They show similar trends with a consistently larger correction to the evaporation rate in comparison to drop heating. This analysis has demonstrated that the detailed drop dynamics of internal flow fields and drop distortions and oscillations may significantly effect the interphase exchange functions in turbulent combustion simulations. As a consequence, large-eddy simulations of a fuel injection process must apply an adequate temporal resolution of corresponding rate-determining effects.

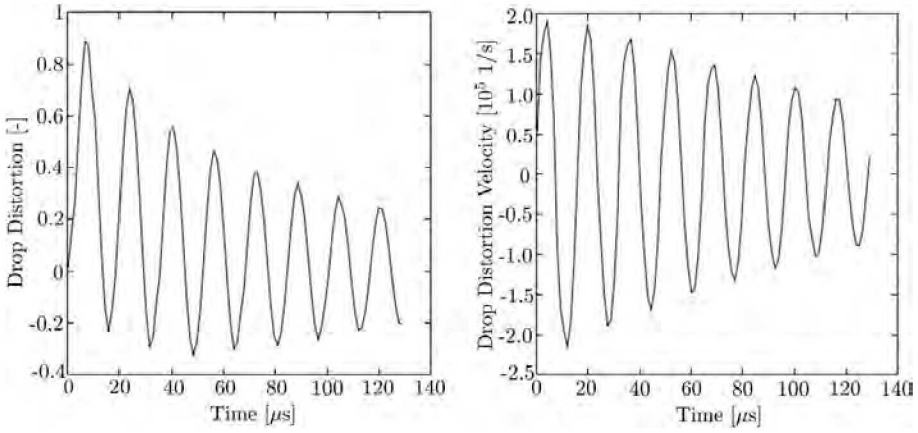

Figure 3.27. Individual drop distortion (left) and drop distortion velocity (right) as a function of time. The amplitude of the oscillation decreases due to diminishing Weber numbers, compare Fig. 3.26.

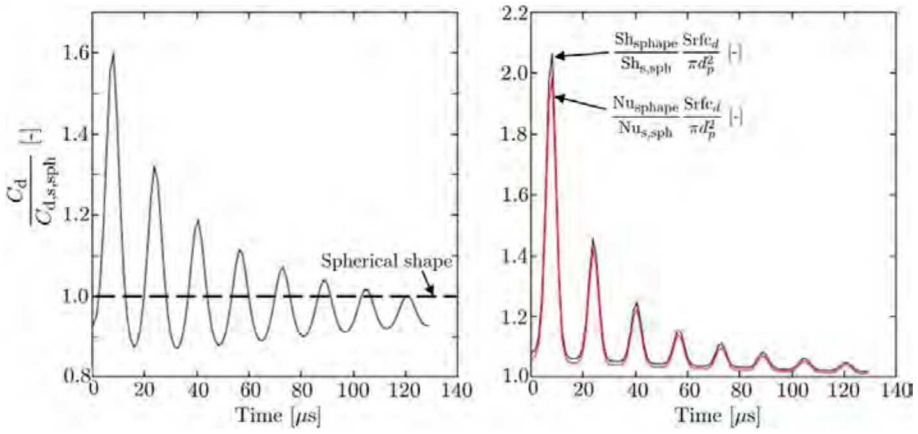

Figure 3.28. Ratio between the effective drag coefficient, calculated from Eq. (2.109), to the solid sphere reference (left) as a function of time. (Right) The respective corrections for drop evaporation and heating, calculated from Eqs. (2.119), (2.124), or (2.124), as a function of time.

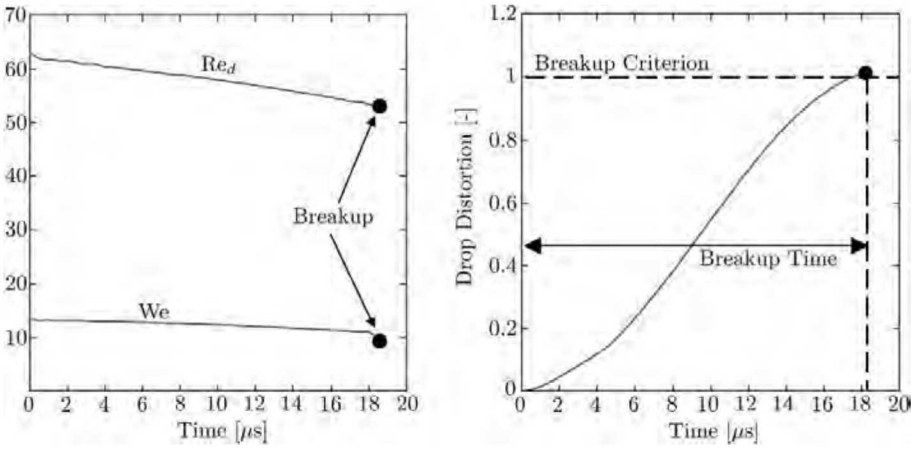

Figure 3.29. (Left) Individual drop Weber and Reynolds numbers as a function of time. Drop breakup occurs due to higher than critical Weber numbers (We$_c$=12). (Right) Drop distortion shows, consistent with the distortion and breakup regime map of Hsiang and Faeth [38], no drop oscillations in the bag breakup regime before breakup.

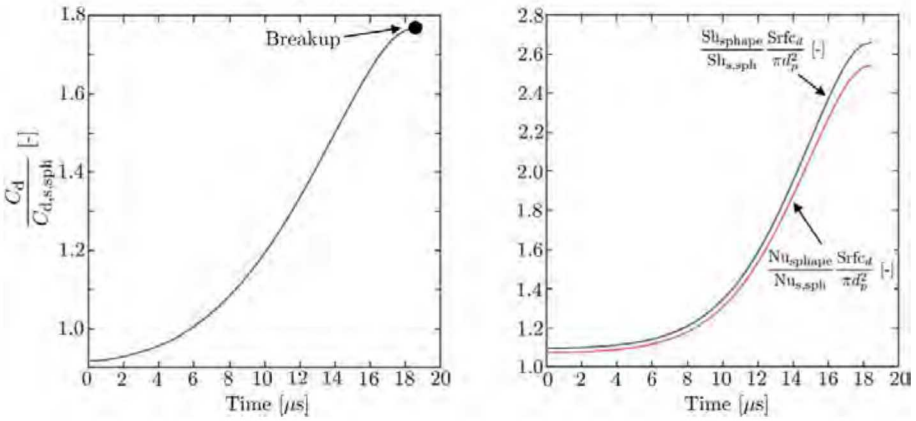

Figure 3.30. Ratio between the effective drag coefficient, calculated from Eq. (2.109), to the solid sphere reference (left) as a function of time. (Right) The respective corrections for drop evaporation and heating, calculated from Eqs. (2.119), (2.124), or (2.124), as a function of time.

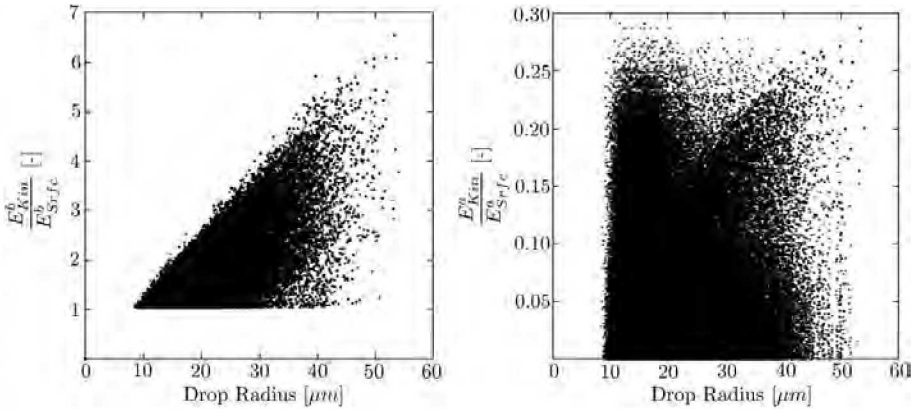

Figure 3.31. Ratio of kinetic energy to surface energy of drops before (left) and after breakup (right), calculated by Eqs. (2.149) and (2.152), respectively, conditioned on the drop radius of the drops at critical deformation $y = 1$.

Having established the capability of predicting the drop and flow dynamics up to the point in time when breakup occurs, the following analysis focuses on the refined framework, defined in Eq. (2.153), to model the breakup event. The starting point is the analysis of the energy equation which relates drop properties before breakup to corresponding drop properties after breakup. The energy of the drops is computed from contributions of kinetic energy and surface energy, as defined in Eq. (2.149). Figure 3.31 (left) presents the ratio of those energy contributions for drops before breakup, conditioned on the time when breakup occurs, and as a function of the corresponding drop radius. It is observed that, with increasing drop size, the contribution of the kinetic energy generally increases while the contribution of the surface energy diminishes. In contrast, Fig. 3.31 (right) presents the ratio of kinetic energy to surface energy of drops after breakup, as defined in Eq. (2.152), conditioned on the breakup time and as a function of the drop radius. Note that this drop radius still refers to the corresponding size of the original drop before breakup, consistent with Fig. 3.31 (left). The analysis shows that, compared to the state before breakup, the ratio of energy contributions has reversed. The breakup event has re-distributed the energy, which was mainly contained in the kinetic state, to the surface energy. Hence, drop properties after breakup are significantly affected by the contribution of the surface energy which, as a consequence, has to be carefully modeled. Figure 3.31 (right) also indicates that the contribution of the surface energy increases with increasing drop sizes.

In the following, the scaling of these energy ratios, which carries important implications for the modeling effort as demonstrated below, is investigated further. Figure 3.32 (left) shows the square of the natural oscillation frequency which contributes in this form to the kinetic energy of drops before breakup, compare Eq. (2.149). It is calculated from Eq. (2.92). It is also noted that the oscillation frequency utilized here includes, in contrast to the original breakup model formulation from O'Rourke and Amsden [67], the reciprocal damping time. The original model utilizes the complete definition of the oscillation frequency in the calculation of the drop dynamics

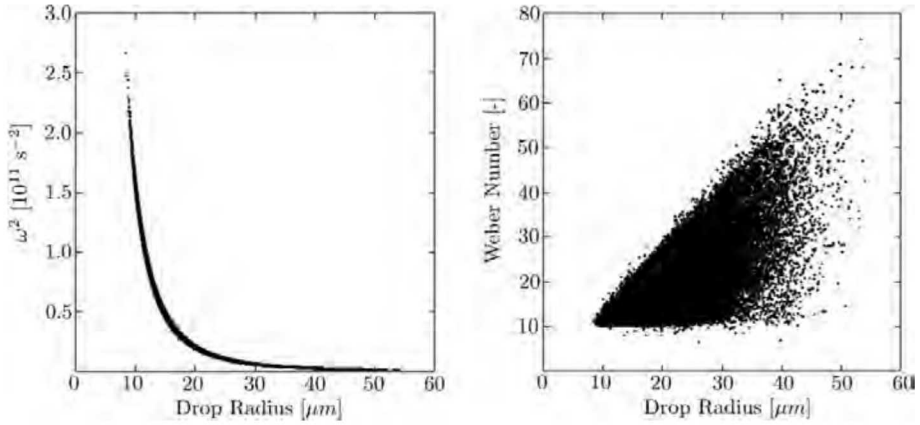

Figure 3.32. (Left) Square of the natural oscillation frequency, calculated by Eq. (2.92), and (right) drop Weber number, conditioned on the drop radius of the drops at critical deformation $y = 1$.

as determined by Eq. (2.86) but not in the calculation of the breakup event. Under the conditions here, however, effects of liquid viscosity as quantified by the Ohnesorge number contribute, while not significantly affecting the overall drop dynamics, to the oscillation dynamics as highlighted in Fig. 3.9. The analysis shows that the energy contained in the oscillation frequency diminishes with increasing drop radius, consistent with its fundamental definition. Figure 3.32 (right) presents the drop Weber number at breakup as a function of the drop radius which shows a similar distribution in comparison to Fig. 3.31 (left).

Figure 3.33 presents a side-by-side comparison of the square of the oscillation frequency (left) and the square of the drop distortion velocity (right) at the time of breakup. It is observed that, with increasing Weber numbers, the contribution of the oscillation frequency diminishes and the kinetic energy in the drop distortion velocity becomes the main contributor to the energy budget of drops before breakup. It is important to note that this shift in the energy contributions occurs within the same breakup regime of bag breakup and multimode breakup and over a range of Weber numbers where TAB breakup model is valid. This conclusion is difficult to obtain from asymptotic analysis of the corresponding equations. Informed by this analysis, the refined breakup model developed here includes the complete definition of the oscillation frequency, as shown in the last term of Eq. (2.149). It was shown that Ohnesorge number effects do modify this oscillation frequency, compare Fig. 3.9. It is important to realize that this frequency, while negligible for prior drop distortion dynamics in this Weber number range as quantified by Eq. (2.86), dominates the kinetic energy budget of drops before breakup at low Weber numbers, as shown in Fig. 3.33. This motivates the inclusion of the full complexity of the oscillation frequency in Eq. (2.149). With increasing Weber numbers, however, this effect diminishes and is being replaced by contributions of drop distortion velocities, as apparent from Fig. 3.33. Such distortion velocities dy/dt of the drop poles and their relation to perpendicular expansion velocities dH/dt are illustrated in the sketch of Fig. 3.34. At the time of critical drop distortion ($y = 1$), the drop has deformed into an oblate spheroid, well-defined by TAB model, as detailed in, for example, Eq. (2.140). Due to this defor-

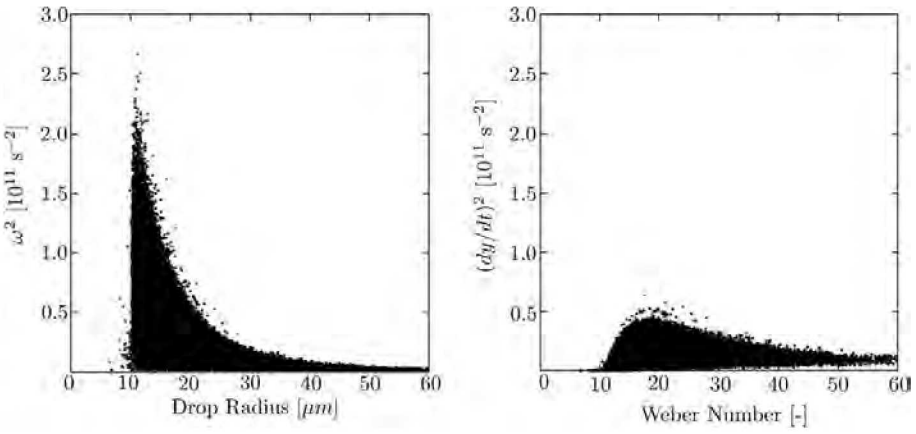

Figure 3.33. (Left) Square of the natural oscillation frequency, calculated by Eq. (2.86), and (right) drop distortion velocity, calculated by Eq. (2.93), as a function of the Weber number, conditioned on the time of breakup.

mation, the resulting expansion velocities dH/dt, which transform into translational velocities of drops after breakup, are distinctively different than the drop pole velocity directly calculated by TAB model from Eq. (2.93). As a consequence, equations for the calculation of these expansion velocities, provided in Eqs. (2.147) and (2.148), have been added to the breakup model to improve its accuracy for larger Weber numbers where the kinetic energy is dominated by the distortion velocity, as discussed above.

As demonstrated in Fig. 3.31, the energy budget of drops immediately after breakup is dictated by the surface energy. Hence, its accurate calculation is imperative for proper breakup modeling. At first, the surface area of the deformed drop at the time of breakup and when the drop poles meet at its center is calculated from Eq. (2.141). It is important to realize that the inclusion of the Sauter mean radius in Eq. (2.152) relates the total surface area of all drops after breakup to the (well-defined) surface area of the original deformed drop before breakup. It is noteworthy that the effect of drop deformation on the surface area at the time of critical distortion $y = 1$ is neglected in the original formulation from O'Rourke and Amsden [67], as shown in the first term of Eq. (2.134). Next, the surface tension force, multiplied by the surface area (Eq. (2.141)) to obtain the surface energy, is calculated from detailed mean-field molecular two-phase interface calculations, defined in Eq. (2.81) and exemplarily shown in Fig. 3.8. These simulations facilitate fundamentally-consistent surface tension calculations in multicomponent mixtures over a wide range of conditions. Results of these simulations are presented in Fig. 3.35 which shows a wide scatter of surface tension forces over drops of all radii. This reinforces the significance of accurate calculations of surface tension forces from local drop conditions, obtained from large-eddy simulations.

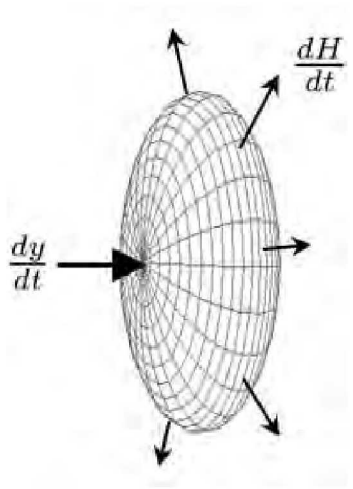

Figure 3.34. Sketch of the distortion velocity dy/dt of the drop poles, as calculated by Eq. (2.93), and the resulting perpendicular expansion velocities dH/dt at the time of critical distortion $y = 1$.

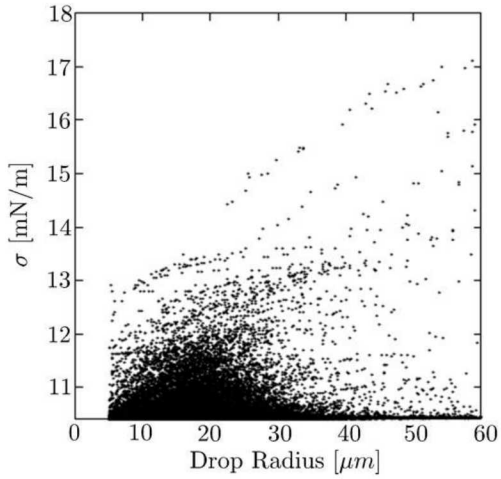

Figure 3.35. Distribution of surface tension values over drops with different radii.

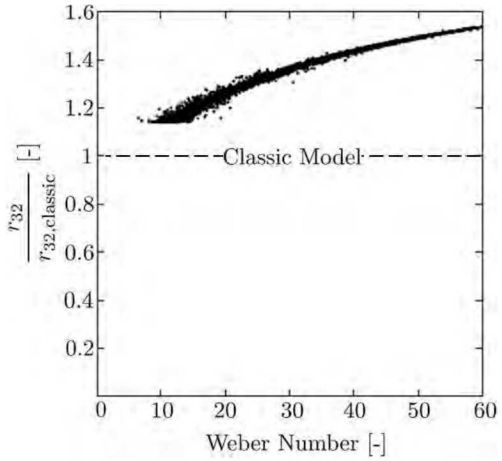

Figure 3.36. Ratio of Sauter mean radius obtained by the breakup model, defined in Eq. (2.153), to the original formulation proposed by O'Rourke and Amsden [67], conditioned on the Weber number at the time of breakup.

The presented set of modeling advancements is compiled into a refined model for breakup, presented in Eq. (2.153) in its final form. Figure 3.36 presents the ratio of Sauter mean radius predictions from this framework to predictions from the original formulation proposed by O'Rourke and Amsden [67]. It is clarified that results from both models are simultaneously calculated during the large-eddy simulation and that, as a consequence, both models operated under the exact same conditions in order to facilitate a meaningful comparison. The presented ratio of the two model predictions illustrates the significance of the introduced modeling refinements and its dependency upon the Weber number. As discussed above, the significance of the individual modeling advancements strongly depends on the Weber number. It is observed from Fig. 3.36 that the new framework consistently predicts a larger Sauter mean radius of drops after breakup in comparison to the reference solution from O'Rourke and Amsden. It is also noted that, with increasing Weber numbers, the difference between the two models also increases.

Under the conditions here, the presented framework calculates a Sauter mean radius which is about 50% higher than the corresponding radius calculated by the classic model at a Weber numbers of We ≈ 60. In this context, it is noteworthy that many studies in the past from academia and industry have shown that the predicted drop sizes after breakup, obtained from the classic model, are often significantly under-predicted [42, 52, 97–99, 103]. The extent of the under-prediction reported in these studies is similar to the magnitude of the modifications which result from this work. It is also noteworthy that the present framework does not introduce new modeling constants as it is entirely based on conservation equations.

The improved modeling framework is utilized to quantify effects of modeling errors to the resulting error in the calculation of the Sauter mean radius. The corresponding analysis has highlighted the significance of surface tension forces to proper breakup modeling as follows. Fig-

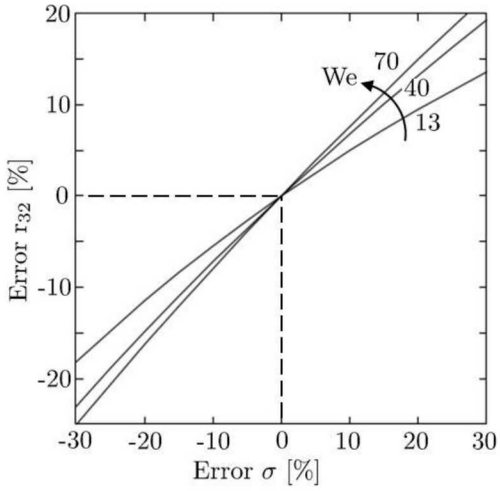

Figure 3.37. Relation between errors in the computation of surface tension values and the resulting errors in the prediction of the Sauter mean radius with increasing Weber numbers.

ure 3.37 quantifies the resulting errors in predicted Sauter mean radius due to errors in the simulated value of surface tension forces. The input errors are obtained by artificial modifications of prior detailed mean-field surface tension calculations from Eq. (2.81). The analysis illustrates that a quasi-linear relationship exists between errors in surface tension forces and its corresponding impact on the predicted Sauter mean radius. The impact of errors in surface tension increases with the Weber number. It is noted that surface tension forces, even in high-fidelity simulations, are not necessarily calculated as rigorously as performed in this study [35, 36, 111]. Hence, the error range assumed in Fig. 3.37 appears conservative and highlights the opportunity for further improvements in simulations performed in industry and academia.

In the following, the refined model for drop velocity predictions after breakup is presented. The starting point is the widely-accepted method to calculate the velocities of newly created drops, perpendicular to the flow direction of the original drop before breakup, from Eq. (2.137). The exact direction is obtained by random sampling. In what follows, it is illustrated, however, that this scheme generally violates the conservation of momentum. As shown in Fig. 3.34, the perpendicular velocity dH/dt originates from the kinetic energy stored in the drop oscillation of the original drops poles before breakup. It is important to realize that this oscillation has not contributed to the original drop momentum which solely resulted from its translational motion. After breakup, however, this oscillation is transformed into a translational motion of the new drops which carry momentum as a consequence. Drop momentum conservation then requires the solution of Eq. (2.156). Figure 3.38, however, shows the resulting drop momentum as a solution to the left-hand-side of Eq. (2.156), obtained by classic random sampling as discussed above, normalized by the reference drop momentum of the original drop $p = m_0 \cdot dH/dt$, defined in Eqs. (2.155) and (2.147). The analysis demonstrates that, without an explicit enforcement of momentum conservation in the calculation of the drop velocities, momentum conservation is violated in a non-negligible manner.

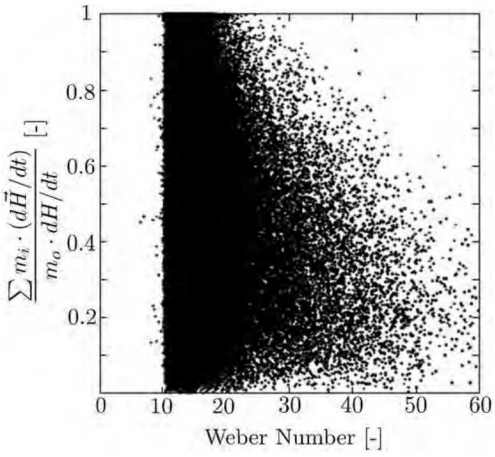

Figure 3.38. Ratio of resulting drop momentum, calculated from the left-hand-side of Eq. (2.156), to the drop reference momentum $p = m_0 \cdot dH/dt$, defined in Eqs. (2.155) and (2.147). The calculations were performed using the classic method based on random sampling without explicit enforcement of momentum conservation. As demonstrated in Eq. (2.156), the shown momentum ratio is required to be zero if momentum is conserved. The momentum ratio is presented as a function of the Weber number.

As demonstrated in Eq. (2.156), this ratio is required to be zero if momentum is conserved. It is essential to realize that the number of newly created drops, while depending on the computed ratio r/r_{32}, is generally insufficient to guarantee an approximate solution of Eq. (2.156) using statistical sampling. Furthermore, respective drop masses and drop velocities are both chosen randomly and independently of each other. As a consequence, a large number of drop samples would be required for a statistical solution of Eq. (2.156) which is, conceptually, not realizable by the physical process of drop breakup within breakup regimes modeled by TAB.

Informed by the analysis above, the current framework explicitly enforces drop momentum conservation after breakup by calculating the velocity vector of the largest drop from Eq. (2.158). Figure 3.39 (left) presents the ratio of this calculated correction velocity magnitude to the reference normal velocity magnitude as a function of the Weber number. It is noted that the mass-based criterion for the drop selection guarantees its meaningful velocity. Energy conservation is subsequently reinstated by the scaling operation of all drop normal velocity magnitudes as defined in Eq. (2.161). Figure 3.39 (right) presents this scaling parameter as a function of the Weber number. The magnitude of the corrections, quantified in Fig. 3.39, reinforces the significance of the explicit enforcement of momentum conservation after breakup as applied in this framework.

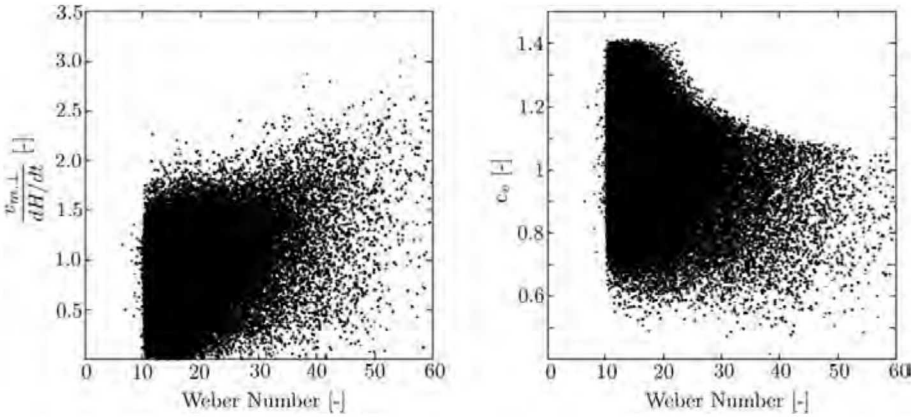

Figure 3.39. (Left) Ratio of the correction velocity magnitude of the largest mass drop, defined by Eq. (2.158), and the reference normal velocity magnitude dH/dt, defined by Eq. (2.147), as a function of Weber number. (Right) Energy conservation scaling factor, calculated from Eq. (2.161), for all drop normal velocity magnitudes as a function of Weber number.

This page intentionally left blank.

Chapter 4

Summary and Conclusion

Over the past three decades, two classes of models have emerged for the simulation of atomization and breakup processes and have entered into academic and commercial fluid flow software. The first is the classic WAVE model and the second is the Taylor Analogy Breakup (TAB) model on which the current work was based on. The TAB model is built upon Taylor's analogy between drop dynamics and a forced spring-mass-damper system. It explicitly models the deformation and oscillation of drop dynamics and assumes that drop breakup occurs as soon as oscillations of the drop poles meet at the drop center. Then, an energy equation is consulted to predict the properties of newly created drops after breakup. The model is conceptually valid for a wide range of Ohnesorge numbers and Weber numbers up to the regime of shear breakup.

At higher Weber numbers, drop breakup is increasingly determined by surface stripping processes for which the utilized forced spring-mass-damper system is not necessarily a meaningful surrogate model. Since its original introduction, however, many studies from academia and industry have shown that the predicted drop sizes after breakup are often significantly under-predicted and that deficiencies in the prediction of the spray angle, to which the breakup model contributes, exist. These deficiencies, along with the attempt to extend the validity of TAB model to higher Weber number regimes, have mainly motivated further developments since. Over the last twenty years, two major advancements to the original formulation have emerged. The first is represented by the Enhanced Taylor Analogy Breakup (ETAB) model. It introduced the "ETAB-law" which postulates that the rate of drop creation after breakup is proportional to the number of critically deformed drops. It was noted, however, that the physical basis of this law is not yet rigorously established and that the respective proportionality constants must be set, dependent on the breakup regime, to match experimental data. A subsequently applied smoothing function guarantees a continuous distribution of the value of the proportionality constant across the different breakup regimes. A uniform drop size distribution after breakup is applied which is not necessary supported by experimental evidence of drop breakup in relevant regimes. Further, ETAB tunes the initial rate of drop deformation to extend the breakup time in order to match experimentally determined values of jet breakup lengths. More recently, the Cascade Atomization and Drop Breakup (CAB) model was introduced as a further development of ETAB model. This model builds on the "ETAB-law" in an attempt to extend its applicability to the catastrophic breakup regime relevant for near-nozzle regions. Additionally, the CAB model constant has been selected to naturally guarantee its continuous distribution across the different breakup regimes without the utilization of a smoothing function as previously required in ETAB.

Despite these advancements, the atomization and breakup dynamics of liquid drops are still not well described in models. In previously developed frameworks for device-scale turbulent combustion simulations, the coupling of drop distortion, oscillation, breakup, and internal flow dynamics to the conservation equations is, despite its relevance, largely neglected. However, a common exception to this statement is represented by the dynamic drag model which is widely applied in academia and industry to account for the effect of drop distortion on its aerodynamic drag. This correction to the drag law is facilitated by a linear interpolation between the drag of a sphere and the drag of a disc. Further, this widely-applied drag correction model is only valid and utilized for positive distortions. Hence, it neglects deformations into prolate spheroids which naturally occur during drop oscillations.

Recent studies have raised concerns about the validity of the applied linear interpolation scheme between reference drag coefficients over the range of relevant drop Reynolds numbers. Further to these limitations, effects on drop heat and mass transfer rates which originate from the coupling of drop dynamics and internal flow dynamics are also relevant but are still largely neglected in device-scale turbulent combustion simulations. Widely-accepted formulations utilize relations for quiescent drop evaporation and heating and correct those for effects of flow convection around a sphere. As a consequence, the analogy to a solid sphere is utilized as an underlying assumption of these frameworks which is, as demonstrated in the current study, questionable in liquid fuel injection processes where the fuel drops are generally not in equilibrium with the flow.

The current work has introduced a fundamentally-consistent framework suitable for large eddy simulations to understand and quantify the effects of drop oscillations, internal flow dynamics, and breakup processes on mass, momentum, and energy exchange functions. This framework is based on the TAB model which naturally quantifies local drop deformation dynamics. It was also established that TAB model is valid over the full range of drop conditions typically encountered. Real-fluid thermodynamic property modeling and Gradient Theory facilitated accurate calculations of molecular two-phase interface exchange functions, surface tensions forces, drop oscillations and breakup processes. Statistical analysis from local drop flow and thermodynamic states established the drop Reynolds number as the most important parameter to describe the coupling of drop dynamics and interface exchange functions. This is a non-trivial conclusion since drop dynamics are determined by the temporal evolution of the drop distortion. Drop deformations, however, are mainly determined by the Weber number as the main parameter of widely-accepted regime diagrams for drop deformation and breakup. However, the analysis revealed a strong correlation between the local drop Weber number and the local drop Reynolds number. Both parameters are mainly determined by the local slip velocity. As a consequence to the non-linear effect of fluid dynamics around the drop, quantified by the Reynolds number, local drop oscillations are determined by the Weber number while the resulting coupling dynamics to the turbulent flow are determined by the Reynolds number.

Building on this analysis, the resulting drag coefficient was shown to significantly deviate from the classic dynamic drag model which is widely applied in academia and industry. It was established that negative drop distortions, which naturally occur during drop oscillations, significantly reduce drag forces. This physical complexity, however, is neglected in the dynamic drag model. Furthermore, it was shown that harmonic drag coefficient oscillations exhibit, contrary to the pos-

tulated linear scaling assumption of the dynamic drag model, an exponential scaling with the drop distortion. It was also established that the dynamic drag model, which assumes a sharp-edged disc as a reference shape at the critical deformation before breakup, generally significantly over-predicts the resulting drag forces as a consequence. Finally, effects of internal flow dynamics were shown to consistently and distinctively reduce drag forces not accounted for in the dynamic drag model. The analysis also revealed that effects which originate from internal drop flows have a lasting effect for the full lifetime of the drop since they do not diminish when the liquid drops equilibrate with the flow. The framework also quantified corresponding effects on evaporation and heating rates, which are largely neglected in modern simulations performed in academia and industry. It was found, however, that the consideration of drop coupling dynamics affect such mass and energy transfer rates even more significantly than the drag forces from the momentum exchange. While internal flow dynamics decrease the momentum exchange and balance, to some extent, the increased momentum exchange from positive drop distortion, those flow dynamics generally amplify evaporation and heating transport phenomena. In contrast to drag forces, however, this effect does diminish once the liquid drops equilibrate with the flow. The significance of this coupling to turbulent flow simulations in fuel injection processes was analyzed using large eddy simulation. This simulation established the significance of the solution of the fully-coupled system of equations for mass, momentum, energy, and drop oscillations to device-scale turbulent combustion simulations. In order to properly capture these coupling dynamics, an adequate time step method for Runge-Kutta integration was applied based on the characteristic time scales associated with the relevant physical processes at local drop conditions. The simulation proved to be successful in capturing the detailed drop coupling dynamics at Weber numbers which support both drop oscillations without breakup and drop deformations which lead to breakup processes, respectively.

A new set of equations was developed to address the current shortcomings in the prediction of resulting drops properties over the full range of relevant breakup conditions. A refined energy balance equation, which relates predicted drop properties after breakup to the well-known drop properties before breakup, was utilized. Its formulation is facilitated by the fundamental definition of the natural drop oscillation frequency which includes the reciprocal of the damping time. The damping time has been neglected in previous models. It was demonstrated, however, that related Ohnesorge number effects modify the oscillation frequency. It was shown that this frequency, while negligible for prior drop distortion dynamics as quantified by TAB model, dominates the kinetic energy budget of drops before breakup at low Weber numbers. At such Weber numbers, Ohnesorge number effects contribute to the drop breakup process as a consequence and were therefore included in the refined drop breakup model. With increasing Weber numbers, however, this effect was shown to be replaced by contributions of drop pole distortion velocities. These velocities transform into translational velocities of drops after breakup. It was demonstrated, however, that these resulting translational velocities are, in contrast to assumptions in previous frameworks, distinctively different than the drop pole velocities directly calculated by TAB model. Hence, equations for the calculation of the translational velocities have been added to the breakup model to improve its accuracy for larger Weber numbers where the kinetic energy of drops before breakup is dominated by the distortion velocity.

In contrast to the energy budget of drops before breakup, the corresponding budget of drops after breakup was shown to be dominated by the surface energy. Based on this analysis, a new set of equations has been added to calculate the surface area of the deformed drop at the time of breakup. It was shown that previous models neglect this physical complexity since they assume a spherical reference shape in respective calculations. Furthermore, the surface tension force, multiplied by the surface area to obtain the surface energy, was calculated from mean-field molecular two-phase interface calculations. These simulations facilitate fundamentally-consistent surface tension calculations in multicomponent mixtures over a wide range of conditions. It was highlighted that many previous models assume the validity of correlation formulas or constant surface tension values which was not necessarily supported by this study. A wide range of surface tension forces, dictated by the local drop state, was observed. A sensitivity analysis revealed a quasi-linear relationship between the fidelity of surface tension calculations and the corresponding accuracy of predicted Sauter mean diameter of drops after breakup.

A refined model for the calculation of drop velocities after breakup was developed. The development was motivated by an analysis which demonstrated that classic methods of previous models generally violate drop momentum conservation in a non-negligible manner. It was recognized that these drop velocities originate, in part, from the kinetic energy stored in the drop oscillation of the drop before breakup. As a consequence, this oscillation has not contributed to its drop momentum which solely resulted from its translational motion. After breakup, however, this oscillation is transformed into a translational motion of the new drops which carry momentum as a consequence. Hence, a new set of equations was added to the breakup model to enforce momentum conservation while retaining energy conservation in the calculation of drop velocities after breakup. It is worth noting that the presented modeling advancements are entirely derived from conservation equations for mass, momentum, and energy and do not, as a consequence, introduce new modeling constants.

References

[1] B. Abramzon and W. A. Sirignano. Droplet vaporization model for spray combustion calculations. *Int. J. Heat Mass Transfer*, 32:1605–1618, 1989.

[2] A. A. Amsden, P. J. O'Rourke, and T. D. Butler. Kiva ii: A computer program for chemically reactive flows with sprays. *Technical Report LA-11560-MS, Los Alamos National Laboratory*, 1989.

[3] Y. Bhatt, D. Arora, R. Shaw, and V. Golubev. Numerical simulations and performance comparison of air-blast and pressure jet atomizers. *AIAA*, 2011-277, 2011.

[4] R.B. Bird, W.E. Stewart, and E.N. Lightfoot. *Transport Phenomena*. John Wiley and Sons, Incorporated, New York, 1960.

[5] R.S. Brodkey. *The Phenomena of Fluid Motions*. Addison Wesley, 1969.

[6] J. W. Cahn and J. E. Hilliard. Free energy of a nonuniform system. i. interfacial free energy. *J. Chem. Phys.*, 28:258–267, 1958. doi: 10.1063/1.1744102.

[7] C. Chryssakis and D. N. Assanis. A unified fuel spray breakup model for internal combustion engine applications. *Atomization and Sprays*, 18:1–52, 2008.

[8] C. T. Crowe, M. P. Sharma, and D. E. Stock. The particle-source-in-cell (psi-cell) model for gas-droplet flows. *Journal of Fluids Engineering*, 99:325–332, 1977.

[9] R. N. Dahms. Gradient theory simulations of pure fluid interfaces using a generalized expression for influence parameters and a helmholtz energy equation of state for fundamentally consistent two-phase calculations. *J. Colloid Interface Sci.*, 445:48–59, 2015.

[10] R. N. Dahms and J. C. Oefelein. On the transition between two-phase and single-phase interface dynamics in multicomponent fluids at supercritical pressures. *Phys. Fluids*, 25: 092103–1–24, 2013. doi: 10.1063/1.4820346.

[11] R. N. Dahms and J. C. Oefelein. Non-equilibrium gas-liquid interface dynamics in high-pressure liquid injection systems. *Proc. Combust. Inst.*, 35, 2014. doi: 10.1016/j.proci.2014.05.155.

[12] R. N. Dahms, T. D. Fansler, M. C. Drake, T.-W. Kuo, A. M. Lippert, and N. Peters. Modeling ignition phenomena in spray-guided spark-ignited engines. *Proc. Combust. Inst.*, 32:2743–2750, 2009. doi: 10.1016/j.proci.2008.05.052.

[13] R. N. Dahms, M. C. Drake, T. D. Fansler, T.-W. Kuo, and N. Peters. Understanding ignition processes in spray-guided gasoline engines using high-speed imaging and the extended spark-ignition model SparkCIMM. Part A: Spark channel processes and

the turbulent flame front propagation. *Combust. Flame*, 158:2229–2244, 2011. doi: 10.1016/j.combustflame.2011.03.012.

[14] R. N. Dahms, M. C. Drake, T. D. Fansler, T.-W. Kuo, and N. Peters. Understanding ignition processes in spray-guided gasoline engines using high-speed imaging and the extended spark-ignition model SparkCIMM. Part B: Importance of molecular fuel properties in early flame front propagation. *Combust. Flame*, 158:2245–2260, 2011. doi: 10.1016/j.combustflame.2011.04.003.

[15] R. N. Dahms, C. Felsch, O. Rohl, and N. Peters. Detailed chemistry flamelet modeling of mixed-mode combustion in spark-assisted HCCI engines. *Proc. Combust. Inst.*, 33:3023–3030, 2011. doi: 10.1016/j.proci.2010.08.005.

[16] R. N. Dahms, M. C. Drake, T. D. Fansler, R. O. Grover, and A. S. Solomon. Detailed simulations of stratified ignition and combustion processes in a spray-guided gasoline engine using the SparkCIMM/G-equation modeling framework. *SAE Int. J. Engines*, 5:141–161, 2012. doi: 10.4271/2012-01-0132.

[17] R. N. Dahms, J. Manin, L. M. Pickett, and J. C. Oefelein. Understanding high-pressure gas-liquid interface phenomena in diesel engines. *Proc. Combust. Inst.*, 34:1667–1675, 2013. doi: 10.1016/j.proci.2012.06.169.

[18] M. C. Drake and D. C. Haworth. Advanced gasoline engine development using optical diagnostics and numerical modeling. *Proc. Combust. Inst.*, 31:99–124, 2007.

[19] M. C. Drake, T. D. Fansler, and A. M. Lippert. Stratified-charge combustion: modeling and imaging of a spray-guided direct-injection spark-ignition engine. *Proc. Combust. Inst.*, 30: 2683–2691, 2005.

[20] J. K. Dukowicz. A particle-fluid numerical model for liquid sprays. *Journal of Computational Physics*, 35:229–253, 1980.

[21] P. Eisenklam and S.A. Arunachalam. The drag resistance of burning drops. *Combust. Flame*, 10, 1966.

[22] P. Eisenklam, S.A. Arunachalam, and J.A. Weston. Evaporation rates and drag resistance of burning drops. *Eleventh Symposium (International) on Combustion*, 11, 1967.

[23] J.F. Ely and H.J.M. Hanley. Prediction of transport properties. 1. viscosity of fluids and mixtures. *Industrial and Engineering Chemistry Fundamentals*, 20, 1981. doi: 10.1021/i100004a004.

[24] J.F. Ely and H.J.M. Hanley. Prediction of transport properties. 2. thermal conductivity of pure fluids and mixtures. *Industrial and Engineering Chemistry Fundamentals*, 22, 1981. doi: 10.1021/i100009a016.

[25] G. M. Faeth. Current status of droplet and liquid combustion. *Progress in Energy and Combustion Science*, 3:191–224, 1977.

[26] G. M. Faeth. Evaporation and combustion in sprays. *Progress in Energy and Combustion Science*, 9:1–76, 1983.

[27] G. M. Faeth. Mixing, transport and combustion in sprays. *Progress in Energy and Combustion Science*, 13:293–345, 1987.

[28] G. M. Faeth and R. S. Lazar. Fuel droplet burning rates in a combustion gas environment. *AIAA Journal*, 9:2165–2171, 1971.

[29] T. D. Fansler, D. L. Reuss, V. Sick, and R. N. Dahms. Combustion instability in spray-guided stratified-charge engines: A review. *Int. J. Engine Res.*, 16:260–305, 2015.

[30] Z.-G. Feng and E.E. Michaelides. Drag coefficents of viscous spheres at intermediate and high reynolds numbers. *J. Fluids Engineering*, 123:841–849, 2001.

[31] G. D. Fisher and T. W. Leland. Corresponding states principle using shape factors. *Industrial and Engineering Chemistry Fundamentals*, 9(4):537–544, 1970.

[32] G.H. Ganser. A rational approach to drag prediction of spherical and nonspherical particles. *Powder Technol.*, 77:143–152, 1993.

[33] A. D. Gosman and E. Ioannides. Aspects of computer simulation of liquid-fueled combustors. *AIAA Paper*, 81-0323, 1981.

[34] A. Haider and O. Levenspiel. Drag coefficient and terminal velocity spherical and nonspherical particles. *Powder Technol.*, 58:63–70, 1989.

[35] M. Herrmann. Detailed numerical simulations of the primary atomization of a turbulent liquid jet in crossflow. *J. Engineering Gas Turbines Power*, 132:061506, 2010.

[36] M. Herrmann. The influence of density ratio on the primary atomization of a turbulent liquid jet in crossflow. *Proc. Combust. Inst.*, 33:2079–2088, 2011.

[37] A. Hölzer and M. Sommerfeld. New simple correlation formula for the drag coefficient of non-spherical particles. *Powder Technol.*, 184:361–365, 2008.

[38] L.-P. Hsiang and G.M. Faeth. Drop deformation and breakup due to shock wave and steady disturbances. *Int. J. Multiphase Fow*, 21:545–560, 1995.

[39] C. Huang and A. Lipatnikov. Modelling of gasoline and ethanol hollow-cone sprays using openfoam. *SAE Technical Paper*, 2011-01-1896, 2011.

[40] G.L. Hubbard, V.E. Denny, and A.F. Mills. Droplet evaporation: Effects of transients and variable properties. *Int. J. Heat Mass Transfer*, 18:1003–, 1975.

[41] D. D. Joseph, J. Belanger, and G. S. Beavers. Breakup of a liquid drop suddenly exposed to a high-speed airstream. *Int. J. Multiphase Flow*, 25:1263–1303, 1999.

[42] E. Kumzerova and T. Esch. Extension and validation of the cab droplet breakup model to a wide weber number range. *Institute for Liquid Atomization and Spray Systems*, 2008-4-5, 2008.

[43] H. Lamb. *Hydrodynamics*. Cambridge University Press, 1932.

[44] J. C. Lasheras and E. J. Hopfinger. Liquid jet instability and atomization in a coaxial gas stream. *Annu. Rev. Fluid Mech.*, 32:275–308, 2000.

[45] C. K. Law. Recent advances in droplet vaporization and combustion. *Progress in Energy and Combustion Science*, 8:171–201, 1982.

[46] J. W. Leach, P. S. Chappelear, and T. W. Leland. Use of molecular shape factors in vapor-liquid equilibrium calculations with the corresponding states principle. *American Institute of Chemical Engineers Journal*, 14(4):568–576, 1968.

[47] T. W. Leland and P. S. Chappelear. The corresponding states principle. a review of current theory and practice. *Industrial and Engineering Chemistry Fundamentals*, 60:15–43, 1968. doi: 10.1021/ie50703a005.

[48] A. Leonard. On the energy cascade in large eddy simulations of turbulent fluid flows. *Technical Report TF-1, Department of Mechanical Engineering, Stanford University, Stanford, California*, 1973.

[49] A. Leonard. Energy cascade in large eddy simulations of turbulent fluid flows. *Advances in Geophysics*, 18:237–248, 1974.

[50] H. Lin, Y.-Y. Duan, and Q. Min. Gradient Theory modeling of surface tension for pure fluids and binary mixtures. *Fluid Phase Equil.*, 254:75–90, 2007. doi: 10.1016/j.fluid.2007.02.013.

[51] A. B. Liu, D. Mather, and R. D. Reitz. Modeling the effects of drop drag and breakup on fuel sprays. *SAE Technical Paper*, 930072, 1993.

[52] A.B. Liu, D. Mather, and R.D. Reitz. Modeling the effects of drop drag and breakup on fuel sprays. *SAE Technical Paper*, 930072, 1993.

[53] R. Manimaran and R. T. K. Raj. Computational studies of swirl ratio and injection timing on atomization in a direct injection diesel engine. *Frontiers in Heat and Mass Transfer*, 5: 1–9, 2014.

[54] J. Manin, M. Bardi, L. M. Pickett, R. N. Dahms, and J. C. Oefelein. Microscopic investigation of the atomization and mixing processes of diesel sprays injected into high pressure and temperature environments. *Fuel*, 134:531–543, 2014. doi: 10.1016/j.fuel.2014.05.060.

[55] B. F. McCoy and H. T. Davis. On the free energy theory of inhomogeneous fluids. *Phys. Rev. A*, 20:1201–1207, 1979. doi: 10.1103/PhysRevA.20.1201.

[56] A. Mejia, J. C. Pamies, D. Duque, H. Seguara, and L. F. Vega. Phase and interface behaviors and type-i and type-v lennard-jones mixtures: Theory and simulations. *J. Chem. Phys.*, 123: 1–10, 2005. doi: 10.1063/1.1955529.

[57] C. Miqueu, B. Mendiboure, and J. Lachaise. Modeling of the surface tension of multi-component mixtures with the gradient theory of fluid interfaces. *Ind. Eng. Chem. Res.*, 44: 3321–3329, 2005. doi: 10.1021/ie049086l.

[58] C. Miqueu, J. M. Miguez, M. M. Pineiro, T. Lafitte, and B. Mendiboure. Simultaneous application of the gradient theory and monte carlo molecular simulation for the investigation of methane/water interfacial properties. *J. Phys. Chem. B*, 115:9618–9625, 2011. doi: 10.1021/jp202276k.

[59] A. A. Moiz, S. Som, L. Bravo, and S.-Y. Lee. Experimental and numerical studies on combustion model selection for split injection spray combustion. *SAE Technical Paper*, 2015-01-0374, 2015.

[60] E. A. Muller and A. Mejia. Interfacial properties of selected binary mixtures containing n-alkanes. *Fluid Phase Equilibria*, 282:68–91, 2009. doi: 10.1016/j.fluid.2009.04.022.

[61] J. C. Oefelein. *Simulation and Analysis of Turbulent Multiphase Combustion Processes at High Pressures*. PhD thesis, The Pennsylvania State University, 1997.

[62] J. C. Oefelein, V. Sankaran, and T. G. Drozda. Large eddy simulation of swirling particle-laden flow in a model axisymmetric combustor. *Proceedings of the Combustion Institute*, 31:2291–2299, 2007.

[63] J. C. Oefelein, R. N. Dahms, and G. Lacaze. Detailed modeling and simulation of high-pressure fuel injection processes in diesel engines. *SAE Intl. J. Engines*, 5:1410–1419, 2012. doi: 10.4271/2012-01-1258.

[64] J. C. Oefelein, G. Lacaze, R. N. Dahms, A. Ruiz, and A. Misdariis. Effects of real fluid thermodynamics in high-pressure fuel injection processes. *SAE Intl. J. Engines*, 7:1125–1136, 2014. doi: 10.4271/2014-01-1429.

[65] J.C. Oefelein. Large eddy simulation of turbulent combustion processes in propulsion and power systems. *Progress in Aerospace Sciences*, 42:2–37, 2006. doi: 10.1016/j.paerosci.2006.02.001.

[66] P. J. O'Rourke. *Collective Drop Effects on Vaporizing Liquid Sprays*. PhD thesis, Princeton University, 1981.

[67] P.J. O'Rourke and A.A. Amsden. The tab method for numerical calculation of spray droplet breakup. *SAE Technical Paper*, 872089, 1987.

[68] K. S. Pitzer. Corresponding states for perfect liquids. *J. Chem. Phys.*, 7:583–590, 1939.

[69] A. Putnam. Integratable form of droplet drag coefficient. *ARS Journal*, 31:1467–1468, 1961.

[70] S. Ramanujan. Modular equations and approximations to pi. *Quart. J. Pure App. Math*, 45: 350–372, 1914.

[71] W. E. Ranz and W. R. Marshall. Evaporation from drops. *Chemical Engineering Progress*, 48:141–173, 1952.

[72] R. C. Reid, J. M. Prausnitz, and B. E. Polling. *The Properties of Liquids and Gases*. McGraw-Hill, New York, 1987.

[73] R. D. Reitz. Modelling atomization processes in high-pressure vaporizing sprays. *Atomization and Spray Technology*, 3:309–337, 1987.

[74] R. D. Reitz and F. V. Bracco. Mechanism of atomization of a liquid jet. *Phys. Fluids*, 25: 1730–1742, 1982.

[75] R. D. Reitz and R. Diwakar. Structure of high-pressure fuel sprays. *SAE Paper*, 870598, 1987.

[76] L. M. Ricart, J. Xin, G. R. Bower, and R. D. Reitz. In-cylinder measurement and modeling of liquid fuel spray penetration in a heavy-duty diesel engine. *SAE Technical Paper*, 971591, 1997.

[77] A. Richter and P.A. Nikrityuk. Drag forces and heat transfer coefficients for spherical, cuboidal and ellipsoidal particles in cross flow at sub-critical reynolds numbers. *Int. J. Heat Mass Transfer*, 55:1343–1354, 2012.

[78] J. S. Rowlinson. Translation of j. d. van der waals' "the thermodynamic theory of capillarity under the hypothesis of a continuous variation of density. *J. Stat. Phys*, 20:200–244, 1979.

[79] J. S. Rowlinson and I. D. Watson. The prediction of the thermodynamic properties of fluids and fluid mixtures–i. the principle of corresponding states and its extensions. *Chem. Eng. Sci.*, 24:1565–1574, 1969. doi: 10.1016/0009-2509(69)80095-3.

[80] S. S. Sazhin. Advanced models of fuel droplet heating and evaporation. *Prog. Energy Combust. Sci.*, 32:162–214, 2006.

[81] K. A. G. Schmidt, G. K. Folas, and B. Kvamme. Calculation of the interfacial tension of methane-water system with the linear gradient theory. *Fluid Phase Equil.*, 261:230–237, 2007. doi: 10.1016/j.fluid.2007.07.045.

[82] P. Senecal, E. Pomraning, K. Richards, and S. Som. An investigation of grid convergence for spray simulations using an les turbulence model. *SAE Technical Paper*, 2013-01-1083, 2013.

[83] P. K. Senecal, K. J. Richards, E. Pomraning, T. Yang, M. Z. Dai, R. M. McDavid, M. A. Patterson, S. Hou, and T. Shethaji. A new parallel cut-cell cartesian cfd code for rapid grid generation applied to in-cylinger diesel engine simulations. *SAE Technical Paper*, 2007-01-0159, 2007.

[84] J. S. Shuen. *A Theoretical and Experimental Investigation of Turbulent Sprays*. PhD thesis, The Pennsylvania State University, 1984.

[85] W. A. Sirignano. Fuel droplet vaporization and spray combustion theory. *Prog. Energy Combust. Sci.*, 9:291–322, 1983.

[86] W. A. Sirignano. Fuel droplet vaporization and spray combustion theory. *Progress in Energy and Combustion Science*, 9:291–322, 1983.

[87] W.A. Sirignano. *Fluid Dynamics and Transport of Droplets and Sprays*. Cambridge Uni. Press, 1999.

[88] J. Smagorinsky. General circulation experiments with the primitive equations. I. The basic experiment. *Monthly Weather Review*, 91:99–164, 1963.

[89] S. Som and S. K. Aggarwal. Assessment of atomization models for diesel engine simulations. *Atom. Sprays*, 19:885–903, 2009.

[90] M. Sommerfeld and H.-H. Qiu. Detailed measurements in a swirling particulate two-phase flow by a phase-doppler anemometer. *International Journal of Heat and Fluid Flow*, 12(1): 20–28, 1991.

[91] M. Sommerfeld and H.-H. Qiu. Characterization of particle-laden, confined swirling flows by phase-doppler anemometry and numerical calculation. *International Journal of Multiphase Flow*, 19(6):1093–1127, 1993.

[92] M. Sommerfeld, A. Ando, and D. Wennerberg. Swirling, particle-laden flows through a pipe expansion. *Journal of Fluids Engineering*, 114:648–656, 1992.

[93] S. L. Soo. *Particulates and Continuum Multiphase Fluid Dynamics*. Hemisphere Publishing Corporation, New York, New York, 1989.

[94] D. B. Spalding. *Some Fundamentals of Combustion*. Butterworths, London, 1955.

[95] D. B. Spalding. Theory of particle combustion at high pressure. *ARS Journal*, 29:828–835, 1959.

[96] S. Takahashi. Preparation of a generalized chart for the diffusion coefficients of gases at high pressures. *Journal of Chemical Engineering of Japan*, 7:417–420, 1974. doi: 10.1252/jcej.7.417.

[97] F.X. Tanner. Liquid jet atomization and droplet breakup modeling of non-evaporating diesel fuel sprays. *SAE Technical Paper*, 970050, 1997.

[98] F.X. Tanner. A cascade atomization and drop breakup model for the simulation of high-pressure liquid jets. *SAE Technical Paper*, 2003-01-1044, 2003.

[99] F.X. Tanner and G. Weisser. Simulation of liquid jet atomization for fuel sprays by means of a cascade drop breakup model. *SAE Technical Paper*, 980808, 1998.

[100] G.I. Taylor. *The shape and acceleration of a drop in a high speed air stream*, volume 3. In G.K. Batchelor, ed., The scientific papers of Sir Geoffrey Ingram Taylor, Cambridge University Press, 1963.

[101] J. R. Travis, F. H. Harlow, and A. A. Amsden. Numerical calculation of two-phase flows. *Nuclear Science and Engineering*, 61:1–10, 1976.

[102] H.P. Trinh and C.P. Chen. Modeling of turbulence effects on liquid jet atomization and breakup. *Atomization Spray*, 16:097–932, 2006.

[103] H.P Trinh, C.P. Chen, and M.S. Balasubramanyam. Numerical simulation of liquid jet atomization including turbulence effects. *41st AIAA/ASME/SAE/ASEE Joint Propulsion Conference*, 2005-3973, 2005.

[104] M. R. Turner, S. S. Sazhin, J. J. Healey, C. Crua, and S. B. Martynov. A breakup model for transient diesel fuel sprays. *Fuel*, 97:288–305, 2012.

[105] J. D. van der Waals. Square gradient model. *Verhandel Konik Akad Weten Amsterdam*, 1: 8–15, 1893.

[106] G. J. VanWylen and R. E. Sonntag. *Fundamentals of Classical Thermodynamics*. John Wiley and Sons, Incorporated, New York, 1986.

[107] J. D. Van Der Waals. *De Continuiteit van den Gas- En Vloeistoftoestand*. PhD thesis, Aan de Hoogeschool Te Leiden, 1873.

[108] Z. Wang, A. Swantek, R. Scarcelli, D. Duke, A. Kastengren, C. F. Powell, S. Som, R. Reese, K. Freeman, and Y. Zhu. Les of diesel and gasoline sprays with validation against x-ray radiography data. *SAE Int. J. Fuels Lubr.*, 8, 2015.

[109] F. A. Williams. The transport equations for multi-phase systems. *Physics of Fluids*, 1: 541–545, 1958.

[110] F. A. Williams. *Combustion Theory*. Addison Wesley, 1985.

[111] F. Xiao, M. Dianat, and J. J. McGuirk. Les of turbulent liquid jet primary breakup in turbulent coaxial flow. *Int. J. Multiphase Flow*, 60:103–118, 2014.

[112] X. Yang, A. Solomon, and T.-W. Kuo. Ignition and combustion simulations of spray-guided sidi engine using arrhenius combustion with spark-energy deposition model. *SAE Technical Paper*, 2012-01-0147, 2012.

[113] M.C. Yuen and L.W. Chen. On drag of evaporating liquid droplets. *Combust. Sci. Techn.*, 14:147–154, 1976.

[114] Y.-X. Zuo and E. H. Stenby. A linear gradient theory model for calculating interfacial tensions of mixtures. *J. Colloid Interface Sci.*, 182:126–132, 1996. doi: 10.1006/jcis.1996.0443.

DISTRIBUTION:

1 MS 0899 Technical Library, 8944 (electronic copy)
1 MS 0359 D. Chavez, LDRD Office, 1911

This page intentionally left blank.


Sandia National Laboratories